

Dissertation thesis



Czech
Technical
University
in Prague

F2

Faculty of Mechanical Engineering
Department of Mechanics, Biomechanics and Mechatronics

Finite element method based computational time reversal in elastodynamics

Ing. Michal Mračko

Supervisor: Ing. Jiří Plešek, CSc.

Supervisor–specialist: doc. Ing. Radek Kolman, Ph.D.

Field of study: P2301 - Mechanical Engineering

Subfield: 3901V024 - Mechanics of Solids, Deformable Bodies and
Continua

March 2023

Acknowledgements

First and foremost, I would like to thank my wife for her support and for taking care of our children during a time-consuming period. Another thanks goes to my supervisor Ing. Jiří Plešek, CSc. for hiring me in the first place and starting my scientific career. A special thanks goes to my supervisor-specialist associate professor Ing. Radek Kolman, Ph.D. for constant support in my studies and personal development. Without him, the articles that form the backbone of this work would not have been possible. I would like to thank Ing. Anton Tkachuk, Ph.D. for guiding me at the right time. I would like to thank Ing. Zdeněk Převorovský, CSc., Ing. Jan Kober, Ph.D., prof. Arkadi Bere-zovski, and Ing. Vítězslav Adámek, Ph.D. for fruitful collaboration on the papers, and Ing. Ján Kopačka, Ph.D. and Ing. Alena Kruisová, Ph.D. for valuable discussions related to this work as well as non-related ones. Last but not least, I would like to thank all colleagues who contributed with their advice to improve the quality of this work.

Michal Mračko

Declaration

I hereby declare that my dissertation entitled *Finite element method based computational time reversal in elastodynamics* is the result of my own work and does not contain anything that is the outcome of work done in collaboration, unless stated in the text.

Michal Mračko

Prague, March 16, 2023

Abstract

The aim of this thesis is to develop a methodology to correctly reconstruct the source in the time domain using the computational time reversal method. This capability would allow identification of existing or forming flaws and defects in the material by analyzing the reconstructed signals. Localization of sources or scatterers using refocusing of energy is a well-established method, but reconstruction of the time history of these sources is still an unsolved scientific problem. A dedicated explicit solver based on the finite element method is developed and used here to solve the elastic wave propagation in solid material. The developed methodology is numerically tested and also verified using experimental data. It is proved that the reconstruction is feasible and correct with a sufficiently tuned model. Thanks to the presented research, the practical deployment of the computational time reversal method is more promising and it can be included in the concept of the so-called digital twin. On the other hand, the method itself is very sensitive to the input parameters and in principle very computationally demanding, which are aspects that still need to be addressed. This also opens up possibilities for further research.

Keywords:

Time reversal, source reconstruction, finite element method

Supervisor:

Ing. Jiří Plešek, CSc.

Supervisor—specialist:

doc. Ing. Radek Kolman, Ph.D.

Abstrakt

Cílem práce je vyvinout metodologii pro věrohodnou rekonstrukci zdroje v časové oblasti za použití metody výpočetní časové reverzace. Tato schopnost by pomocí analýzy rekonstruovaných signálů umožnila identifikovat stávající nebo vznikající poruchy a defekty v materiálu. Lokalizace zdroje za pomoci zpětného zaměření energie je dobře známá metoda, nicméně rekonstrukce časového průběhu zdroje je stále otevřený vědecký problém. Pro řešení šíření elastických vln byl vyvinut a použit vlastní explicitní řešič založený na metodě konečných prvků. Vyvinutá metodologie byla otestována numericky a verifikována na experimentálních datech. Bylo prokázáno, že s dostatečně naladěným numerickým modelem je rekonstrukce zdroje nejen proveditelná, ale také správná. Díky představenému výzkumu je praktické nasazení výpočetní metody časové reverzace perspektivnější a metoda může být zahrnuta do konceptu zvaného digitální dvojče. Na druhou stranu, samotná metoda je velmi citlivá na vstupní parametry a z principu náročná na výpočet, což jsou aspekty, se kterými je nutné se vypořádat. Tím se také otevírají možnosti pro další výzkum.

Klíčová slova:

Časová reverzace, rekonstrukce zdroje, metoda konečných prvků

Překlad názvu:

Řešení úloh časové reverzace v elastodynamice použitím metody konečných prvků

Contents

1 Introduction	1	
2 State of the art	3	
2.1 Wave propagation in solids	3	
2.2 Linear elastodynamic problem . . .	3	
2.2.1 Types of waves, wave speed ..	6	
2.3 Time reversal method	8	
2.4 TR problem - definitions and governing equations	8	
2.4.1 Definition of the frontal problem	8	
2.4.2 Definition of the reverse problem as a source identification problem	10	
2.5 Finite element method	11	
2.5.1 Explicit time integration . . .	12	
2.5.2 Reduced integration	12	
2.5.3 Hourglass control	13	
2.5.4 Mass matrix lumping	13	
2.5.5 Rigid body modes filtering ..	13	
2.5.6 Time step size estimations ..	14	
3 Aim of the thesis	19	
3.1 Aim	19	
3.2 Objectives	19	
4 Results of the PhD research	21	
4.1 TR-FEM solver	21	
4.2 Numerical simulations of the frontal problem	22	
4.2.1 Homogeneous elastic strip . .	22	
4.2.2 Heterogeneous elastic strip ..	30	
4.3 Numerical simulation of the reverse problem	38	
4.3.1 Loading and boundary conditions	39	
4.3.2 Definition of cost functions ..	40	
4.3.3 Problem definition	42	
4.3.4 Refocusing test	44	
4.3.5 Reconstruction test and proposed methodology	49	
4.3.6 Key verification of the proposed methodology	54	
4.3.7 Numerical sensitivity study of the proposed methodology	58	
4.4 TR with experimental data	66	
4.4.1 Problem definition	66	
4.4.2 Results of TR with experimental data	67	
4.4.3 Study of sensitivity to position of reverse load	68	
4.4.4 Discussion of TR with experimental data	69	
4.5 Other numerical examples	70	
4.5.1 Influence of temperature	70	
4.5.2 Cross-correlation	73	
4.5.3 Crack detection	75	
5 Discussion	79	
6 Conclusions	81	
Bibliography	83	
Author's peer-reviewed journal papers	83	
Author's conference journal papers .	83	
Author's conference talks	83	
Author's conference posters	85	
Other references	85	

Figures

<p>2.1 Illustrative picture generated by AI model DALL-E from given description: <i>3d render of sinusoidal waves made of wool flying around group of people in light colors.</i> 4</p> <p>2.2 Application of TR method in NDT. 8</p> <p>2.3 Scheme of TR problem. Ω is the the domain of interest, Ω_S is the support of the original source, and Ω_m is the area of measurement. 9</p> <p>2.4 Gershgorin circles. 16</p> <p>2.5 Diagonal entities for l_c in equation (2.39) 18</p> <p>4.1 Sketch of the problem [A1]. 22</p> <p>4.2 Experimental setup [A1]. 24</p> <p>4.3 Shape of ideal and real loading pulses [A1]. 24</p> <p>4.4 The response to the ideal pulse: analytical solution vs numerical simulations [A1]. 25</p> <p>4.5 The response to the real pulse at point A: analytical and numerical solution vs experimental data [A1]. 26</p> <p>4.6 The response to the real pulse at point B: analytical and numerical solution vs experimental data [A1]. 27</p> <p>4.7 The response to the real pulse at point C: analytical and numerical solution vs experimental data [A1]. 27</p> <p>4.8 The response to the real pulse at point B obtained by the stress and velocity loading [A1]. 28</p> <p>4.9 Distribution of the mean velocity $\sqrt{v_1^2 + v_2^2}$ inside the strip. Snapshots of the analytical solution for $t = \{186\Delta t, 420\Delta t, 561\Delta t, 753\Delta t\}$ [A1]. 29</p> <p>4.10 Measured response vs analytical solution and finite element computation for longer time [A1]. . 29</p> <p>4.11 Comparison of results for finite element 2D and 3D simulation [A1]. 30</p> <p>4.12 Sketch of the problem [A2]. 31</p>	<p>4.13 Time history of the normalized stress σ_{11} at point A in homogeneous aluminum strip [A2]. 33</p> <p>4.14 Time history of the normalized stress σ_{11} at point B in homogeneous aluminum strip [A2]. 33</p> <p>4.15 Time variation of loading pulse along the vertical central line [A2]. 34</p> <p>4.16 Time history of the normalized stress σ_{11} at point A in two-layer $Al-Al_2O_3$ strip [A2]. 35</p> <p>4.17 Time history of the normalized stress σ_{11} at point B in two-layer $Al-Al_2O_3$ strip [A2]. 35</p> <p>4.18 Time history of the longitudinal stress at point A in two-layer Al_2O_3-Al strip [A2]. 36</p> <p>4.19 Time history of the longitudinal stress at point B in two-layer Al_2O_3-Al strip [A2]. 37</p> <p>4.20 The equivalent stress field (mapped to the z-direction) at certain time for all three compositions of two-layer strip. 37</p> <p>4.21 Time windows for cost functions C_i [A3]. 41</p> <p>4.22 Scheme of the domain of interest, [m] [A3]. 43</p> <p>4.23 Loading Ricker pulse with its parameters [A3]. 43</p> <p>4.24 A snapshot of y-component of velocity and total energy per volume distribution from the frontal problem for time $94 \Delta t$ corresponding to the maximum peak of loading pulse [A3]. 45</p> <p>4.25 A snapshot of reconstruction of y-component of velocity and total energy per volume distribution from the reverse problem for time of maximum peak T_M and several other times; loading by TYPE I - "velocity loading", computational time $T = 100,000 \Delta t$ [A3]. 45</p>
-----------------------------------------------------------------------------------------------------------------------------------------------------------------------------------------------------------------------------------------------------------------------------------------------------------------------------------------------------------------------------------------------------------------------------------------------------------------------------------------------------------------------------------------------------------------------------------------------------------------------------------------------------------------------------------------------------------------------------------------------------------------------------------------------------------------------------------------------------------------------------------------------------------------------------------------------------------------------------------------------------------------------------------------------------------------------------------------------------------------------------------------------------------------------------------------------------------------------------------------------------------------------------------------------------------------------------------------------------------------------------------------------------------------------------------------------------------------------------------------------------------------------------------------------------------------------------------------------------------------------------------------------------------------------------------------------------------------------------------------------------------------------------------------------------------------------------------------------------------	------------------------------------------------------------------------------------------------------------------------------------------------------------------------------------------------------------------------------------------------------------------------------------------------------------------------------------------------------------------------------------------------------------------------------------------------------------------------------------------------------------------------------------------------------------------------------------------------------------------------------------------------------------------------------------------------------------------------------------------------------------------------------------------------------------------------------------------------------------------------------------------------------------------------------------------------------------------------------------------------------------------------------------------------------------------------------------------------------------------------------------------------------------------------------------------------------------------------------------------------------------------------------------------------------------------------------------------------------------------------------------------------------------------------------------------------------------------------------------------------------------------------------------------------------------------------------------------------------------------------------------------------------------------------------------------------------------------------------------------------------------------------------------------------------------------------------------------------

4.25 A snapshot of reconstruction of y-component of velocity and total energy per volume distribution from the reverse problem for time of maximum peak T_M and several other times. Loading by TYPE I - "velocity loading", computational time $T = 100,000 \Delta t$ [A3].	46	4.30 Reconstructions of the original source for four different combinations of modification of loading signals in frontal and reverse problems, denoted as Int and Orig . The first indication refers to frontal problem, the second one refers to reverse problem. The keys Int marks the time integration of the pulse and Orig marks the pulse without modification, i.e. without time integration [A3].	52
4.26 A snapshot of reconstruction of y-component of velocity and total energy per volume distribution from the reverse problem for time of maximum peak T_M and several other times. Loading by TYPE II - "force nodal loading", computational time $T = 100,000 \Delta t$ [A3].	47	4.31 Scheme of the different ways to prescribe the loading values <i>val</i> . N nodes loaded (left), N nodes loaded - averaged (right) [A3].	54
4.26 A snapshot of reconstruction of velocity-y and total energy distribution from the reverse problem for time of maximum peak T_M and several other times. Loading by TYPE II - "nodal force loading", computational time $T = 100,000 \Delta t$ [A3].	48	4.32 Global cost C_G , TYPE I - loading by nodal velocities [A3].	55
4.27 Output quantities in the y-direction at the middle point of loading by nodal force. The time function of nodal force (top-left) was applied as a load, other graphs represent the response of FE model. Only the quantities in the middle node out of nine nodes in total at point A were recorded [A3].	49	4.33 Global cost C_G , TYPE II - loading by nodal forces [A3].	56
4.28 Reconstruction of the original source (left); original loading pulse with its time derivatives (right), original pulse (red solid line), its 1 st time derivative (orange dashed line), and its 2 nd time derivative (brown dotted line); reconstructed pulse (gray solid line) is also added here for clarity [A3].	50	4.34 Reconstructed pulse for time T_{10} , loading of TYPE I - nodal velocities [A3].	57
4.29 An integrated Ricker pulse as a time integral $\int_0^T R(t)dt$ [A3].	51	4.35 Reconstructed pulse for time T_{10} , loading of TYPE II - nodal forces [A3].	57
		4.36 Sensitivity study 1 - Reconstruction [A3].	59
		4.37 Sensitivity study 2 - Reconstruction [A3].	60
		4.38 Sensitivity study 3 - positions of recording points [A3].	61
		4.39 Sensitivity study 3 - Reconstruction [A3].	61
		4.40 Sensitivity study 4 - scheme [A3].	62
		4.41 A snapshot of velocity wave field from the frontal problem for time $300 \Delta t$, comparison of a domain without/with a hole [A3].	62
		4.42 Sensitivity study 4 - Reconstruction [A3].	63
		4.43 Sensitivity study 5 - creation of noise [A3].	64
		4.44 Sensitivity study 5 - Reconstruction [A3].	65
		4.45 Scheme of experimental measurement.	66

4.46 Loading signal.	67
4.47 X-t plot of measured normal velocities.	67
4.48 Result of TR.	68
4.49 Scheme shows positions (P1,...,P5) of loaded group of nodes and their distance from the axis of symmetry.	68
4.50 Result of sensitivity study to position of reverse load. Reconstruction of the loading signal is in the left column in blue, black line is the real loading pulse. In the right column is the cross-correlation of the reconstructed and the original signal.	69
4.51 Scheme for analysis of influence of temperature.	71
4.52 Reconstructed pulse - decreased wave speed c_L (increased temperature).	72
4.53 Reconstructed pulse - increased wave speed c_L (decreased temperature).	72
4.54 Scheme of the numerical experiment - localization of source using cross-correlation.	73
4.55 Settings of the numerical experiment: loading signal, loaded nodes, and nodes where the output was recorded.	74
4.56 Result of correlated signals on coarse and refined grid. The red signals come from nodes originally loaded in the frontal task.	74
4.57 Scheme of the numerical experiment of forming and propagating crack detection.	75
4.58 Localization of forming crack, magnitude of nodal velocity for different times of computation and number of loaded nodes.	77
4.59 Localization of propagating crack, magnitude of nodal velocity for different times of computation and number of loaded nodes.	78

Tables

2.1 Overview of the selected elastic wave speeds.	7
4.1 Material properties of the strip under investigation.	23
4.2 Values of material properties.	31
4.3 Table of computational times T_i	54
4.4 Sensitivity study 1 - input values [A3].	58
4.5 Sensitivity study 2 - input values.	59
4.6 Change of longitudinal wave speed c_L and Young's modulus E in case study.	70



Symbols and abbreviations



Abbreviations

Abbreviation	Description
CDM	Central difference method
FE	Finite element
FEM	Finite element method
NDT	Non-destructive testing
RBM	Rigid body mode
SHM	Structural health monitoring
TR	Time reversal

Material properties

Symbol	Unit	Description
E	$[\text{kgm}^{-1}\text{s}^{-2}]$	Young's modulus
G	$[\text{kgm}^{-1}\text{s}^{-2}]$	Shear modulus, Lamé parameter
Λ	$[\text{kgm}^{-1}\text{s}^{-2}]$	Lamé parameter
ρ	$[\text{kgm}^{-3}]$	Mass density
ν	$[-]$	Poisson's ratio
c_L	$[\text{ms}^{-1}]$	Wave speed of longitudinal waves
c_T	$[\text{ms}^{-1}]$	Wave speed of transversal waves
c_R	$[\text{ms}^{-1}]$	Wave speed of Rayleigh waves
m	$[\text{kg}]$	Mass

Index notation

Symbol	Unit	Description
σ_{ij}	$[\text{kgm}^{-1}\text{s}^{-2}]$	Stress tensor
ε_{ij}	$[-]$	Infinitesimal strain tensor
C_{ij}	$[\text{kgm}^{-1}\text{s}^{-2}]$	Elasticity tensor
δ_{ij}	$[-]$	Kronecker delta
u_i	$[\text{m}]$	Displacement
$\dot{u}_i = v_i$	$[\text{ms}^{-1}]$	Velocity
$\ddot{u}_i = a_i$	$[\text{ms}^{-2}]$	Acceleration
w_i	$[\text{m}]$	Reversed displacement
\dot{w}_i	$[\text{ms}^{-1}]$	Reversed velocity
x_i	$[\text{m}]$	Spatial coordinate
b_i	$[\text{kgm}^{-2}\text{s}^{-2}]$	Body force
M_{ij}	$[\text{m}]$	Element of mass matrix

Vector notation

Symbol	Unit	Description
$\boldsymbol{\sigma}$	$[\text{kgm}^{-1}\text{s}^{-2}]$	Cauchy stress tensor
$\boldsymbol{\varepsilon}$	$[\text{kgm}^{-1}\text{s}^{-2}]$	Infinitesimal strain tensor
\mathbf{C}	$[\text{kgm}^{-3}]$	Elasticity matrix
\mathbf{u}	$[\text{m}]$	Displacement vector
\mathbf{u}^0	$[\text{m}]$	Displacement vector from initial condition
\mathbf{u}_m	$[\text{m}]$	Measured displacement vector
\mathbf{u}_R	$[\text{m}]$	Vector of displacement component corresponding to rigid body motion
\mathbf{d}	$[\text{m}]$	Vector of displacement component without rigid body motion
$\dot{\mathbf{u}} = \mathbf{v}$	$[\text{ms}^{-1}]$	Velocity vector
$\dot{\mathbf{u}}^0 = \mathbf{v}^0$	$[\text{ms}^{-1}]$	Velocity vector from initial condition
$\dot{\mathbf{u}}_m = \mathbf{v}_m$	$[\text{ms}^{-1}]$	Measured velocity vector
$\ddot{\mathbf{u}} = \mathbf{a}$	$[\text{ms}^{-2}]$	Acceleration vector
$\ddot{\mathbf{u}}^0 = \mathbf{a}^0$	$[\text{ms}^{-2}]$	Acceleration vector from initial condition
\mathbf{w}	$[\text{m}]$	Reverse displacement vector
$\dot{\mathbf{w}}$	$[\text{ms}^{-1}]$	Reverse velocity vector
\mathbf{x}	$[\text{m}]$	Spatial coordinate vector
\mathbf{I}	$[-]$	Identity matrix
\mathbf{I}_f	$[\text{kgms}^{-1}]$	Force impulse vector
\mathbf{p}	$[\text{kgms}^{-1}]$	Vector of linear momentum
\mathbf{M}	$[\text{kg}]$	Global mass matrix
\mathbf{M}^e	$[\text{kg}]$	Element mass matrix
\mathbf{M}^{diag}	$[\text{kg}]$	Diagonal mass matrix
\mathbf{K}	$[\text{kgs}^{-2}]$	Global stiffness matrix
\mathbf{K}^e	$[\text{kgs}^{-2}]$	Element stiffness matrix
$\mathbf{K}_{1\text{gp}}$	$[\text{kgs}^{-2}]$	Stiffness matrix matrix obtained by 1-point integration
\mathbf{K}_{stab}	$[\text{kgs}^{-2}]$	Stability stiffness matrix
\mathbf{f}_{ext}	$[\text{kgms}^{-2}]$	Vector of external forces
$\mathbf{f}_{\text{ext}}^0$	$[\text{kgms}^{-2}]$	Initial vector of external forces
\mathbf{r}	$[\text{kgms}^{-2}]$	Vector of residual forces
\mathbf{N}	$[-]$	Shape functions matrix
\mathbf{B}	$[-]$	Strain-displacement matrix
\mathbf{t}	$[\text{kgm}^{-1}\text{s}^{-2}]$	Traction vector



Chapter 1

Introduction

With the advent of Industry 4.0, [21, 22], terms such as structural health monitoring (SHM), [23, 24, 25], or digital twin, [26, 27], have been more frequently cited. Knowing the structural changes in a construction caused by emerging flaws is as attractive as knowing the end of life of working equipment or consumables. This inevitably requires real-time monitoring and evaluation of the recorded data. One possible way to evaluate this is through a computational model - the digital twin. If the computational model is representative and accurate enough, it can be used to simulate the inverse problem to detect and analyze new sources, primarily, of vibration. The originator of additional vibration could be for example an impact or an existing or forming crack. The correct and robust localization of cracks and defects in bodies and structures in energetics [28], civil engineering [29], or aerospace [30], is still a hot topic despite the long history of this research. Moreover, this knowledge and information about cracks are needed for practical applications to ensure safe operation in various industries, such as power plants, aircraft, vehicles, satellites, and many others.

One method for locating flaws in structures is the time reversal (TR) method. The TR method belongs to the family of inverse methods in physics, [31], and is based on the properties of the Hamiltonian system [32]. TR was first formulated in the 1960s under the name “matched signal processing” for underwater acoustic communications of submarines [33]. In the 1990s, Fink and his collaborators, [34], did much research for application in acoustics and renamed the method “time reversal (or time reversed acoustics)”. The TR method is a powerful tool that can be used in various physical fields involving wave propagation. It uses the property of reversibility of wave propagation to focus the energy to the original source location in space and time. When the original source is very local, this procedure is called refocusing. Nowadays, the most important applications are in nondestructive testing (NDT), underwater acoustics [35, 36], biomedical ultrasound imaging [37], surgery and lithotripsy [38, 39], and last but not least, seismology [40].

In ultrasonic NDT, the TR method can be used to detect defects in materials and cracks in bodies. Depending on the approach, one can speak of passive and active detection. In general, in passive detection, the emerging defects (forming/propagating cracks, impacts, leaks in pipes) are detected,

for example, with help of acoustic emission [41]. In active detection, a "third" excitation signal is used to locate the existing flaw (crack, cavity), which serves as a scatterer for the propagating elastic wave. A crack exposed to a wave passing through acts as an additional wave source and can therefore be localized [42].

The computational TR method has been widely employed, e.g. to localize an acoustic impact with temperature effect [43], to localize scatterers [44, 45, 46], to identify damage in a beam structure [47], to reconstruct the shape of traction-free scatterers [48], or to localize noise sources in a road vehicle [49]. Noticeable progress has been made in the use of experimental data for damage identification [50]. Several works are dedicated to investigate or improve the quality of reconstruction of the original source [51, 52, 53]. While localization is a mastered process, reconstruction of the source in the time domain has not yet been fully managed and a methodology to perform the TR in standard and widely used numerical methods such as the finite element method (FEM) has not been fully established. This work aims to improve the reconstruction of the exciting signal in the time domain, meaning some existing or forming flaw in the material, and to determine the proper procedure for deploying TR in practice, i.e., in commercial finite element (FE) software.

The thesis is divided into several main chapters; **Chapter 2 – State of the art**, where the used methods are presented and explained - mainly the time reversal method; **Chapter 3 – Aim of the thesis**, where aim and objectives of the work are mentioned; carrying part of the thesis is **Chapter 4 – Results of the PhD research**, consisting mainly of the results from papers published in impact journals, [A1, A2, A3], then several numerical experiments and time reversal with experimental data follow; **Chapter 5 – Discussion**, where the merit of this work is emphasized and recommendations for future research are discussed; and the work ends with **Chapter 6 – Conclusions**.

Chapter 2

State of the art

2.1 Wave propagation in solids

Waves and their propagation are studied in many scientific fields such as acoustics, seismology, fluid mechanics, and many others, but we also observe them in everyday life. The most imaginable phenomenon is waves in the ocean, but the same laws also apply to radio waves, [54], or traffic flow, [55]. Waves, in some form, surround us all the time; see the illustrative Pic. 2.1 generated by the artificial intelligence (AI) model DALL·E. But what is a wave?

"A wave is any recognizable signal that is transferred from one part of the medium to another with a recognizable velocity of propagation. The signal may be any feature of the disturbance, such as a maximum or an abrupt change in some quantity, provided that it can be clearly recognized and its location at any time can be determined." [56] page 2.

Whitham distinguishes in his book two main classes of waves - hyperbolic, which are formulated mathematically in terms of hyperbolic partial differential equations, and dispersive, which are not so easily characterized but are united by the fact that their wave velocity is not constant for some reason.

This work is limited to (hyperbolic) elastic wave propagation in solid materials and, in particular, to their numerical solution.

2.2 Linear elastodynamic problem

Elastic wave propagation in unbounded domain $\Omega \subset \mathbb{R}^3$ follows the equations of motion which can be derived from balance of linear momentum and stress-strain relation. We start with balance of linear momentum in index notation

$$\rho \frac{\partial^2 u_i}{\partial t^2} = b_i + \frac{\partial}{\partial x_j} \sigma_{ij}, \text{ on } \Omega. \quad (2.1)$$

In the following derivation we do not include body forces b_i , since in elastic problems with small displacements they are insignificant and can be neglected.



Figure 2.1: Illustrative picture generated by AI model DALL·E from given description: *3d render of sinusoidal waves made of wool flying around group of people in light colors.*

Now we introduce the stress-strain relation (Hooke's law) by which the stress tensor σ_{ij} for isotropic material is defined as

$$\sigma_{ij} = \Lambda \delta_{ij} \varepsilon_{kk} + 2G \varepsilon_{ij}, \quad (2.2)$$

and the components of infinitesimal strain tensor ε_{ij} are derived from displacement components u_i , as

$$\varepsilon_{ij} = \frac{1}{2} \left(\frac{\partial u_i}{\partial x_j} + \frac{\partial u_j}{\partial x_i} \right). \quad (2.3)$$

If we combine equations (2.1), (2.2), and (2.3), we obtain the equation of balance of linear momentum for an isotropic linear material

$$\rho \frac{\partial^2 u_i}{\partial t^2} = (\Lambda + G) \frac{\partial^2 u_j}{\partial x_i \partial x_j} + G \frac{\partial^2 u_i}{\partial x_j \partial x_j}. \quad (2.4)$$

We can express equation (2.4) also in vector notation, as

$$\rho \frac{\partial^2 \mathbf{u}}{\partial t^2} = (\Lambda + G) \nabla (\nabla \cdot \mathbf{u}) + G \nabla^2 \mathbf{u}. \quad (2.5)$$

Here $\nabla \equiv \left\{ \frac{\partial}{\partial x_1}, \frac{\partial}{\partial x_2}, \frac{\partial}{\partial x_3} \right\}$ is Nabla operator. The part of the last term, $\nabla^2 \mathbf{u}$, is called *vector Laplacian* and the following relation holds for it

$$\nabla^2 \mathbf{u} = \nabla (\nabla \cdot \mathbf{u}) - \nabla \times (\nabla \times \mathbf{u}). \quad (2.6)$$

Putting ((2.6)) into ((2.5)) we obtain

$$\rho \frac{\partial^2 \mathbf{u}}{\partial t^2} = (\Lambda + 2G) \nabla(\nabla \cdot \mathbf{u}) - G \nabla \times (\nabla \times \mathbf{u}). \quad (2.7)$$

Such an equation is not so easy to solve, which is why the *Helmholtz decomposition* [57] is introduced. The Helmholtz decomposition states that a vector field (if it satisfies appropriate smoothness and decay conditions) can be decomposed into the sum of the irrotational vector field (gradient of a scalar potential ϕ) and the solenoidal (divergence-free) vector field (curl of a vector potential ψ). This applied to the displacement field gives

$$\mathbf{u} = \nabla \phi + \nabla \times \psi. \quad (2.8)$$

If we use (2.8) to every term in (2.7) containing \mathbf{u} , separately just for clarity, we obtain

$$\rho \frac{\partial^2 \mathbf{u}}{\partial t^2} = \nabla \rho \frac{\partial^2 \phi}{\partial t^2} + \nabla \times \rho \frac{\partial^2 \psi}{\partial t^2}, \quad (2.9)$$

$$\nabla \cdot \mathbf{u} = \nabla \cdot \nabla \phi + \nabla \cdot (\nabla \times \psi), \quad (2.10)$$

$$\nabla \times \mathbf{u} = \nabla \times \nabla \phi + \nabla \times (\nabla \times \psi), \quad (2.11)$$

where by definition,

$$\nabla \cdot (\nabla \times \psi) = 0, \quad \nabla \cdot \nabla \phi = \nabla^2 \phi \text{ (in (2.10)), and}$$

$$\nabla \times \nabla \phi = 0 \text{ in ((2.11)).}$$

On the second term in (2.11) we can again apply the formula (2.6), so

$$\nabla \times (\nabla \times \psi) = \nabla(\nabla \cdot \psi) - \nabla^2 \psi.$$

For solenoidal vector field ψ , $\nabla \cdot \psi = 0$, thus the first term vanishes. Putting the remaining terms from equations (2.9), (2.10), and (2.11) into (2.7) gives us

$$\nabla \rho \frac{\partial^2 \phi}{\partial t^2} + \nabla \times \rho \frac{\partial^2 \psi}{\partial t^2} = (\Lambda + 2G) \nabla \nabla^2 \phi + \nabla \times (G \nabla^2 \psi) \quad (2.12)$$

and we can rewrite this equation to

$$\nabla \left[\rho \frac{\partial^2 \phi}{\partial t^2} - (\Lambda + 2G) \nabla^2 \phi \right] + \nabla \times \left[\rho \frac{\partial^2 \psi}{\partial t^2} - G \nabla^2 \psi \right] = 0. \quad (2.13)$$

The equation of motion (2.13) is satisfied if potentials ϕ and ψ satisfy the equations

$$\frac{\partial^2 \phi}{\partial t^2} = \alpha^2 \nabla^2 \phi, \quad (2.14)$$

$$\frac{\partial^2 \psi}{\partial t^2} = \beta^2 \nabla^2 \psi, \quad (2.15)$$

propagation. Both Rayleigh and Love waves play an important role especially in seismology.

Many other types of waves have been described, such as von Schmidt waves, Lamb waves, Stoneley waves, or torsional or bending waves. These generally exhibit dispersion behavior and more complex motion. Some complex waves such as Rayleigh or Lamb waves are used in a method called *guided wave testing* [59, 60]. This method takes advantage of the natural properties of certain waves (infinite number of wave modes, wave speed depending on the structure and loading frequency), which makes it more versatile and effective than standard ultrasonic testing.

The values of wave speeds depend on the material elastic properties, the Lamé parameters Λ and G , and the physical properties, the mass density ρ . Some wave speeds are more clear to express in engineering parameters, Young's modulus E , Poisson's ratio ν , eventually shear modulus G . The transition between Lamé parameters and engineering parameters is governed by the formulas

$$\Lambda = \frac{\nu E}{(1 + \nu)(1 - 2\nu)}, \quad G = \frac{E}{2(1 + \nu)}. \quad (2.17)$$

3D	Longitudinal		$c_L = \sqrt{\frac{\Lambda+2G}{\rho}}$
	Transversal		$c_T = \sqrt{\frac{G}{\rho}}$
2D	Plane strain	Longitudinal	$c_L = \sqrt{\frac{\Lambda+2G}{\rho}}$
		Transversal	$c_T = \sqrt{\frac{G}{\rho}}$
	Plane stress	Longitudinal	$c_L = \sqrt{\frac{E}{(1-\nu^2)\rho}}$
		Transversal	$c_T = \sqrt{\frac{G}{\rho}}$
1D	Uniaxial strain		$c_L = \sqrt{\frac{(1-\nu)E}{(1+\nu)(1-2\nu)\rho}}$
	Uniaxial stress		$c_T = \sqrt{\frac{E}{\rho}}$
Rayleigh wave speed along half-space boundary			$c_R = c_T \frac{0.862+1.14\nu}{1+\nu}$

Table 2.1: Overview of the selected elastic wave speeds.

2.3 Time reversal method

In practice, the process of localization is accomplished in two steps. The first step, based on forward propagation, is the measurement on a real structure. In the second step, the measured signals are reversed in time and transmitted to the computational model, where, based on backpropagation, the energy is focused into the location of the original source. The mentioned process is schematically shown in Figure 2.2. Generally, one works only with partial information (incomplete data from sensors), since it is not possible to record response signals in the whole structure. There are two approaches to perform effective refocusing using the TR method. The first is using a substantial number of transducers in combination with a short recording time (and computation time), the second is the exact opposite – using only one or several transducers combined with a long recording time. The second approach exploits reflections at the structure boundaries, which compensate for the lack of direct information and overall create a virtual time-reversal mirror, see [61].

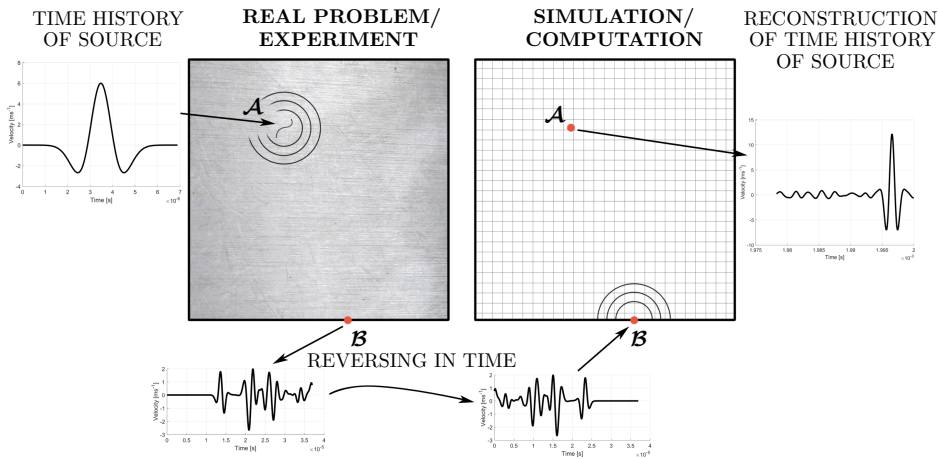


Figure 2.2: Application of TR method in NDT.

2.4 TR problem - definitions and governing equations

In this work, the classical theory of small deformations of elastic isotropic media is used for the mathematical description of elastic wave propagation in solids, which is applied to the frontal and reverse problem of TR. The definition of the problems was inspired by the paper [62].

2.4.1 Definition of the frontal problem

The first step is to define the frontal problem with appropriate boundary and initial conditions. An open bounded domain $\Omega \in \mathbb{R}^3$ with smooth boundary

$\partial\Omega$ is considered. Moreover, the linear equations of elastodynamics in the domain Ω and in time $t \in [0, T]$ are considered. The governing equations of elastodynamics, see [63], are given by the kinematic relation, the Hooke's law, and the Cauchy's equation without volume force as

$$\nabla \cdot \boldsymbol{\sigma} = \rho \ddot{\mathbf{u}}, \quad \boldsymbol{\sigma} = \mathbf{C} : \boldsymbol{\varepsilon}, \quad \boldsymbol{\varepsilon} = \frac{1}{2}(\nabla \mathbf{u} + (\nabla \mathbf{u})^\top), \quad 0 \leq t \leq T, \quad \mathbf{x} \in \Omega, \quad (2.18a)$$

with boundary conditions

$$\mathbb{B} \mathbf{u} = \mathbf{0} \text{ on } \partial\Omega, \quad (2.18b)$$

and with initial conditions

$$\mathbf{u}(\mathbf{x}, t = 0) = \mathbf{u}^0(\mathbf{x}), \quad \dot{\mathbf{u}}(\mathbf{x}, t = 0) = \mathbf{v}^0(\mathbf{x}) \quad \mathbf{x} \in \Omega. \quad (2.18c)$$

In the aforesaid relations, the superimposed dots, $\dot{\square}$, $\ddot{\square}$, denote the derivatives with respect to time t and the operator $\nabla = \{\frac{\partial}{\partial x_1}, \frac{\partial}{\partial x_2}, \frac{\partial}{\partial x_3}\}$, $\boldsymbol{\sigma}$ is the Cauchy stress tensor, $\boldsymbol{\varepsilon}$ is the infinitesimal strain tensor, \mathbf{C} is the elastic tensor, and ρ is the mass density. Furthermore, $\mathbf{u}(\mathbf{x}, t)$ is the displacement, $\dot{\mathbf{u}}(\mathbf{x}, t)$ is the velocity, and $\ddot{\mathbf{u}}(\mathbf{x}, t)$ is the acceleration. For isotropic elastic medium, we consider the Hooke's law as $\boldsymbol{\sigma} = \Lambda \text{tr}(\boldsymbol{\varepsilon})\mathbf{I} + 2G\boldsymbol{\varepsilon}$, where Λ and G are Lamé's constants related to the engineering constants $\Lambda = \nu E / [(1 + \nu)(1 - 2\nu)]$ and $G = E / [2(1 + \nu)]$, where E and ν are the Young's modulus and the Poisson's ratio, respectively.

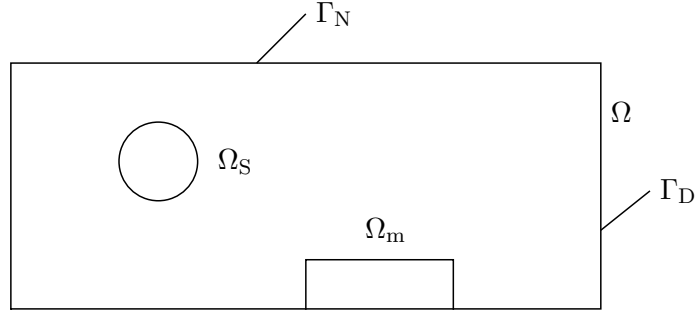


Figure 2.3: Scheme of TR problem. Ω is the the domain of interest, Ω_S is the support of the original source, and Ω_m is the area of measurement.

Furthermore in (2.18b), \mathbb{B} is a boundary operator on the displacement field $\mathbf{u}(\mathbf{x}, t)$ as the operator imposing boundary conditions on $\Gamma = \partial\Omega$. Neumann boundary conditions as stress-free boundary conditions are prescribed on Γ_N and Dirichlet boundary conditions are prescribed on Γ_D , where $\Gamma_D \cup \Gamma_N = \Gamma$ and $\Gamma_D \cap \Gamma_N = \emptyset$. The initial conditions are given by the displacement field $\mathbf{u}^0(\mathbf{x})$ and the velocity field $\mathbf{v}^0(\mathbf{x})$ at initial time $t = 0$ as in (2.18c). In future text, notations such as $\mathbf{u}(\mathbf{x}, t)$, $\mathbf{u}^t(\mathbf{x})$, and \mathbf{u}^t are equivalent.

with boundary conditions

$$\mathbb{B}\mathbf{w} = \mathbf{0} \text{ on } \partial\Omega, \quad (2.19b)$$

and with initial conditions

$$\mathbf{w}(\mathbf{x}, 0) = \mathbf{0}, \quad \dot{\mathbf{w}}(\mathbf{x}, 0) = \mathbf{0} \quad \mathbf{x} \in \Omega, \quad (2.19c)$$

and with kinematic conditions on Ω_m for TR identification as follows

$$\mathbf{w}(\mathbf{x}, \tau) = \mathbf{u}_m(\mathbf{x}, t), \quad \dot{\mathbf{w}}(\mathbf{x}, \tau) = -\dot{\mathbf{u}}_m(\mathbf{x}, t) \quad \mathbf{x} \in \Omega_m. \quad (2.19d)$$

For details on the TR problem formulation, see the work of [44]. Prescribing these kinematic conditions $\mathbf{w}(\mathbf{x}, \tau)$ and $\dot{\mathbf{w}}(\mathbf{x}, \tau)$ on Ω_m into the governing equations (2.19) provides the time reversal of the original problem defined in Section 2.4.1.

2.5 Finite element method

Although the development of the FE solver was one of the goals, FEM itself is used as a tool in this work. Therefore, the derivation of FEM from the variational principle is not shown here, but rather the important or less well-known procedures are explained and the level of description is determined by the specific application. A thorough description of the method can be found in essential books of famous authors such as Hughes [64], Belytschko [65], Bathe [66], or Zienkiewicz [67].

The spatially discretized equation of motion is

$$\mathbf{M}\ddot{\mathbf{u}}(t) + \mathbf{K}\mathbf{u}(t) = \mathbf{f}(t), \quad (2.20)$$

where \mathbf{u} is the vector of nodal displacements, $\ddot{\mathbf{u}}$ is the vector of nodal accelerations, \mathbf{M} is the mass matrix, \mathbf{K} is the stiffness matrix, \mathbf{f} is the vector of external forces, and the following formulas apply

$$\mathbf{M} = \sum_e \int_{\Omega^e} \rho \mathbf{N}^T \mathbf{N} d\Omega, \quad (2.21)$$

$$\mathbf{K} = \sum_e \int_{\Omega^e} \mathbf{B}^T \mathbf{C} \mathbf{B} d\Omega, \quad (2.22)$$

$$\mathbf{f} = \sum_e \int_{\Gamma} \mathbf{N} \mathbf{t} d\Omega. \quad (2.23)$$

Here, \mathbf{N} is matrix of shape functions, \mathbf{B} is matrix of shape functions derivatives, \mathbf{C} is stress-strain matrix, and \mathbf{t} is the traction vector.

2.5.1 Explicit time integration

Explicit time integration, namely the central difference method (CDM), is commonly used for the kind of problems analyzed in this work, so only this is mentioned. With CDM, the velocity (2.24) and the acceleration (2.25) are derived numerically from the displacement. There are several forms of implementation of CDM and here the so-called *leapfrog* form is used, see Algorithm 1. This algorithm is explained e.g. in [65].

$$\dot{\mathbf{u}}(t) \approx \frac{\mathbf{u}(t + \Delta t) - \mathbf{u}(t - \Delta t)}{2\Delta t} \quad (2.24)$$

$$\ddot{\mathbf{u}}(t) \approx \frac{\mathbf{u}(t + \Delta t) - 2\mathbf{u}(t) + \mathbf{u}(t - \Delta t)}{\Delta t^2} \quad (2.25)$$

Initialize $t^0 = 0$, \mathbf{u}^0 , $\dot{\mathbf{u}}^0$, assemble \mathbf{M} , \mathbf{K} , and compute

$$\ddot{\mathbf{u}}^0 = \mathbf{M}^{-1} (\mathbf{f}_{ext}^0 - \mathbf{K}\mathbf{u}^0)$$

```

while  $t < T$  do
    setting of the time step size  $\Delta t$ 
     $\dot{\mathbf{u}}(t + \frac{\Delta t}{2}) = \dot{\mathbf{u}}(t) + \ddot{\mathbf{u}}(t) \frac{\Delta t}{2}$ ;
     $\mathbf{u}(t + \Delta t) = \mathbf{u}(t) + \dot{\mathbf{u}}(t + \frac{\Delta t}{2})\Delta t$ ;
    application of boundary conditions;
     $\mathbf{r}(t + \Delta t) = \mathbf{f}_{ext}(t + \Delta t) - \mathbf{K}\mathbf{u}(t + \Delta t)$ ;
     $\ddot{\mathbf{u}}(t + \Delta t) = \mathbf{M}^{-1}\mathbf{r}(t + \Delta t)$ ;
     $\dot{\mathbf{u}}(t + \Delta t) = \dot{\mathbf{u}}(t + \frac{\Delta t}{2}) + \ddot{\mathbf{u}}(t + \Delta t) \frac{\Delta t}{2}$ ;
    application of boundary conditions;
     $t = t + \Delta t$ ;
end

```

Algorithm 1: The central difference scheme in the *leapfrog* form for direct time integration of elastodynamic problems.

2.5.2 Reduced integration

The integration of matrices and vectors is performed numerically, over integration points. There are several methods of numerical integration with varying accuracy and difficulty, such as the trapezoidal rule or the Simpson's rule, but the optimal method in FEM is the Gaussian quadrature. Compared to the previously mentioned methods, it requires fewer integration points to achieve the same accuracy and is therefore less time-consuming. Gaussian quadrature uses not equally spaced integration points with associated weights. The location of these points is obtained from the solution of Legendre polynomials. To attain the accuracy of order $2n$, n integration points are needed. The theory is thoroughly discussed in [68].

Linear rather than quadratic elements are mainly used in dynamic simulations, both for lower time demands for integration and for better representation of transient effects. Moreover, fully integrated linear elements may suffer from shear locking (or volumetric locking for incompressible material). That's the reason why the reduced integration was introduced.

Fully integrated linear element¹ requires 2 integration points per each dimension, thus reduced integration is given by 1 integration point, also referred to as one-point (Gauss) integration. The consequence of this is a "small" loss of accuracy in the evaluation of the integral. The reduced integration eliminates the risk of locking, but brings another problem to deal with, and that is presence of hourglass modes.

2.5.3 Hourglass control

When the element stiffness is evaluated only over one integration point, the element loses the stiffness for some deformation modes, called hourglass modes or zero-energy modes, since zero stiffness produces no energy for any deformation. To avoid this unphysical behavior, it is necessary to induce a certain resistance against the emergence of these modes and their propagation.

Several approaches can be seen in [69], [70], or [71]. One possible way is to add a stabilization stiffness matrix \mathbf{K}_{stab} to control hourglassing as

$$\mathbf{K} = \mathbf{K}_{\text{IGP}} + \mathbf{K}_{\text{stab}}. \quad (2.26)$$

2.5.4 Mass matrix lumping

In order to take full advantage of explicit integration, it is necessary to use a diagonal mass matrix, since the inversion is computed during time integration. The easiest method is referred as *row-sum* and its use consists of adding the off-diagonal elements to the diagonal elements separately for each row.

$$M_{aa}^{\text{diag}} = \sum_b M_{ab} \quad (2.27)$$

Unfortunately, the *row-sum* method sometimes produces negative mass - corner nodes of 8-noded serendipity elements.


Different lumping technique is *HRZ algorithm* [72], called "Special lumping technique" by Hughes in [64]. This algorithm redistributes the whole mass proportionally to the diagonal entries of the element mass matrix. Since the input consistent mass matrix is positive definite, the HRZ algorithm produces always positive lumped masses.

2.5.5 Rigid body modes filtering

Whereas in a physical experiment the observed model is somehow "softly fixed in space" and the recorded signals from transducers are relative to the model, in a numerical experiment the model floats in space and the recorded signals are relative to the default coordinate system. Therefore, the model is also undergoing rigid motion. For elimination of rigid motions or rigid body

¹Only 4-node quadrilateral elements for 2D and 8-node hexagonal elements in 3D are used here and the presented theory is generally valid only for those. For example, triangular or quadrilateral elements do not exhibit hourglass behavior, which is discussed later.

The method solves the problem $\mathbf{A}\Phi = \lambda\Phi$ using following algorithm:

1. $\Phi_0 = rand$
– generate random vector
 2. $\tilde{\Phi}_0 = \frac{\Phi_0}{|\Phi_0|}$
– norm vector
 3. $\mathbf{A}\tilde{\Phi}_0 = \Phi_1$
– multiply normed vector by matrix to get the new approximation of the eigenvector corresponding to the largest eigenvalue
 4. $\lambda_1^{\max} = |\Phi_1|$
– compute the largest eigenvalue as a norm of the new vector
 5. $\tilde{\Phi}_1 = \frac{\Phi_1}{\lambda_1}$
– norm vector
- 

The algorithm is terminated when the desired accuracy is achieved.

More effective methods exist, which are not discussed here, such as *Rayleigh quotient* based methods or *Lanczos algorithm*, [78].

2.5.6.2 Estimation of critical time step size

Computationally more efficient and therefore less time consuming method of the time step size determination is its estimation. There are two main approaches, e.i. global, and local. Global approach means that the estimator operates on whole (global) matrices of the system, while local estimators uses some local entities. Local estimators can be subdivided into elemental and nodal based on the entities they operate on.

Global approach

Estimate based on Gershgorin's circle theorem

Gershgorin circle theorem [79], also called Gershgorin disc theorem, consists of several rules. However, we are interested only in determination of the maximum eigenvalue. The theorem is used to bound the spectrum $\sigma(\mathbf{A})$ of a complex $n \times n$ matrix \mathbf{A} as

$$\sigma(\mathbf{A}) \subseteq \mathcal{S}_{\mathcal{R}} = \bigcup_{i=1}^n \mathcal{R}_i, \quad \mathcal{R}_i = \{z \in \mathbb{C} : |z - a_{ii}| \leq \sum_{j=1, j \neq i}^n |a_{ij}|\}. \quad (2.31)$$

One can imagine this as a group of circles in which all eigenvalues of our system lie. Equation (2.31) can be rewritten in more illustrative form, if we directly define Gershgorin circle

$$\mathcal{D}(a_{ii}, R_i), \quad (2.32)$$

where a_{ii} and R_i are center and radius, respectively. Center a_{ii} is a diagonal term of matrix \mathbf{A} , radius R_i is a sum of non-diagonal terms in absolute value of corresponding row or column, so

$$R_i = \sum_{j=1, j \neq i}^n |a_{ij}|. \quad (2.33)$$

Example 2.1. We have following matrix \mathbf{A} :

$$\mathbf{A} = \begin{bmatrix} 3 & -0.5 & 0.4 \\ -0.75 & 4 & -0.5 \\ 0 & -0.7 & 1 \end{bmatrix}$$

Gershgorin circles for i -th column/row are then defined for column-wise sum as

$$\mathcal{D}_{C1}(3, 0.9) \quad \mathcal{D}_{C2}(4, 1.25) \quad \mathcal{D}_{C3}(1, 0.7)$$

and for row-wise sum as

$$\mathcal{D}_{R1}(3, 0.75) \quad \mathcal{D}_{R2}(4, 1.2) \quad \mathcal{D}_{R3}(1, 0.9).$$

Graphical representation of these circles in complex plane is shown in figure 2.4.

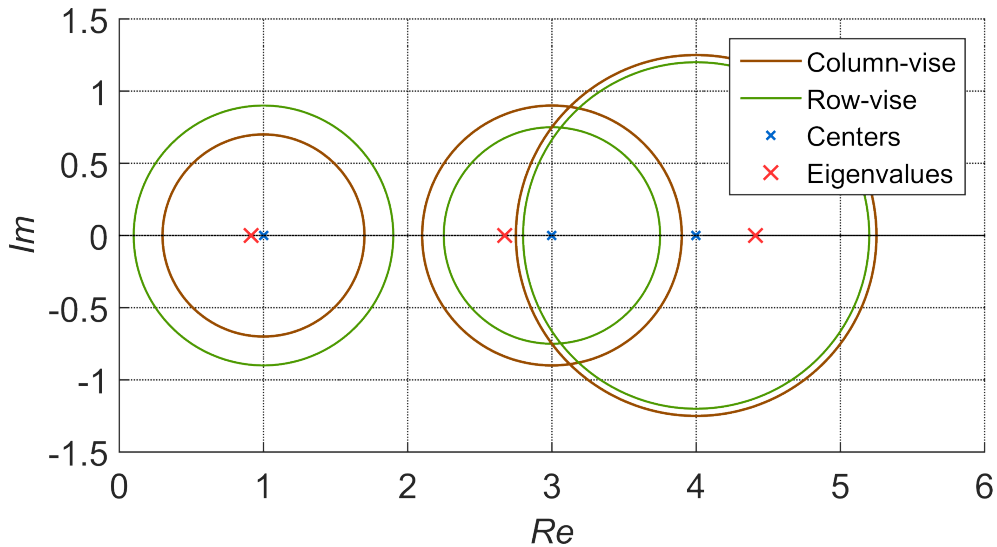


Figure 2.4: Gershgorin circles

When applied on the dynamical system (2.20), first done by Kulak [80], this method can be used for estimation of the maximum eigen-frequency. For generalized eigenvalue problem (2.30) is matrix $\mathbf{A} = \mathbf{M}^{-1}\mathbf{K}$. For lumped mass matrix the Gershgorin circle is defined as

$$\mathcal{D} \left(\frac{\mathbf{K}_{ii}}{\mathbf{M}_{ii}}, \frac{\sum_{j=1, j \neq i}^n |\mathbf{K}_{ij}|}{\mathbf{M}_{ii}} \right). \quad (2.34)$$

Based on equation (2.34) we can determine conservative estimate of maximum eigen-frequency as

$$\omega_{\max} \leq \max_i \sqrt{\frac{\sum_{j=1}^n |\mathbf{K}_{ij}|}{\mathbf{M}_{ii}}}, \quad (2.35)$$

which represents the furthest point in the unity of all circles in complex plane.

Local approach

Local approaches are established on a fact that the maximum eigenfrequency of any element is higher than the maximum eigenfrequency of the whole system,

$$\omega_{\max} \leq \max_e (\omega_{\max}^e). \quad (2.36)$$

Therefore, local estimate is always a conservative estimate. Proof of this formula can be found in [81].

Gershgorin's circle theorem on local level

Analogously, the Gershgorin's circle theorem can be applied on local level, using element stiffness and mass matrices,

$$\omega_{\max}^e \leq \max_i \sqrt{\frac{\sum_{j=1}^n |\mathbf{K}_{ij}^e|}{\mathbf{M}_{ii}^e}}. \quad (2.37)$$

Courant-Friedrichs-Lewy condition

The original form of Courant-Friedrichs-Lewy (CFL) condition [82] is

$$Co = \frac{c_L \Delta t}{\Delta x} \leq Co_{\max}, \quad (2.38)$$

where Co is a Courant number and Co_{\max} is maximum Courant number, for which central difference method remains stable. For CDM is $Co_{\max} = 1$. Δx is some distance traveled by longitudinal wave with speed c_L , Δt is time necessary for traveling distance Δx . In 1D problem Δx is the length of finite element. Hence $Co = 1$, where Co represents so called dimensionless time, means that fastest wave cannot travel a distance longer than one element, within one time step Δt . In more dimensions Δx is substituted by l_c , some characteristic dimension, which is not necessarily a trivial element dimension like length of an edge.

■ 2.5.6.3 Estimation of critical time step size in FE software (LS-Dyna)

In commercial FE software are used the previously described methods, usually with some modifications. Here we show the method of critical time step size estimation in LS-Dyna [83], which is probably most common software for

Chapter 3

Aim of the thesis

3.1 Aim

This work aims to improve the reconstruction of the exciting signal in the time domain, meaning some present or forming flaw in the material, and to determine the proper procedure for deployment of TR in practice, i.e., in commercial FE software.

3.2 Objectives

1. *Development of a numerical linear elastodynamic solver suitable for time reversal application*

Common commercial FE software does not provide full control over analysis settings and all input parameters. For this reason, own linear elastodynamic solver will be developed to control the entire process of the dynamic analysis. It will merge the desired FEM procedures with non-standard time-varying boundary conditions and automate the TR process.

2. *Development of a suitable methodology for FEM based TR (correct reconstruction of the source signal)*

Several works are dedicated to investigating or improving the quality of the reconstruction of the original source, but a methodology for performing TR in standard and widely used numerical methods such as FEM has not yet been fully established. The most important step in using TR in practice is the correctness of the reconstruction of the original source, and such a methodology will be developed. To evaluate the methodology, several cost functions will be defined.

3. *Sensitivity analysis of computational TR process*

The effect of changing the input parameters between the direct and inverse tasks, such as temperature, time step size, mesh size, number of signals used, domain shape (domain with a hole), and environmental disturbance (background noise) on the reconstruction of the original

Chapter 4

Results of the PhD research

4.1 TR-FEM solver

Taking into account the necessity of combining specific procedures to solve the chosen problem, a dynamic solver was developed in MATLAB software. In this work, the solver is called *TR-FEM*. Its capabilities are stated below and the description of the numerical procedures is covered in the theoretical part, Section 2.5.

- Linear elastodynamics – 2D + 3D
 - for 2D, plane strain, plane stress, and axial symmetry are possible
- Explicit time integration
 - *leapfrog* form of the central difference method
 - the time integration also includes Δt_{crit} estimations
 - accurate computation according to the formula $\Delta t_{\text{crit}} = \frac{2}{\omega_{\text{max}}}$ is possible
- Full and reduced integration
 - first and second order serendipity quadrilateral and hexagonal elements are implemented
- Hourglass control
 - in the form of an additional stiffness matrix
- Mass matrix lumping
 - row-sum, and HRZ algorithm
- Non-standard time-varying boundary conditions – needed for comparison with the paper in which the inspiration was found
- Rigid body modes filtering
 - for free-floating bodies
- Others: Newmark method, periodic boundary conditions (node2node), contact

4.2 Numerical simulations of the frontal problem

In this section, the frontal problem is simulated in homogeneous and heterogeneous elastic strip, since the knowledge of capabilities and limits of the FEM is a prerequisite for numerical solution of the reverse problem. Moreover, these simulations served also as a verification of the developed *TR-FEM* solver. In the publications [A1] and [A2] several solution methods (FEM, FVM, analytical solution and experimental measurement) were compared, but here only the solution with FEM is presented. Nevertheless, all used methods from the papers are compared in the figures.

This section collects the main results from two mentioned impacted papers, namely *Experimental, Analytical, and Numerical Study of Transient Elastic Waves from a Localized Source in an Aluminium Strip*, published in the Journal *Applied Acoustics* and *A Two-Layer Elastic Strip under Transverse Impact Loading: Analytical Solution, Finite Element, and Finite Volume Simulations*, published in the Journal *Mathematics and Computers in Simulation*, listed in the bibliography section as **A1** and **A2**, respectively.

4.2.1 Homogeneous elastic strip

4.2.1.1 Problem definition

The problem lies in the investigation of the transient response of an elastic strip to a transversal loading. The elastic strip was made of a homogeneous isotropic Al alloy D16-ATV. The material parameters are summarized in Table 4.1, the value of longitudinal speed c_L corresponds to plane stress conditions. Dimensions of the strip were $399 \times 50 \times 1.35$ mm. The sketch of the model is shown in Figure 4.1 [A1].

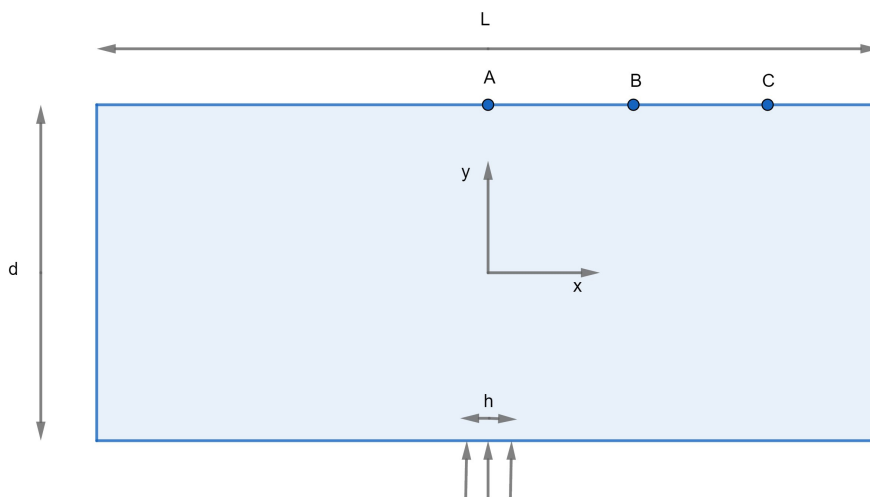


Figure 4.1: Sketch of the problem [A1].

Material	Density ρ (kg/m ³)	Young modulus E (GPa)	Poisson ratio ν	Longitudinal speed c_L (m/s)	Transversal speed c_T (m/s)
Al alloy D16-ATV	2770	72	0.333	5401	3126

Table 4.1: Material properties of the strip under investigation.

The loading signal corresponds to a smooth pulse of duration $t_0 = 9 \mu\text{s}$ with maximum amplitude $\sigma_0 = 0.72 \text{ MPa}$. The amplitude changes according to cosine train 333 kHz with 0.25 cosine window. This pulse can be expressed as

$$\sigma(t) = \begin{cases} \frac{\sigma_0}{2} \cos\left(\frac{\pi t}{30}\right) \left(1 - \cos\left(\frac{\pi t}{22}\right)\right) & \text{for } t \leq 23\Delta t, \\ \sigma_0 \cos\left(\frac{\pi t}{30}\right) & \text{for } 23\Delta t \leq t \leq 157\Delta t, \\ \frac{\sigma_0}{2} \cos\left(\frac{\pi t}{30}\right) \left(1 - \cos\left(\frac{\pi(180-t)}{22}\right)\right) & \text{for } 157\Delta t \leq t \leq 180\Delta t, \\ 0 & \text{for } t \geq 180\Delta t. \end{cases}$$

The time history of this input signal is shown in Figure 4.3 [A1] (curve *Ideal pulse*).

According to the introduced coordinate system, the stress loading $p(x, t)$ is nonzero only for $y = -d/2$ and $x \in [-h/2, h/2]$. It will be approximated by $p(x, t) = (H(x + h/2) - H(x - h/2)) \sigma(t)$, where $H(x)$ denotes the Heaviside function in x and $\sigma(t)$ stands for the ideal or real pulse from Figure 4.3 [A1]. The problem was solved as the symmetric one and the evaluation of vertical velocity component up to time $t_{\text{max}} = 750 \mu\text{s}$ was primarily made at points A, B, and C for comparison with experimental data. The position of these points is shown in Figure 4.1 [A1] and the distance between them is 13.5 mm each.

4.2.1.2 Experiment

Measurements of wave propagation in an elastic strip of finite length were done in the Laboratory of Non-Destructive Testing of the Institute of Thermomechanics of the Czech Academy of Sciences. The loading pulse was induced with the piezoelectric transducer and for the non-contact record of the response, the vibrometer was used. See the experimental setup in Figure 4.2 [A1]. Detailed description of the experiment is in [A1].

According to a more thorough experimental analysis, as presented in [A1], the input signal does not match the real signal exciting the strip (see Figure 4.3 [A1], curve *Real pulse*). This real pulse is the result of the normal velocity measurement in the center of the transducer surface using a vibrometer. The difference between the ideal pulse (input electric signal into the transducer) and real pulse (corresponding to the normal velocity measured on the transducer surface) is due to complex wave processes inside the transducer, piezo-electric response, and piezo-electric/mechanical coupling. In reality, one has to think also about a non-ideal connection between the transducer and the strip under investigation. This effect is neglected both

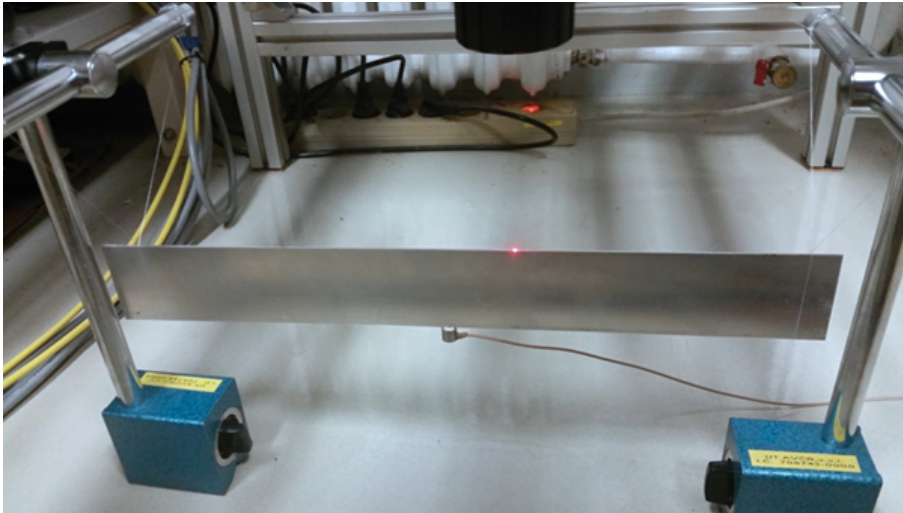


Figure 4.2: Experimental setup [A1].

in numerical and analytical solutions of the problem, so an ideal connection between the transducer and the strip is assumed.

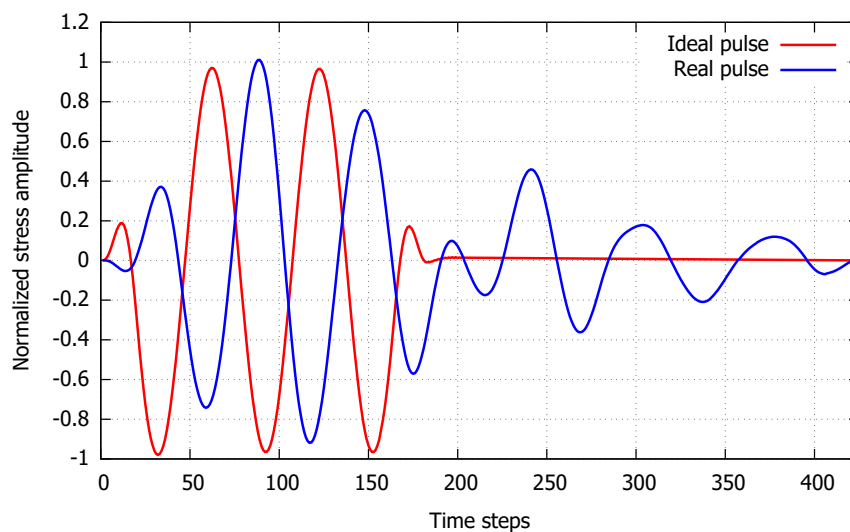


Figure 4.3: Shape of ideal and real loading pulses [A1].

4.2.1.3 Details of FE simulation

Except solution using FEM, also analytical solution and FVM were used. Generally, the figures shown below contain results of all used methods. See the description of other methods in [A1].

Due to its dimensions, the elastic strip was modeled as 2D plane stress problem. The structural FE mesh was composed of four-noded quadrilateral elements with edge length 0.25 mm, making 159 600 elements using

symmetricity. The length of the finite element edge is set considering the maximum frequency contained in the loading pulse, [76]. The lumped mass matrix was used and for evaluation of the stiffness matrix, the one-Gauss point integration with the hourglass stabilization is utilized. A more detailed description of used methods can be found in Section 2.5.

The time step size corresponds to the Courant number $Co = 0.97$.

4.2.1.4 Infinite strip

To validate the accuracy of both numerical methods, it is instructive to start with the problem of an infinite strip for which the analytical solution exists.

The computation of wave propagation in the strip under ideal loading via the normal stress shown in Figure 4.3 [A1] was performed analytically and by finite volume and finite element methods. Results of numerical simulations and analytical solution are compared at all three points. The comparison at point A that corresponds to the middle of the strip is presented in Figure 4.4 [A1]. As one can see, the results of simulations by finite volume and finite element methods are almost coinciding with the analytical solution up to 2000 time steps (100 μ s), i.e., at early stages of the signal propagation. Similar results have been obtained also for points B and C. After 2000 time steps, the results start to diverge due to the influence of lateral vertical boundaries of the strip used in numerical models. Based on this comparison, we can conclude that the chosen finite element and finite volume methods are suitable for the elastic wave propagation problem in the strip.

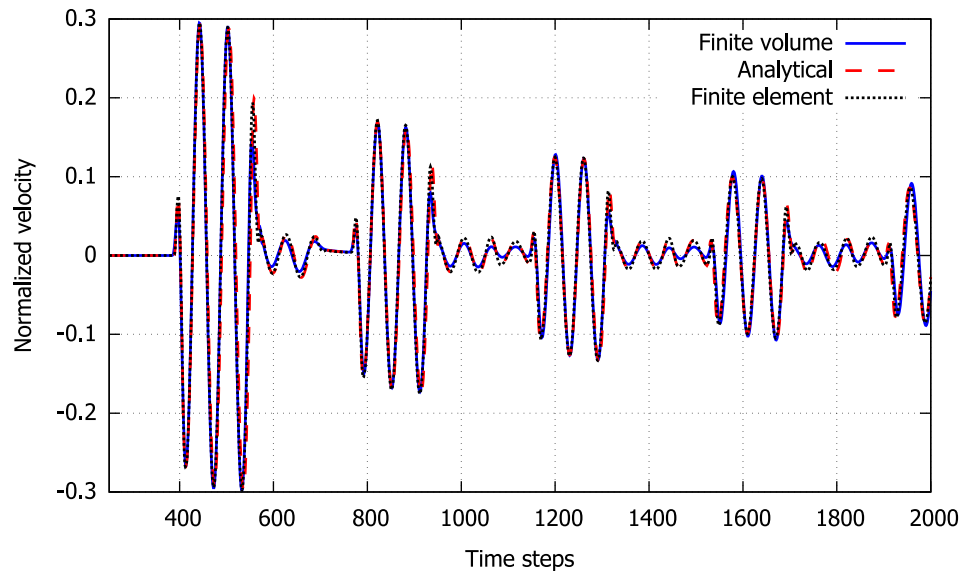


Figure 4.4: The response to the ideal pulse: analytical solution vs numerical simulations [A1].

The same coincidence between the analytical and numerical solutions was achieved also for the real pulse excitation. Making such verification of applied

approaches, the obtained results can be compared with the measured strip response to the real pulse. This comparison is presented in Figures 4.5 - 4.7 [A1] for all three studied points. Due to the mentioned coincidence between analytical and numerical solutions, only analytical and experimental results are shown.

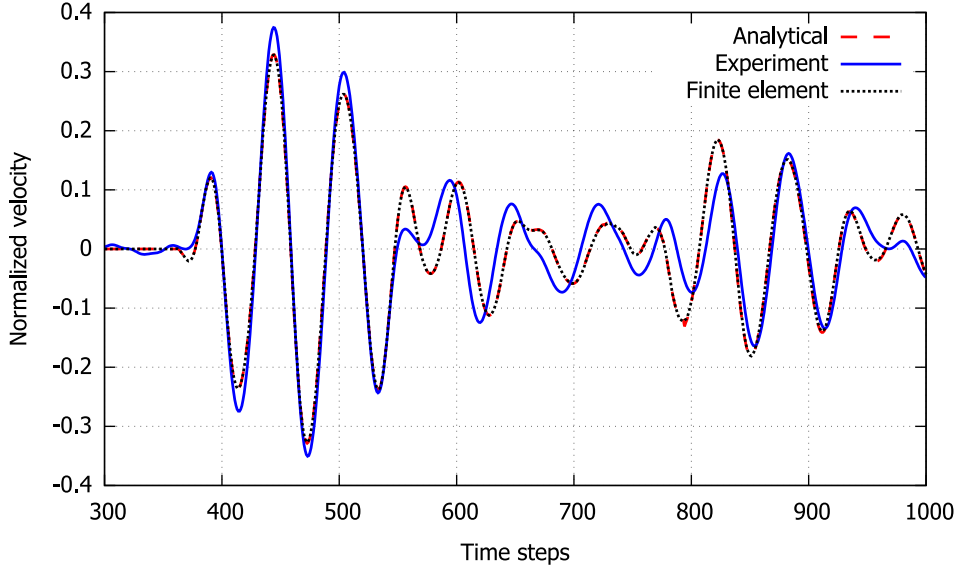


Figure 4.5: The response to the real pulse at point A: analytical and numerical solution vs experimental data [A1].

It is seen that the very good agreement with the measured data occurs for the first 1000 time steps (i.e. up to time $50 \mu s$), especially at point B (see Figure 4.6 [A1]). Considering the time history for the vertical velocity at point C (Figure 4.7 [A1]), we cannot say that the agreement with the experiment is as good as at the previous points even for the short time simulations. Also for longer times, the dispersion properties of the real strip and the real structure of the strip material make the differences between both responses more significant at all three points.

The application of the time-varying Dirichlet boundary condition for the normal velocity is also checked in the finite element simulations. The results of the time history of the normal velocity at the point B are depicted in Figure 4.8 [A1] as an example. One can see that the results for Dirichlet and Neumann boundary conditions are very close to each other. So it can be said that both types of boundary conditions can be used for correct representation of transducer loading.

Having the verified analytical and numerical models for short time response of the real strip, one can use these models to visualize the wavefield the consequences of which have been measured at the strip edge. For this purpose, the snapshots of the mean velocity $\sqrt{v_1^2 + v_2^2}$ at various time instants obtained by the analytical solution are shown in Figure 4.9 [A1]. This picture demonstrates how the wave field is varied due to reflections from upper and

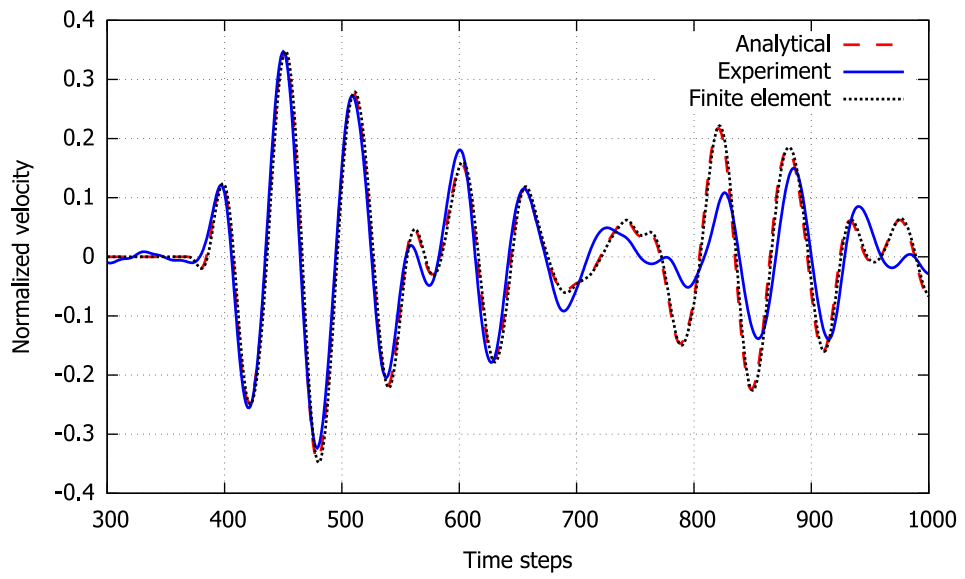


Figure 4.6: The response to the real pulse at point B: analytical and numerical solution vs experimental data [A1].

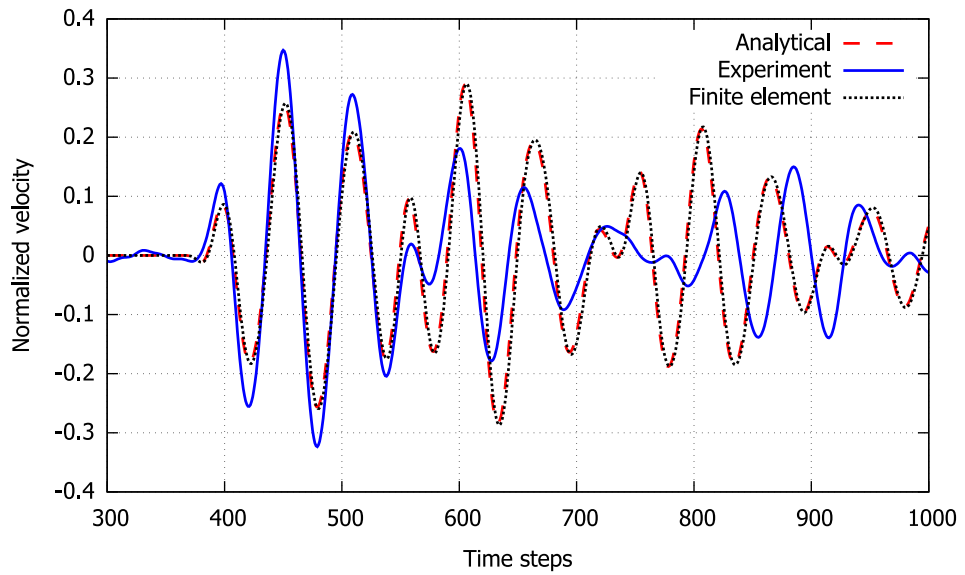


Figure 4.7: The response to the real pulse at point C: analytical and numerical solution vs experimental data [A1].

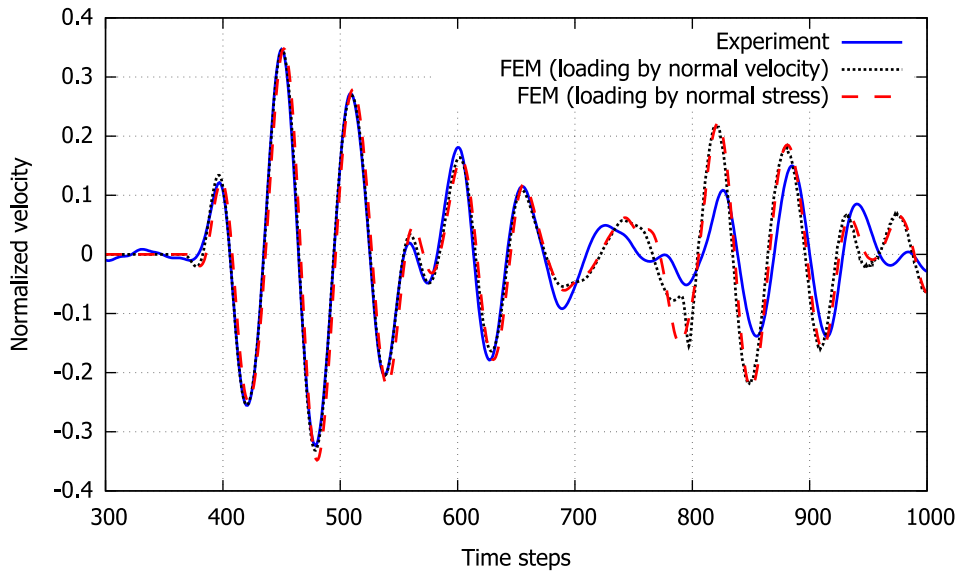


Figure 4.8: The response to the real pulse at point B obtained by the stress and velocity loading [A1].

bottom boundaries and internal interferences. A clear separation between the longitudinal wave and the pattern of remaining wave interference is observed.

4.2.1.5 Finite strip

In the case of finite strip, we need to take into account the reflections from the lateral vertical boundaries. It requires computations for a longer time. The comparison of experimental data with analytical solution and numerical results obtained by the finite element method is shown in Figure 4.10 [A1]. The results of finite volume simulation are not presented because they are nearly identical to analytical ones up to about 2000 time steps and for longer times they do not conserve the total energy of the signal. It is clear from Figure 4.10 [A1] that all results coincide quite well up to about 2500 time steps. After this time instant, the analytical solution does not represent the real response due to the absence of lateral strip boundaries influence. The results of finite element computations take the reflections from lateral boundaries into account, but uncertainties in experimental setup prevent the detailed coincidence.

In an attempt to improve the agreement between numerical simulations and experimental data, the 3D computation of the problem was performed using *TR-FEM* solver. Unfortunately, the results of 3D calculation differ from those in 2D only slightly, as it can be clearly seen in Figure 4.11 [A1]. From one side, it confirms that the applied plane stress approximation is applicable for the considered problem. From another side, it does not assure that 3D computing will improve the results of numerical modeling significantly.

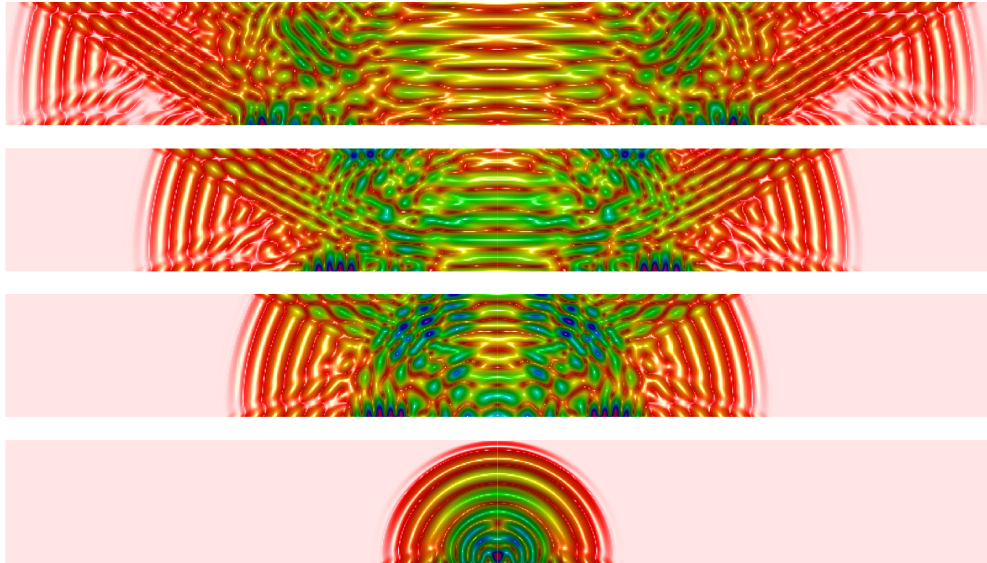


Figure 4.9: Distribution of the mean velocity $\sqrt{v_1^2 + v_2^2}$ inside the strip. Snapshots of the analytical solution for $t = \{186\Delta t, 420\Delta t, 561\Delta t, 753\Delta t\}$ [A1].

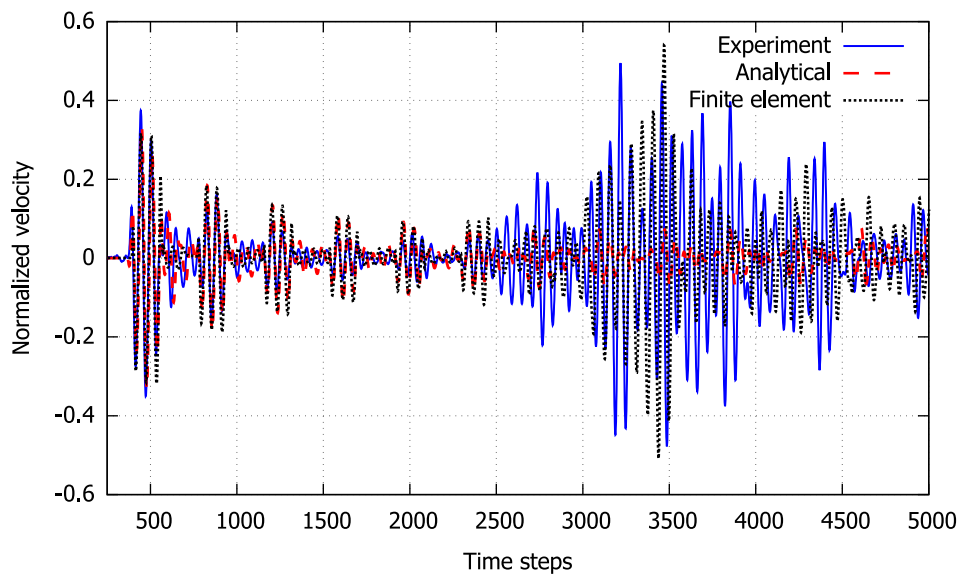


Figure 4.10: Measured response vs analytical solution and finite element computation for longer time [A1].

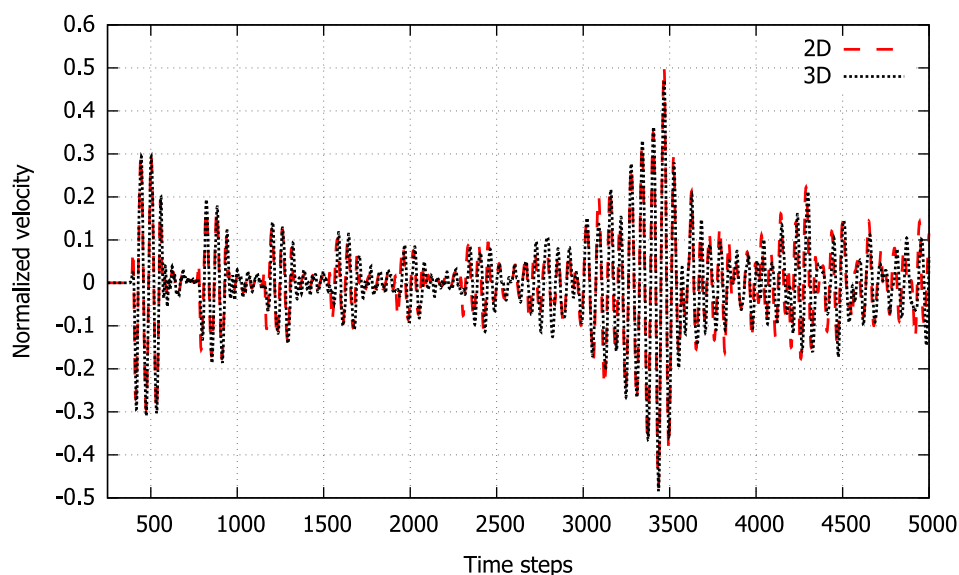


Figure 4.11: Comparison of results for finite element 2D and 3D simulation [A1].

4.2.1.6 Discussion of the homogeneous elastic strip

Experimental measurements and numerical simulations were performed to investigate the accuracy of the plane stress approximation in describing elastic waves in a finite strip. Comparison of the experimental data with the analytical solution and numerical simulations demonstrates the ability of standard numerical methods to reproduce the signal propagation in a homogeneous strip only for short-time computations. The obtained results confirm the suitability of existing non-destructive evaluation methods and raise certain questions concerning the time reversal technique using long-time computing.

4.2.2 Heterogeneous elastic strip

4.2.2.1 Problem definition

The transient response to the transversal loading of a two-layer elastic strip is considered. The sketch of the problem is shown in Figure 4.12 [A2]. The infinite elastic strip consists of two layers of different homogeneous isotropic materials, namely aluminum Al and aluminum oxide Al_2O_3 (ceramics). The bottom *layer 1* has thickness $d_1 = 30$ mm and the upper *layer 2* has thickness $d_2 = 10$ mm. The properties of the materials are given in Table 4.2. The corresponding longitudinal and transversal wave velocities are also stated there. The values of longitudinal velocity c_L in parentheses correspond to plane stress conditions. It is clear from the values specified in Table 4.2 that the composite strip is made of two materials with very different properties.

Initially, the strip is at rest. The stress loading $p(x_1, t)$, as normal pressure, is nonzero only for $x_2 = d_1 + d_2$ and for $x_1 \in [-h, h]$. All other parts of

the strip boundaries were stress-free. The shape of the loading $p(x_1, t)$ is a smooth cosine pulse of duration t_0 with the amplitude σ_0 changing according to cosine function in x_1 as

$$p(x_1, t) = \frac{\sigma_0}{2} \cos\left(\frac{\pi x_1}{2h}\right) \left(1 - \cos\frac{2\pi t}{t_0}\right) [H(t) - H(t - t_0)], \quad (4.1)$$

where $H(t)$ denotes the Heaviside step function. Corresponding parameters contained in (4.1) were the following: $h = 2 \text{ mm}$, $\sigma_0 = 10^6 \text{ Pa}$, $t_0 = 2 \cdot 10^{-6} \text{ s}$.

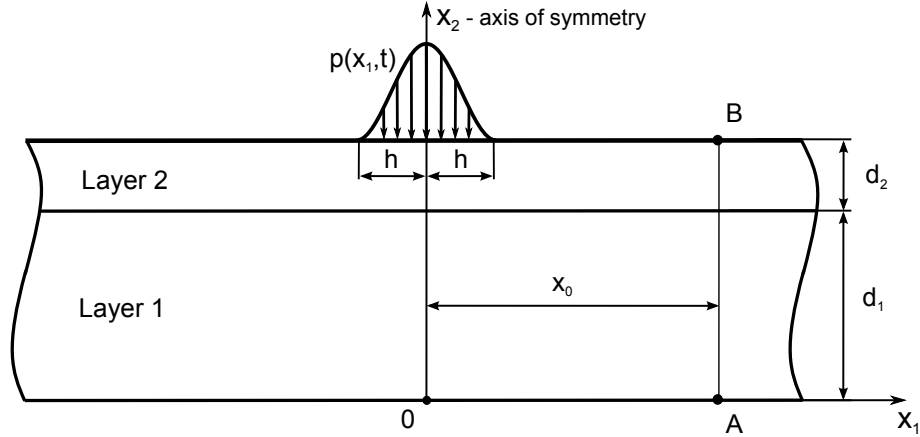


Figure 4.12: Sketch of the problem [A2].

Material	Density ρ [kg/m^3]	Young modulus E [GPa]	Poisson ratio ν	Longitudinal wave speed c_L [m/s]	Transversal speed c_T [m/s]	Source
<i>Al</i>	2700	70.6	0.345	6420 (5448)	3040	[84]
<i>Al₂O₃</i>	3970	401	0.24	10911 (10353)	6382	[85]

Table 4.2: Values of material properties.

4.2.2.2 Details of FE simulation

Because of its dimensions, the elastic strip was modeled as a 2D plane stress problem. The structured FE mesh consisted of the four-noded quadrilateral elements with an edge length of 0.2 mm, which corresponded to 120 000 elements. The length of the finite element edge was determined considering the maximum frequency contained in the loading pulse, [76]. The lumped mass matrix was used and one-point Gauss integration with the hourglass stabilization was used to evaluate the stiffness matrix. A more detailed description of used methods can be found in Section 2.5.

Based on the geometry of the problem shown in Figure 4.12 [A2], the values of the parameters used for the numerical simulations are chosen as follows:

- Loading size $h = 2 \text{ mm} = 10 \Delta x_1$;
- Strip thickness $d_1 + d_2 = 40 \text{ mm} = 200 \Delta x_1$;
- Strip length $= 120 \text{ mm} = 600 \Delta x_2$;
- Space step (mesh size) $\Delta x_1 = \Delta x_2 = 0.2 \text{ mm}$;
- Distance $x_0 = 10 \text{ mm} = 50 \Delta x_1$.

■ 4.2.2.3 Numerical results and comparison with the analytical solution

In this section, the results of numerical solution of pulse propagation in the homogeneous and heterogeneous strips are presented. The results obtained with FEM and FVM are compared with the analytical solution. The comparison of the dimensionless stress component σ_{11}/σ_0 was performed at two selected points A and B for $x_0 = 10 \text{ mm}$ (see the problem sketch in Fig 4.12 [A2]). Note that the stress components σ_{22} and σ_{12} have zero values at the points A and B , therefore only the normal stress σ_{11} is of interest.

First, the homogeneous case is presented, then two heterogeneous cases of a layered strip consisting of two different materials as specified in Section 4.2.2.1 are shown.

Homogeneous aluminum strip

The time step Δt for explicit schemes is determined by the maximum of longitudinal velocity in the studied material. Comparative studies and pitfalls of Δt_{crit} estimates were presented at conferences [A6, A7, A8, A4, A20]. For pure aluminum, the value of the longitudinal wave velocity is 5448 m/s (see Table 4.2), which determines

$$\Delta t = \Delta x_1 / c_L = 2 \cdot 10^{-4} / 5448 = 3.67 \cdot 10^{-8} \text{ s.}$$

Correspondingly, the duration of the loading is

$$t_0 = 200 / 3.67 = 54 \Delta t.$$

The characteristic time T_0 is then

$$T_0 = 0.04 / 5448 = 7.34 \cdot 10^{-6} = 200 \Delta t.$$

Calculations are performed for 500 time steps providing the absence of influence of lateral boundaries of the strip.

The results obtained are shown in Figures. 4.13–4.14 [A2]. Here, the blue lines correspond to the analytical solution, the red lines to the finite element simulation, and the magenta lines to the results of the finite volume

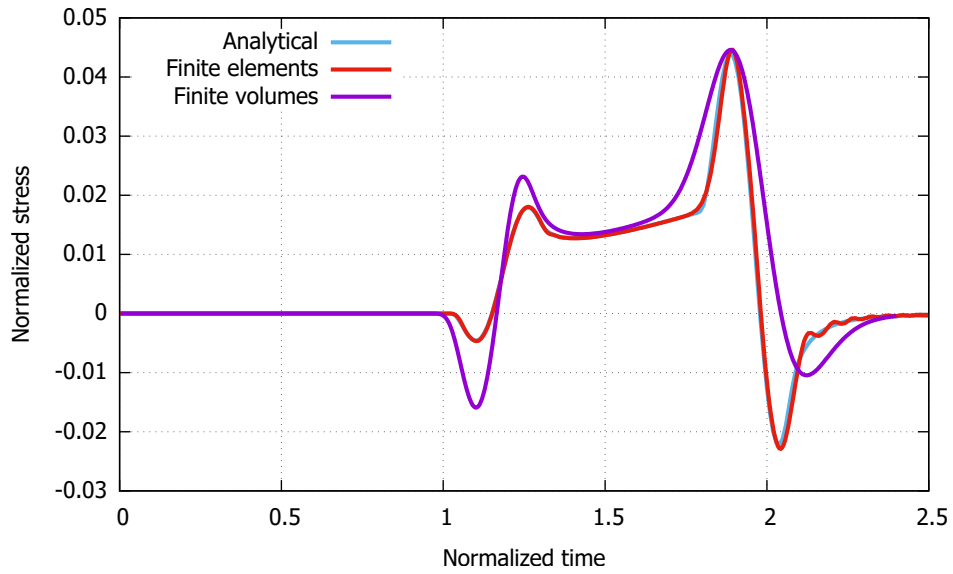


Figure 4.13: Time history of the normalized stress σ_{11} at point A in homogeneous aluminum strip [A2].

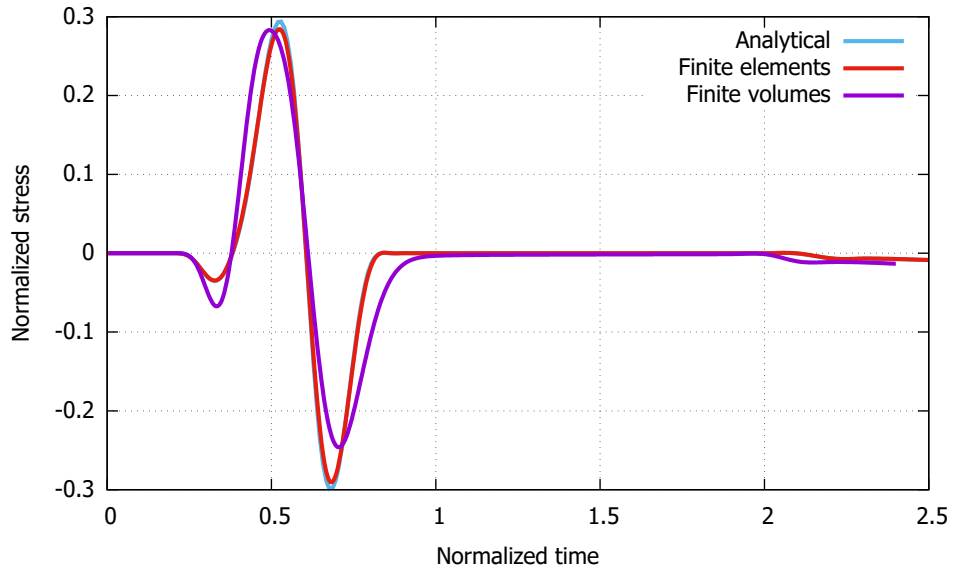


Figure 4.14: Time history of the normalized stress σ_{11} at point B in homogeneous aluminum strip [A2].

calculations. As can be seen, there is almost no difference between the results of the finite element computations and the analytical solution.

At the same time, the results of the finite volume simulation are qualitatively similar, but have quantitatively recognizable differences. The reason for this lies in the definition of the boundary conditions. For stability reasons, the finite volume calculations are performed with a value of the Courant number smaller than one. If the same size of time and space steps as in the finite

element calculations is kept, the delay in the time variation of the loading is obtained, as shown in Figure 4.15 [A2]. Here the blue line corresponds to the value of the Courant number equal to one used in the finite element solution, and the magenta line shows the representation of the same pulse for $Co = 0.83$ used in the finite volume calculations. The initial delay in the input causes the delay in the response.

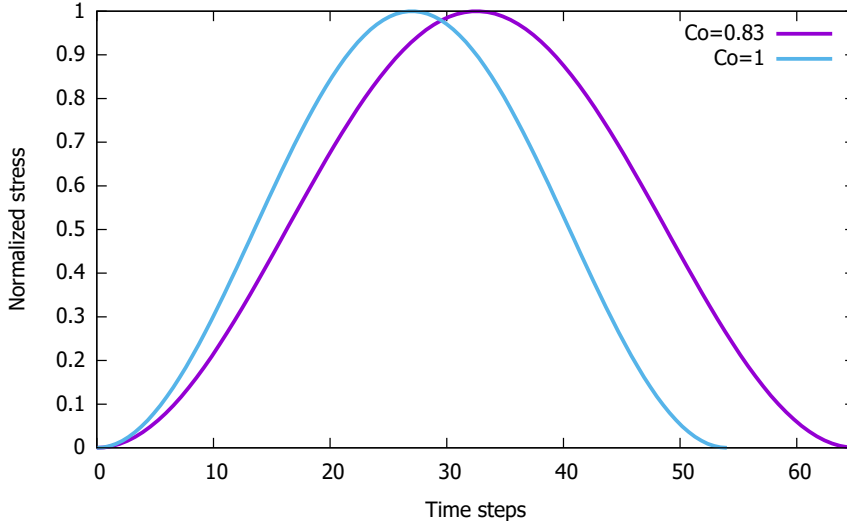


Figure 4.15: Time variation of loading pulse along the vertical central line [A2].

Composite strip $Al-Al_2O_3$

Now, the layered strip is considered, where pure aluminum is in the layer 1, and the layer 2 is made of the ceramics Al_2O_3 . The results of the numerical simulations are compared with the analytical solution. Since the longitudinal wave velocity for Al_2O_3 is 10353 m/s, the time step Δt for the simulation is

$$\Delta t = \Delta x / c_L = 2 \cdot 10^{-4} / 10353 = 1.93 \cdot 10^{-8} \text{ s.}$$

Accordingly, the duration of the loading is

$$t_0 = 200 / 1.93 = 104 \Delta t,$$

and the characteristic time T_0 is then

$$T_0 = 0.04 / 10352.8 = 3.86 \cdot 10^{-6} = 200 \Delta t.$$

The comparison of the numerical and analytical solutions for the time history of the normalized stress σ_{11} at points A and B, in this case, is presented in Figures 4.16–4.17 [A2]. The finite element and analytical results are practically coincided in this case. Even finite volume calculations are closer to analytical and finite element outcomes.

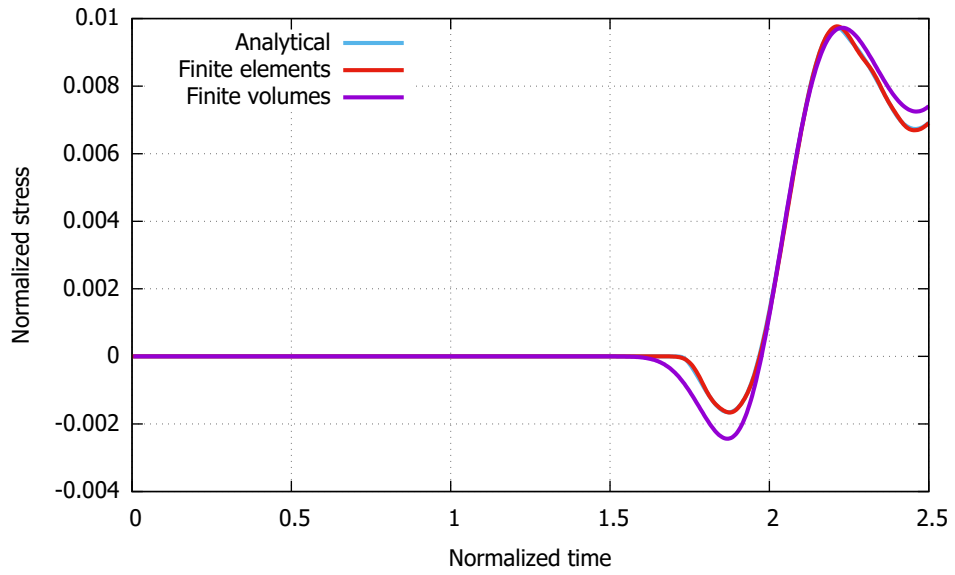


Figure 4.16: Time history of the normalized stress σ_{11} at point A in two-layer $Al-Al_2O_3$ strip [A2].

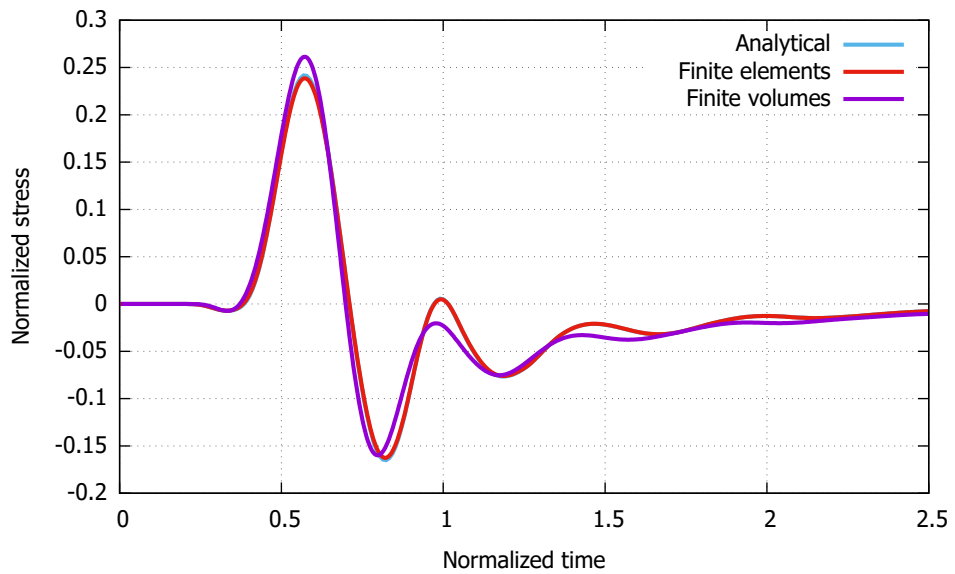


Figure 4.17: Time history of the normalized stress σ_{11} at point B in two-layer $Al-Al_2O_3$ strip [A2].

Composite strip Al_2O_3-Al

Now, the layers are swapped to see how this affects the comparison. This means that the layer 1 is made of the ceramic Al_2O_3 and the layer 2 is made of pure aluminum. The parameters used in the simulations are the same as in the previous case because only the placement of layers is changed. The

comparison of numerical and analytical solutions for the time history of the longitudinal stress at points A and B is presented in Figures 4.18–4.19 [A2].

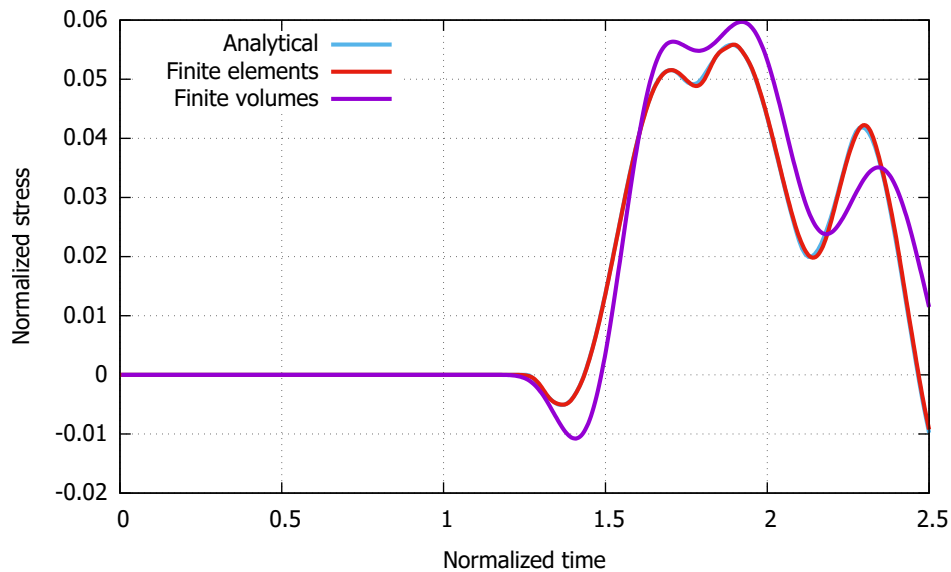


Figure 4.18: Time history of the longitudinal stress at point A in two-layer Al_2O_3 – Al strip [A2].

Again, the blue lines in mentioned figures correspond to the analytical solutions, the red lines show the results of the finite element computations and the magenta lines denote the results of the finite volume calculations. It is clear that the variation of stresses in time has changed, but the finite element results are in a perfect agreement with the analytical ones. As before, the finite volume calculations provide less accurate results for the reasons mentioned above.

Figure 4.20 shows the equivalent stress field at a given time for all three compositions of the two-layer strips. The stress values were mapped to the z -direction and used as a deformation vector to visualize the difference between the simulated compositions. Each strip has its own color bar defined by the maximum stress value, but the scale of deformation is the same for all cases. It is apparent that the velocity of waves and stress magnitude vary in different materials and that the reflections occur at the interface. This well-known phenomenon can be used, e.g., in stress attenuators.

4.2.2.4 Discussion of the heterogeneous elastic strip

Numerical simulations using finite element and finite volume methods were performed and the results were compared with the analytical solution. From the results, it appears that FEM is able to represent more accurately the wave propagation in elastic material. A more detailed study would be required for firmer conclusions.

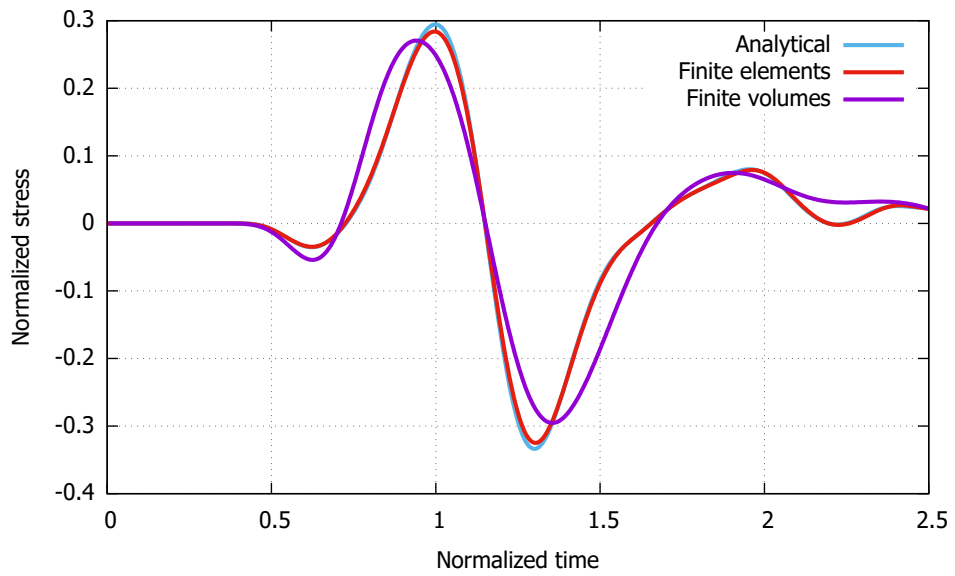


Figure 4.19: Time history of the longitudinal stress at point B in two-layer Al_2O_3 -Al strip [A2].

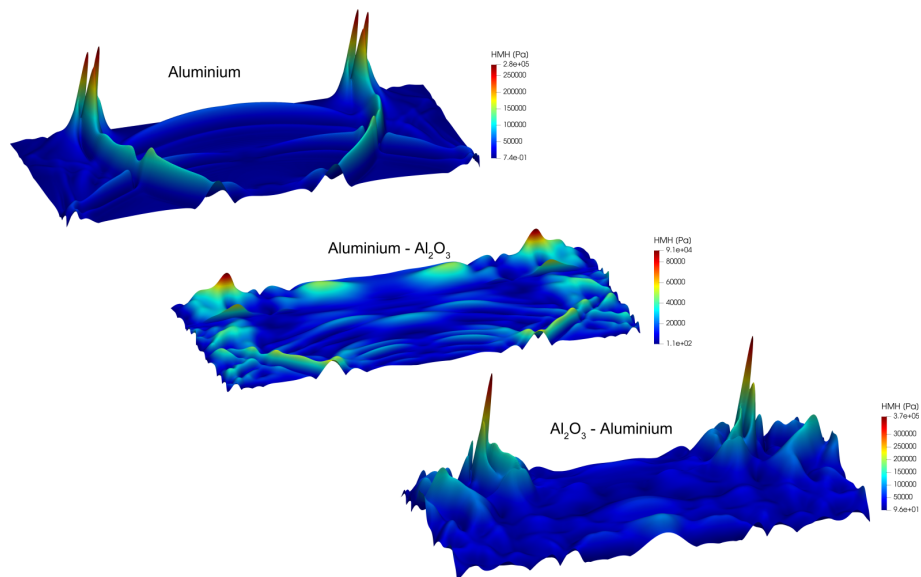


Figure 4.20: The equivalent stress field (mapped to the z-direction) at certain time for all three compositions of two-layer strip.

4.3 Numerical simulation of the reverse problem

In this section, a purely numerical solution of the full TR process is carried out. First, two types of loading/ boundary conditions are defined, as well as the cost functions to evaluate the quality of the reconstruction. Next, after the problem definition, the test of refocusing is performed, followed by the test of reconstruction from which the new methodology emerged. The section ends with tests of the numerical sensitivity of the proposed methodology.

This section is based on the results of the paper *Finite Element Method Based Computational Time Reversal in Elastodynamics: Refocusing, Reconstruction and Its Numerical Sensitivity*, published in the Journal *Mathematics and Computers in Simulation*, listed in the bibliography section as **A3**.

It is assumed that only the normal component of the velocities $\dot{\mathbf{u}}_m(\mathbf{x}, t)$ at the boundary $\partial\Omega_m$ is recorded as the response of the frontal problem. This simulates recording the response in terms of normal velocities at $\partial\Omega_m$ by piezo-sensor or other measurement techniques. Then, $\dot{\mathbf{w}}_m(\mathbf{x}, \tau)$ is computed via (2.19d). This process is called *time reversal of signal*. In this way the 'experimental data' for the TR task defined in (2.19d) are generated by the numerical model. Then, the boundary conditions must be applied in a suitable form to the reverse problem. For the application of the boundary conditions in Ω_m in the FE simulation, two forms are considered, only on $\partial\Omega_m$, as

Type I: loading by normal velocity components in the Dirichlet sense

$$\dot{\mathbf{w}}_m^n(\mathbf{x}, \tau) \quad \mathbf{x} \in \partial\Omega_m, \quad 0 \leq \tau \leq T, \quad (4.2a)$$

Type II: loading by normal stress components in the Neumann sense

$$\boldsymbol{\sigma}_m^n(\mathbf{x}, \tau) = \boldsymbol{\sigma}_m^n(\mathbf{x}, \tau)\mathbf{n} = A\dot{\mathbf{w}}_m^n(\mathbf{x}, \tau) \quad \mathbf{x} \in \partial\Omega_m, \quad 0 \leq \tau \leq T. \quad (4.2b)$$

Here, \mathbf{n} is the outward normal direction to the boundary $\partial\Omega_m$. A is a constant with a suitable value depending on the material parameters. For this normal traction loading $\boldsymbol{\sigma}_n$ the external nodal force vector is generated as \mathbf{f}_{ext} . This process can be viewed as a transfer of the Dirichlet boundary conditions of velocity $\dot{\mathbf{w}}_m^n$ meaning to Neumann boundary condition as normal stress $\boldsymbol{\sigma}_m^n$ in $\partial\Omega_m$.

Remark 1: If $\Omega_m = \Omega$, an exact reconstruction of the initial wavefield $\mathbf{u}(\mathbf{x}, t = 0)$ can be found. In this case, $\Omega_m \subset \Omega$, where we have only partial information of the wavefield, $\dot{\mathbf{u}}_m(\mathbf{x}, t)$, the reconstructed wavefield is only an approximation of the initial state $\mathbf{u}(\mathbf{x}, t = 0)$.

4.3.1 Loading and boundary conditions

To solve the system (2.20), the suitable Dirichlet and Neumann boundary and initial conditions for frontal and reverse problems should be included. In the finite element method, the kinematic boundary conditions can be prescribed by given nodal displacements, velocities or accelerations, for details see [64] or [86].

In the following two algorithms, the prescribed quantities in CD schemes are meant to be prescribed only at some nodes. This effect is not additionally emphasized in the symbols used for better readability. Also, the asterisk in the lower index, \square_* , denotes the prescribed value in the corresponding time, and the symbol $:=$ denotes the assignment of the prescribed value.

Application of 'loading' Type I

The CD scheme (Algorithm 1) was modified in order to include the measurement data in the form of normal velocities $\dot{\mathbf{w}}_{\text{normal}}$ as Type I. The following algorithm (4.3a)–(4.3e) shows the use of the CD scheme with marked points where the desired values of velocity at the boundary $\partial\Omega_m$ are prescribed as $\dot{\mathbf{u}}_*$.

Application of 'loading' of **TYPE I**:

$$\dot{\mathbf{u}}\left(t + \frac{\Delta t}{2}\right) = \dot{\mathbf{u}}(t) + \ddot{\mathbf{u}}(t)\frac{\Delta t}{2} \quad (4.3a)$$

apply prescribed nodal velocity as

$$\dot{\mathbf{u}}\left(t + \frac{\Delta t}{2}\right) := \dot{\mathbf{u}}_*\left(t + \frac{\Delta t}{2}\right) \text{ at } \partial\Omega_m$$

$$\mathbf{u}(t + \Delta t) = \mathbf{u}(t) + \dot{\mathbf{u}}\left(t + \frac{\Delta t}{2}\right) \Delta t \quad (4.3b)$$

$$\mathbf{r}(t + \Delta t) = \mathbf{f}_{\text{ext}}(t + \Delta t) - \mathbf{K}\mathbf{u}(t + \Delta t) \quad (4.3c)$$

$$\ddot{\mathbf{u}}(t + \Delta t) = \mathbf{M}^{-1}\mathbf{r}(t + \Delta t) \quad (4.3d)$$

$$\dot{\mathbf{u}}(t + \Delta t) = \dot{\mathbf{u}}\left(t + \frac{\Delta t}{2}\right) + \ddot{\mathbf{u}}(t + \Delta t)\frac{\Delta t}{2} \quad (4.3e)$$

apply prescribed nodal velocity as

$$\dot{\mathbf{u}}(t + \Delta t) := \dot{\mathbf{u}}_*(t + \Delta t) \text{ at } \partial\Omega_m$$

Application of 'loading' Type II

In Type II, loading in the form of a prescribed external nodal force $\mathbf{f}_{\text{ext},*}$ is assumed at $\partial\Omega_m$ due to a normal traction loading with the given time history. In the same principle as in the previous text, the following five equations (4.4a)–(4.4e) show the same algorithm with a point at which the desired values of nodal force are prescribed.

Application of 'loading' of **TYPE II**:

$$\dot{\mathbf{u}}\left(t + \frac{\Delta t}{2}\right) = \dot{\mathbf{u}}(t) + \ddot{\mathbf{u}}(t) \frac{\Delta t}{2} \quad (4.4a)$$

$$\mathbf{u}(t + \Delta t) = \mathbf{u}(t) + \dot{\mathbf{u}}\left(t + \frac{\Delta t}{2}\right) \Delta t \quad (4.4b)$$

apply prescribed nodal force as

$$\mathbf{f}_{\text{ext}}(t + \Delta t) := \mathbf{f}_{\text{ext}}(t + \Delta t) + \mathbf{f}_{\text{ext},*}(t + \Delta t) \text{ at } \partial\Omega_m$$

$$\mathbf{r}(t + \Delta t) = \mathbf{f}_{\text{ext}}(t + \Delta t) - \mathbf{K}\mathbf{u}(t + \Delta t) \quad (4.4c)$$

$$\ddot{\mathbf{u}}(t + \Delta t) = \mathbf{M}^{-1}\mathbf{r}(t + \Delta t) \quad (4.4d)$$

$$\dot{\mathbf{u}}(t + \Delta t) = \dot{\mathbf{u}}\left(t + \frac{\Delta t}{2}\right) + \ddot{\mathbf{u}}(t + \Delta t) \frac{\Delta t}{2} \quad (4.4e)$$

In the following text, both approaches to the application of boundary conditions are tested.

Remark 2: If the prescribed velocity is updated with the desired value as in [44], i.e. $\dot{\mathbf{u}}^t := \dot{\mathbf{u}}^t + \dot{\mathbf{u}}_*^t$, with a scaling parameter \mathcal{C} , while the choice of \mathcal{C} is subjected to preservation of the linear momentum balance, then for one node as a mass point with the mass m the relation obtained is

$$\dot{\mathbf{u}}^{t+\frac{\Delta t}{2}} := \dot{\mathbf{u}}^t + \mathcal{C} \cdot \dot{\mathbf{u}}_*^{t+\frac{\Delta t}{2}}. \quad (4.5)$$

Then the impulse-momentum theorem is used

$$\mathbf{I}_f = \int_t^{t+\Delta t} \mathbf{f}_*(t) dt = \mathbf{p}(t + \Delta t) - \mathbf{p}(t) = \Delta \mathbf{p} = m \Delta \dot{\mathbf{u}} \quad (4.6)$$

where \mathbf{I}_f is the impulse of the force and \mathbf{p} is the linear momentum defined as $\mathbf{p} = m\dot{\mathbf{u}}$. Respecting using half-steps for prescription of the velocity, the relation derived is

$$\frac{\Delta t}{2} \mathbf{f}_* \equiv m \cdot \Delta \dot{\mathbf{u}}_{* \frac{\Delta t}{2}}, \quad (4.7)$$

where m is nodal mass, $\Delta \dot{\mathbf{u}}_{* \frac{\Delta t}{2}}$ is the change of the nodal velocity between times t and $t + \frac{\Delta t}{2}$ from the equation (4.5), and f_* is the acting equivalent nodal force. Hence, coefficient $\mathcal{C} = \frac{2 \cdot m}{\Delta t}$. It is apparent that with this way of prescription of the nodal velocity with updating $\dot{\mathbf{u}}^t := \dot{\mathbf{u}}^t + \mathcal{C} \dot{\mathbf{u}}_*^t$ the same result is obtained, with numerical accuracy, as with the loading by the corresponding nodal force \mathbf{f}_* and no further scaling of the recorded signals is necessary. Due to the linearity of the problem, using \mathcal{C} with different value leads to the same signal with different magnitude.

4.3.2 Definition of cost functions

In this section, three local cost functions C_i and one global cost function C_G are defined as the norm for measurement of distance/nearness of two functions of interest – lower value of the cost function means more accurate reconstruction in TR. For all costs only, y-component of the reconstructed

nodal velocity is considered. The inspiration for the definition of the cost functions was found in [44], but here the distribution of some quantities of interest in time is observed. The reconstructed signal is expected to appear at the right position at the right time, and the quality of the reconstruction under these conditions is measured. This assumption is confirmed in Section 4.3.4.

To define the cost functions, the reconstructed signal is divided into three sections called time windows - $W0$, $W1$ and $W2$, see Figure 4.21 [A3] with an example. The time window $W0$ (hatched) is cut off, since only the developed signal provides relevant information, $W1$ (light gray) can be referred to as the window of the delivering signal, and $W2$ (dark gray) is the time window with the expected reconstructed pulse. The time window $W2$ has the same length as the loading signal L in the frontal problem. These costs operate with known source and cannot be used in a real TR problem with experimental data, since the source signal and thus the division into time windows is not known in advance. In the following text, the local cost functions C_i and the global cost function C_G used are described.

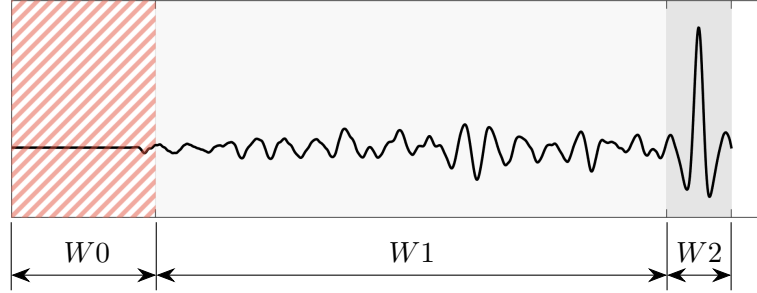


Figure 4.21: Time windows for cost functions C_i [A3].

The cost function C_1 represents a ratio of *kinetic energies* of the observed FE nodes in the time windows $W1$ and $W2$. This so-called kinetic energy is computed as the root mean square (RMS) of the velocity in the corresponding time window. This procedure is known in signal processing as *signal to noise ratio*, [87]. The cost C_1 simply tells whether the reconstructed pulse is distinguishable from the surrounding signal as

$$C_1 = \frac{\text{RMS}_{W1}}{\text{RMS}_{W2}}. \quad (4.8)$$

The cost C_2 measures the perpendicularity of the original pulse and the reconstructed pulse, or more precisely, their parallelism. The vector of the original pulse L and the vector of the reconstructed pulse $W2$ form an angle ϕ , while the calculation of $\cos \phi$ is according to a well-known formula from linear algebra described in (4.9), see e.g. [78], so

$$C_2 = 1 - \cos \phi = 1 - \frac{W2 \cdot L}{|W2| \cdot |L|}. \quad (4.9)$$

The cost C_3 measures how the reconstructed pulse is shifted in time by comparing the time positions of the maximum peaks of the original pulse

and the reconstructed pulse. To calculate this cost, it is assumed that the time window $W2$ starts at time $t = 0$ s. Here $t_{\max L}$ and $t_{\max W2}$ are the time positions of the maximum peak of the loading pulse and the reconstructed pulse, $lenL$ is the length of the loading pulse (and also of the time window $W2$). Since the maximum peak of the loading pulse is right in the middle of the signal, only half of the total length is taken as a possible shift in time. This results in the cost C_3 as

$$C_3 = \frac{|t_{\max L} - t_{\max W2}|}{lenL/2}. \quad (4.10)$$

Remark 3: Using the cost functions C_1 , C_2 and C_3 , where the known time window $W2$ is needed, has limitation for real applications. In this work, they are used for measuring the quality of reconstruction of known original sources, where the time windows of the signals are defined.

For the evaluation of the numerical tests, the global cost function C_G is used, which is defined by the following equation

$$C_G = \frac{1}{\sum w_i} (w_1 C_1 + w_2 C_2 + w_3 C_3), \quad (4.11)$$

where w_i are weights of the local costs. Since the focus is on signal reconstruction, more importance is given to the cost C_2 . Therefore, the weights are set as follows: $w_1 = 1$, $w_2 = 2$, and $w_3 = 1$.

4.3.3 Problem definition

For all the following numerical experiments in this section (Section 4.3), a two-dimensional square domain under plane stress condition with stress-free boundary is considered, see its dimensions in Figure 4.22 [A3]. In this figure, the \mathcal{A} and \mathcal{B} regions mark the position of application of the original source and the position where the response is recorded, respectively. The locations of these regions were chosen arbitrarily, but \mathcal{B} should belong to the boundary. In \mathcal{A} , 3×3 nodes are prescribed the loading, while in \mathcal{B} , the number of nodes varies and is specified in each task description. The length of the element edge is 0.4 mm, thus the FE mesh consists of 62,500 bilinear four-noded elements. The mesh was defined with respect to the maximum frequency contained in the loading signal and the dispersion behavior of the finite element method, see [88, 76], or [A5, A9, A10].

A linear homogeneous isotropic material is assumed with Young's modulus $E = 2 \cdot 10^{11}$ Pa, Poisson's ratio $\nu = 0.3$, and mass density $\rho = 7,850$ kg·m⁻³, with neither material nor numerical damping. The longitudinal wave speed for plane stress problem is given as $c_L = \sqrt{\frac{E}{(1-\nu^2)\rho}} \doteq 5,291.3$ m·s⁻¹. Time step size Δt is set to $4.009 \cdot 10^{-8}$ s resulting in the Courant number $Co \doteq 0.75$, where the Courant number is defined as $Co = \Delta t c_L / H$, see [82]; H is the characteristic dimension of the finite element, given as $H = A/D$, where A is the area of the element and D is the length of its longest diagonal, see [83].

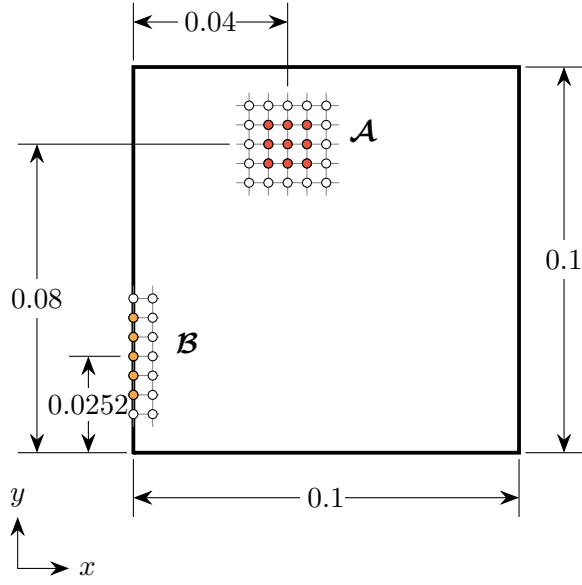


Figure 4.22: Scheme of the domain of interest, [m] [A3].

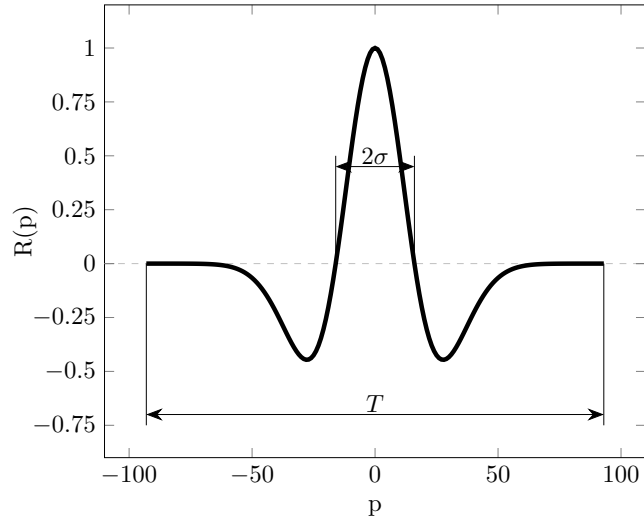


Figure 4.23: Loading Ricker pulse with its parameters [A3].

For loading function $\mathbf{f}_{\text{ext}}(t) = A_0 R(t)$ in the region \mathcal{A} , where A_0 is the amplitude of loading, the Ricker pulse (Ricker wavelet) is used, [89], which is given by a parametric formula with parameter p as

$$R(p) = -\frac{\sqrt{2\pi} \cdot \sigma \cdot \left(\left(\frac{p}{\sigma}\right)^2 - 1\right) \cdot e^{\left(-0.5 \cdot \left(\frac{p}{\sigma}\right)^2\right)}}{\sqrt{2\pi} \cdot \sigma}, \quad (4.12)$$

where $\sigma = 16 \cdot \Delta t$ and $p = \langle -93, 93 \rangle \cdot \Delta t$, the transformation between parameter p and time t is $t = p + 93 \cdot \Delta t$, and T is then 7.49683^{-6} s, see Figure 4.23. Amplitude $A_0 = 1$ in all numerical experiments.

The Ricker pulse was chosen for the reason that this pulse is symmetrical and also the areas above and below the horizontal zero line are the same. This means that the total impulse of the pulse is equal to zero. This implies that loading with a Ricker pulse does not accelerate a free body and all kinematic quantities have a meaningful value. On the contrary, a general loading signal accelerates a free body in space. In order to analyze the results, one must deal with this rigid body motion, e.g. as described in Section 2.5.5.

4.3.4 Refocusing test

In the frontal problem, the loading of TYPE I and TYPE II are applied, prescribing the y-component of the velocities or the y-component of the nodal forces at the nodes of the region corresponding to \mathcal{A} , see Figure 4.22 [A3], where the time function has the form of the Ricker pulse. The loading applied in the region \mathcal{A} generates wave processes and the normal velocities in the region \mathcal{B} are recorded. Then, the loading via TYPE I (applied normal velocity) and TYPE II (applied traction normal force) generates the reverse wave processes and refocusing can be observed in the region of the original source, \mathcal{A} . The amplitudes of loading via TYPE I and TYPE II have been set so that they are not affected by rounding errors, taking advantage of the linearity of our problem. The aim of this study is to show that the maximum peak is reconstructed at the location of the original source, \mathcal{A} , and at the correct time.

Figure 4.24 [A3] shows a snapshot of the y-component of the velocity and the total energy per volume for the frontal problem with the loading of TYPE I at the time $94 \Delta t$, which corresponds to the highest peak of the loading function - Ricker pulse. In Figure 4.25 [A3], snapshots of the reconstructed quantities, namely the y-component of velocity and total energy per volume, are presented for several times, where T_M means the time of the highest peak of the reconstructed wavefield. The loading is of TYPE I - loading by the prescribed normal velocity. It can be seen that backpropagation leads to refocusing of the original source at the correct position. The same results, see Figure 4.26 [A3], are obtained for the task with loading of TYPE II given as the loading by prescribed normal stresses in the form of nodal forces in the direction of outward normal to the surface $\partial\Omega_m$ related to the region \mathcal{B} . Figures 4.25 and 4.26 [A3] also show how the reconstructed maximum peak forms its shape from times " $t = T_M - 40 \Delta t$ " to " $t = T_M$ ", and how it vanishes in times " $t = T_M + 10 \Delta t$ " and " $t = T_M + 20 \Delta t$ ". In all sub-figures on the left, only y-component of velocity is shown and is mapped into the z-direction for illustration.

Based on these results for the both loading types, it can be seen that the localization of the original source by FEM based TR works very well. It is therefore possible to continue with the reconstruction of the source in the time domain and observe the reconstructed signal directly in the region \mathcal{B} .

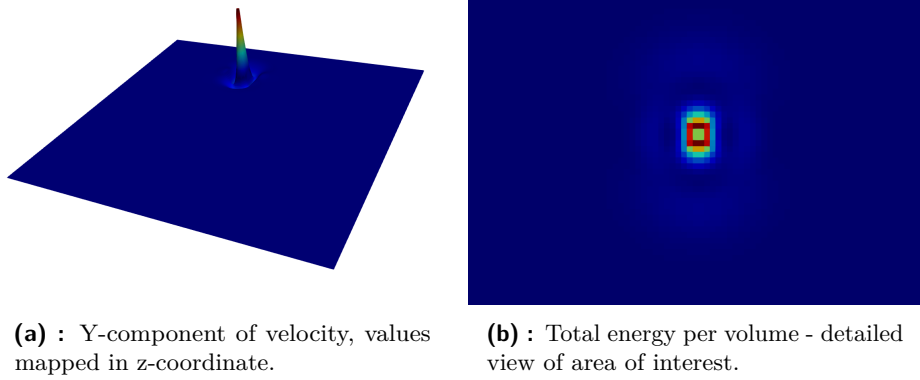


Figure 4.24: A snapshot of y-component of velocity and total energy per volume distribution from the frontal problem for time $94 \Delta t$ corresponding to the maximum peak of loading pulse [A3].

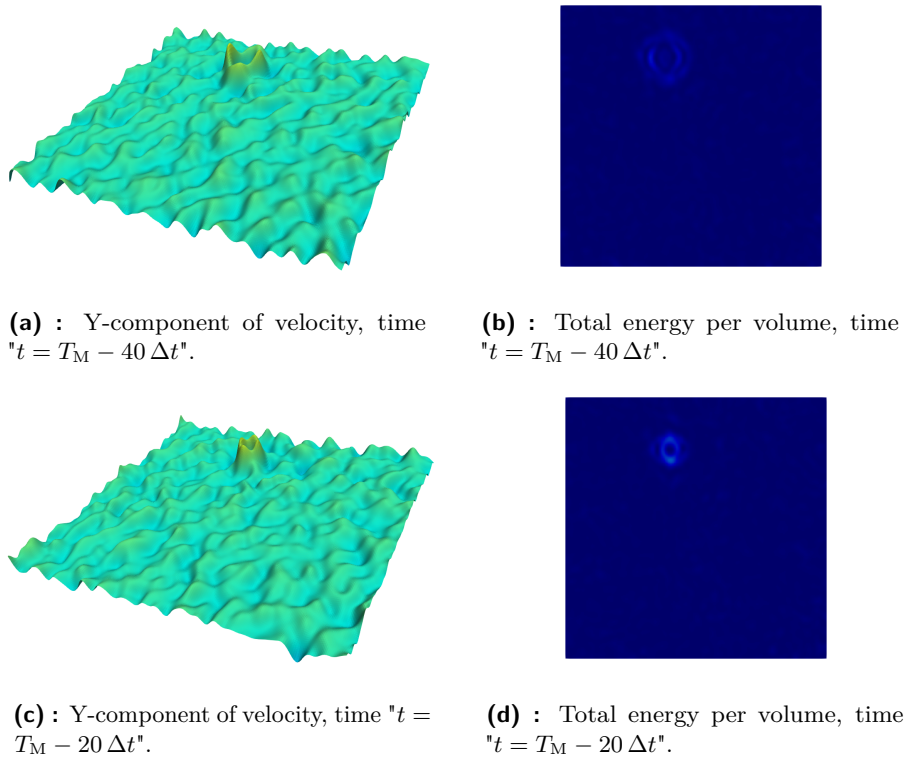
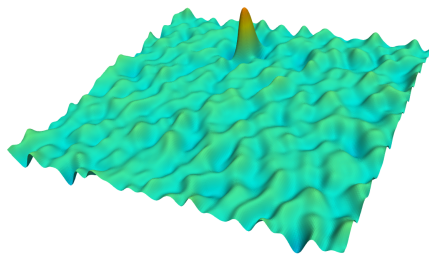
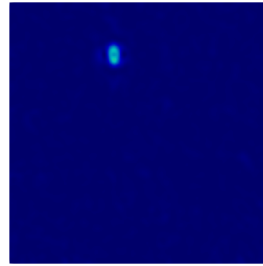


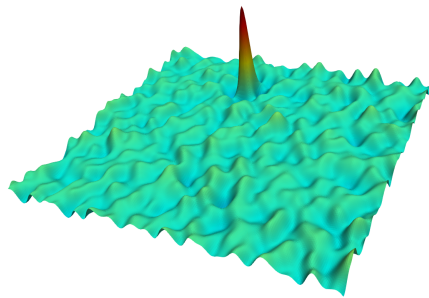
Figure 4.25: A snapshot of reconstruction of y-component of velocity and total energy per volume distribution from the reverse problem for time of maximum peak T_M and several other times; loading by TYPE I. - "velocity loading", computational time $T = 100,000 \Delta t$ [A3].



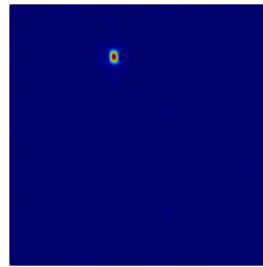
(e) : Y-component of velocity, time " $t = T_M - 10 \Delta t$ ".



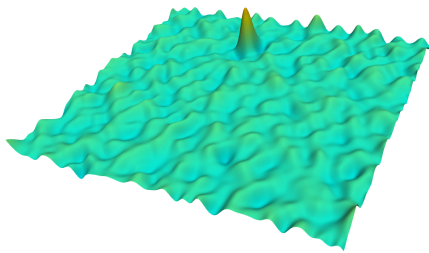
(f) : Total energy per volume, time " $t = T_M - 10 \Delta t$ ".



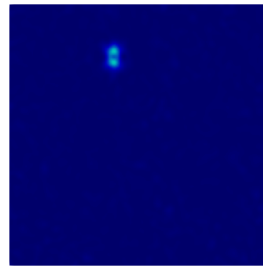
(g) : Y-component of velocity, time " $t = T_M$ " - maximum peak.



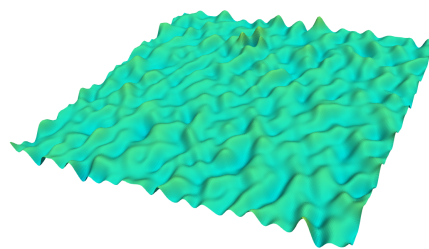
(h) : Total energy per volume, time " $t = T_M$ " - maximum peak.



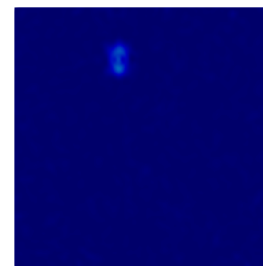
(i) : Y-component of velocity, time " $t = T_M + 10 \Delta t$ ".



(j) : Total energy per volume, time " $t = T_M + 10 \Delta t$ ".



(k) : Y-component of velocity, time " $t = T_M + 20 \Delta t$ ".



(l) : Total energy per volume, time " $t = T_M + 20 \Delta t$ ".

Figure 4.25: A snapshot of reconstruction of y-component of velocity and total energy per volume distribution from the reverse problem for time of maximum peak T_M and several other times. Loading by TYPE I - "velocity loading", computational time $T = 100,000 \Delta t$ [A3].

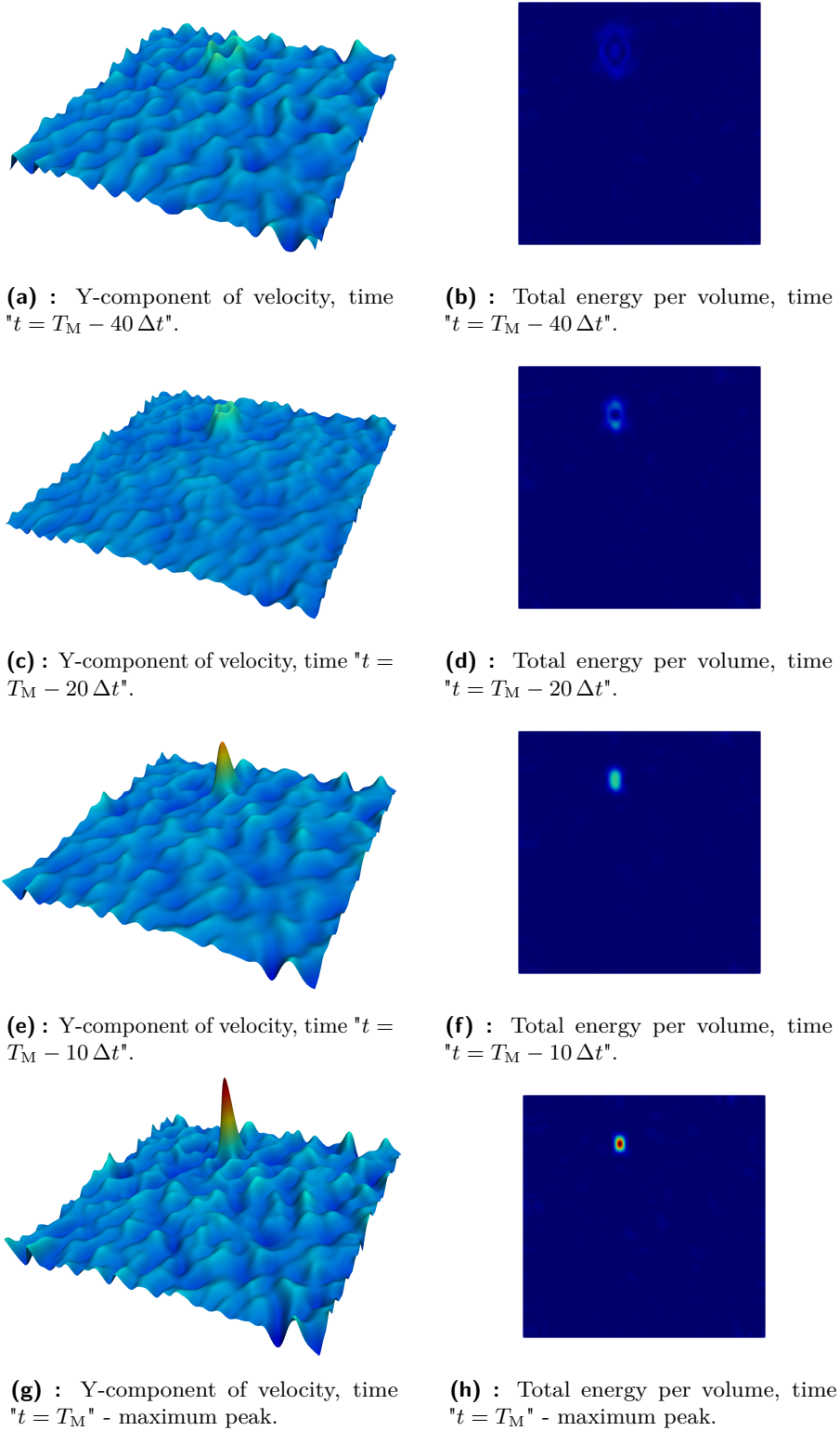
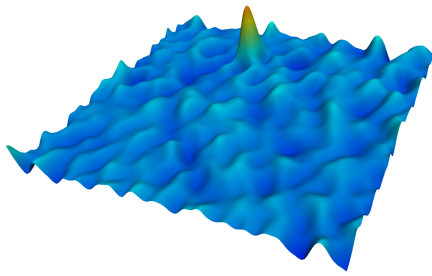
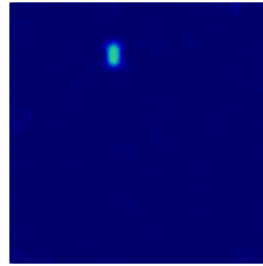


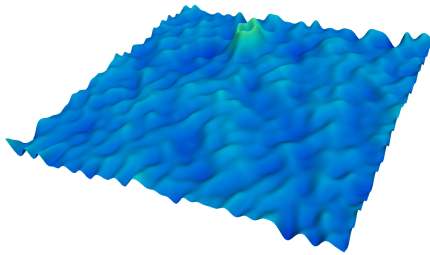
Figure 4.26: A snapshot of reconstruction of y-component of velocity and total energy per volume distribution from the reverse problem for time of maximum peak T_M and several other times. Loading by TYPE II - "force nodal loading", computational time $T = 100,000 \Delta t$ [A3].



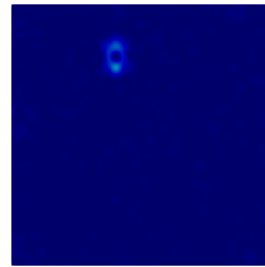
(i) : Y-component of velocity, time " $t = T_M + 10 \Delta t$ ".



(j) : Total energy per volume, time " $t = T_M + 10 \Delta t$ ".



(k) : Y-component of velocity, time " $t = T_M + 20 \Delta t$ ".



(l) : Total energy per volume, time " $t = T_M + 20 \Delta t$ ".

Figure 4.26: A snapshot of reconstruction of velocity-y and total energy distribution from the reverse problem for time of maximum peak T_M and several other times. Loading by TYPE II - "nodal force loading", computational time $T = 100,000 \Delta t$ [A3].

4.3.5 Reconstruction test and proposed methodology

This test is performed to analyze the effect of different types of boundary conditions on the accuracy of the reconstruction of the original source. The quality of the reconstruction is measured using the cost functions defined in Section 4.3.2. With these findings, it was possible to propose a flowchart for the implementation of the appropriate scheme with the application of TR boundary conditions for accurate reconstruction in TR tasks.

Numerical response to loading TYPE II in frontal task

First, the response to nodal force loading (TYPE II) in the frontal task was investigated to gain a better understanding of an optimal application of boundary conditions in the TR problem. The nodal force loading is applied to nodes in the region \mathcal{A} in the y-direction with the time function of the Ricker pulse. The kinematic quantities, namely the y-component of displacement, velocity and acceleration in the central node of \mathcal{A} are recorded, see Figure 4.27 [A3]. The result shows that the time history of the displacement in \mathcal{A} corresponds to the time function of the loading nodal force. This means that the time function of the nodal force loading must be an integral of the desired nodal velocity in order to force the desired motion in terms of velocity. The following numerical test shows the verification of this idea for a correct time reversal.

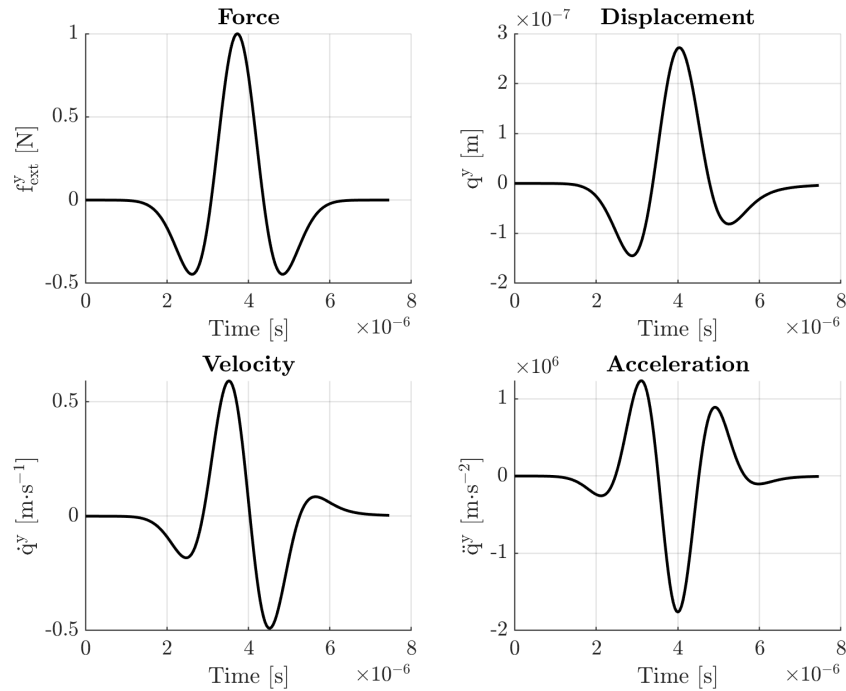


Figure 4.27: Output quantities in the y-direction at the middle point of loading by nodal force. The time function of nodal force (top-left) was applied as a load, other graphs represent the response of FE model. Only the quantities in the middle node out of nine nodes in total at point \mathcal{A} were recorded [A3].

Numerical verification of proposed procedure for loading TYPE II

Here, the effect of the application of the loading TYPE II in the full TR computation is examined. The nodes in the region \mathcal{A} are loaded by a nodal force with the time function of the Ricker pulse. Then, the normal velocity in the region \mathcal{B} is recorded from the frontal task. The obtained signal is reversed in time and applied as a force loading in the region \mathcal{B} . Finally, the velocity response from reverse task is recorded in the region \mathcal{A} . The Figure 4.28 (left) [A3] shows the time response in terms of velocity in the y-direction. The Figure 4.28 (right) [A3], shows the original pulse needed to be reconstructed (Loading pulse). The first and second time derivatives of the original pulse are also included here. Based on the comparison, it can be said that the time history of the recorded velocity (left) corresponds to the second time derivative of the original loading pulse (right).

This means, metaphorically, that during the numerical TR process (forward and reverse tasks together) two time derivatives of the original pulse are lost - each computation changes the time derivative of the output signal with respect to the input signal. This phenomenon can be explained by the impulse-momentum theorem (4.6), where there is a relation between the time history of the applied force and the derived velocity. For the correct reconstruction of the original pulse, one need to precede the time integration of the loading pulse both before frontal and reverse task of the TR process. In the following text, this phenomenon in TR computations is studied and the final form of the TR process in FEM is proposed.

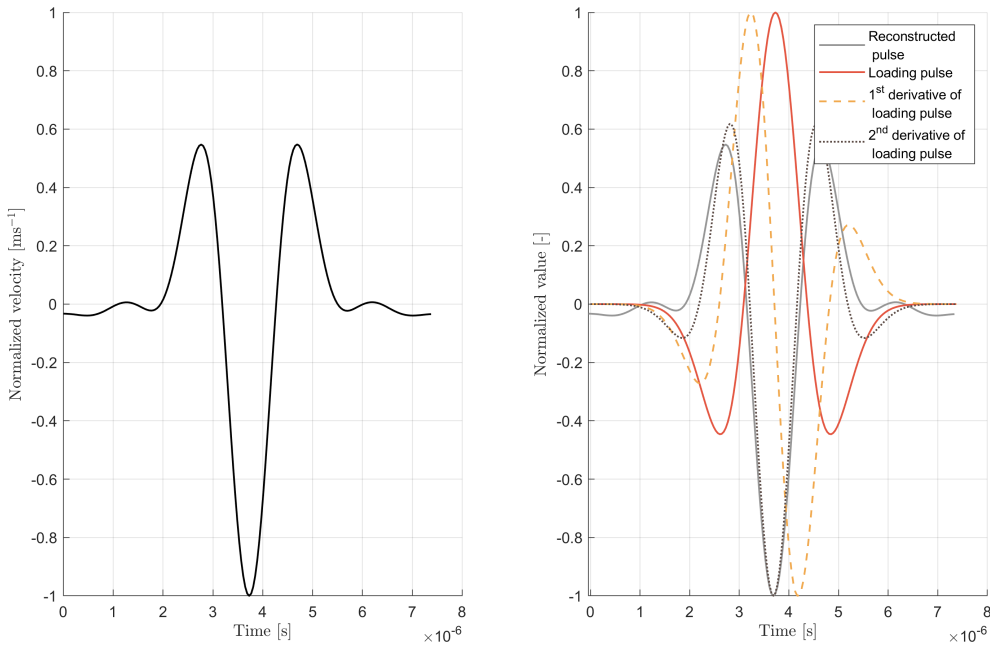


Figure 4.28: Reconstruction of the original source (left); original loading pulse with its time derivatives (right), original pulse (red solid line), its 1st time derivative (orange dashed line), and its 2nd time derivative (brown dotted line); reconstructed pulse (gray solid line) is also added here for clarity [A3].

Now, a sequence of time integration of the original loading pulse (the Ricker pulse) and time integration of a velocity signal recorded in the region \mathcal{A} is examined. The integrated Ricker pulse is shown in Figure 4.29 [A3]. Physically, it is a time history of the impulse of the external force with the time history given by (4.12).

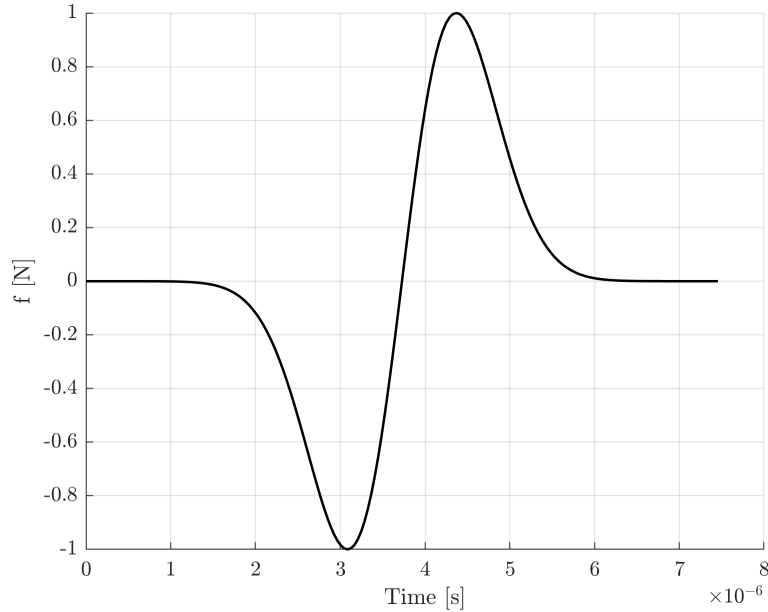


Figure 4.29: An integrated Ricker pulse as a time integral $\int_0^T R(t)dt$ [A3].

The computations are marked as **Int – Int**, **Int – Orig**, **Orig – Int**, and **Orig – Orig**, where the first key means the loading time function in the region \mathcal{A} for the forward task, and the second key means the loading time function in the region \mathcal{B} for the reverse task after reversing the responding signal in time. The key **Int** denotes the time integration of the pulse and **Orig** denotes the pulse without modification, i.e., without time integration. For example, the combination **Int – Orig** means, that the time function in the region \mathcal{A} is integrated in time and the time function recorded in the region \mathcal{B} is not integrated with respect to time and only reversed in time. Then it is applied as loading into the reverse task. For the numerical time integration of the signal, the trapezoidal rule is employed with the time step size as for the FE computation. Four combinations of keys occur (**Int – Int**, **Int – Orig**, **Orig – Int**, **Orig – Orig**) and this results in four reconstructed signals.

In general, the amplitudes of loading in the regions \mathcal{A} and \mathcal{B} must be chosen with respect to the accuracy of computation, the scale of the problem, and the material properties of the domain of interest.

The results normalized with respect to the maximum value are shown in Figure 4.30 (red/orange lines) [A3]. These plots summarize the time histories of the y-component of the reconstructed velocity in the region \mathcal{A} are summarized for all combinations of both integrated and non-integrated

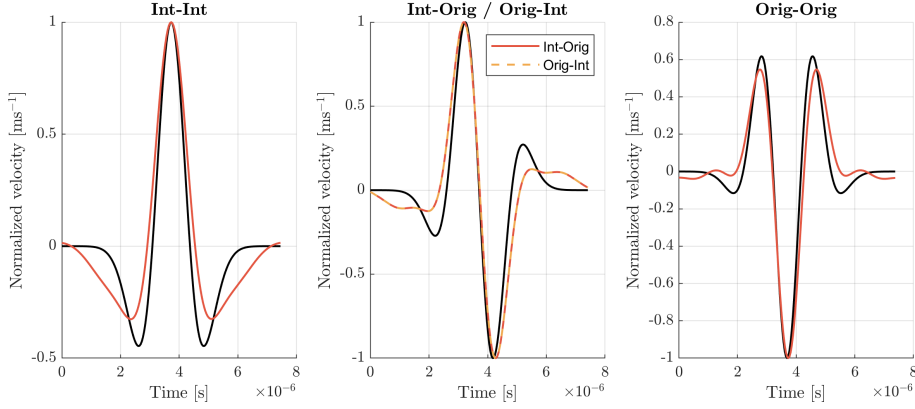
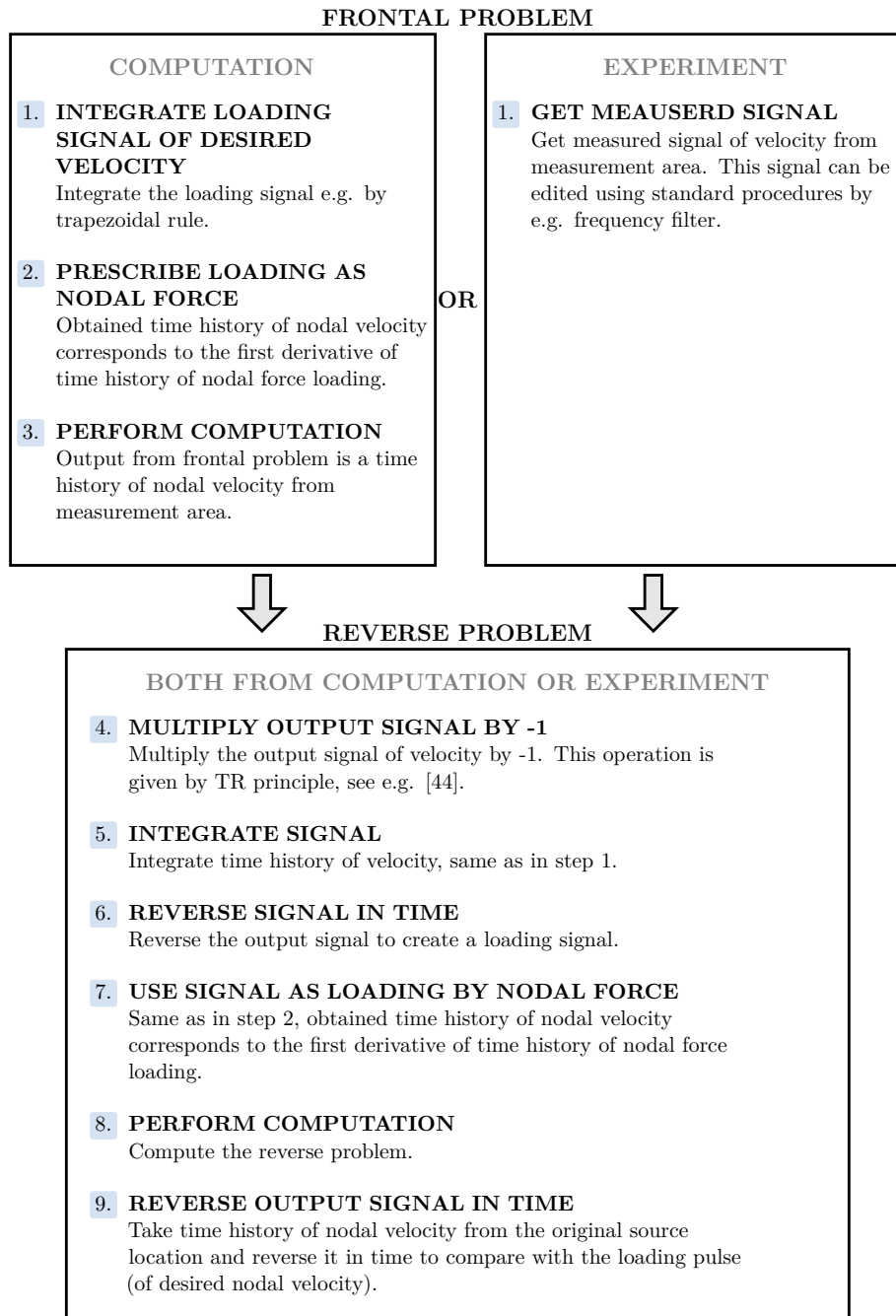


Figure 4.30: Reconstructions of the original source for four different combinations of modification of loading signals in frontal and reverse problems, denoted as **Int** and **Orig**. The first indication refers to frontal problem, the second one refers to reverse problem. The keys **Int** marks the time integration of the pulse and **Orig** marks the pulse without modification, i.e. without time integration [A3].

loading signals after the entire TR process. It is needed to say that with respect to the linearity of the problem, combinations **Int – Orig**, **Orig – Int** produce the same results. In all sub-figures the corresponding (analytically calculated) time derivative of the loading pulse is plotted as a black line.

In the left sub-figure, the black line corresponds to the Ricker pulse as an original loading pulse, in the middle sub-figure, the black line corresponds to the first time derivative, and finally, in the right sub-figure, the black line corresponds to the second time derivative. It is clear, that the combination **Int – Int** produces the correct time history of the original pulse of the nodal velocity. The combination **Int – Orig / Orig – Int** gives the first time derivative of the original pulse, and the combination **Orig – Orig** gives the second time derivative of the original pulse. The differences between the theoretical pulses and their time derivatives and the numerical results are given by spreading of the wave fronts in the reverse task where only partial information is used at the boundary of the domain of interest.

Based on the previous results, the variant **Int – Int** is preferred and this TR approach provides the correct reconstruction of the original source. Based on this knowledge of the behavior of the time change (time integration) of the pulse during the TR computations, the algorithm for computational TR is proposed, Alg. 2. This algorithm, if all steps are followed, leads to a "topologically" correct reconstruction of the original source. On the left side of the algorithm one can see the flowchart for the full computational approach for TR computations with the generation of the '*experimental data*' on the domain Ω_m numerically. On the right side one can see the flowchart for the application of TR with real experimental data in terms of measured velocities.



Algorithm 2: Proposed algorithm for practical use of time reversal method. On the left is the computational/computational approach, and on the right is the experimental/computational approach.

4.3.6 Key verification of the proposed methodology

In this series of numerical experiments, two types of loading for application in TR tasks are compared – TYPE I (nodal velocity) and TYPE II (nodal force). The effect of the size of the domain Ω_m on the quality of the reconstruction is also examined in a form of different numbers of active nodes in reverse task, to which the nodal information is prescribed. Five different numbers of loaded nodes are assumed – one node, five nodes and eleven nodes with separate signals, and the same numbers with averaged signals, see Figure 4.31 [A3].

Moreover, ten different computational times are assumed, defined by the number of time steps, indicated as T_1, \dots, T_{10} , see Table 4.3 for the details. T_i denotes the time of computation for both the frontal and reverse task. The time T_i can also be viewed as the number of reflections of the longitudinal wave in the domain of interest, for example, the time T_3 corresponds to approximately 10 reflections of the longitudinal wave with wave speed c_L between the opposite edges.

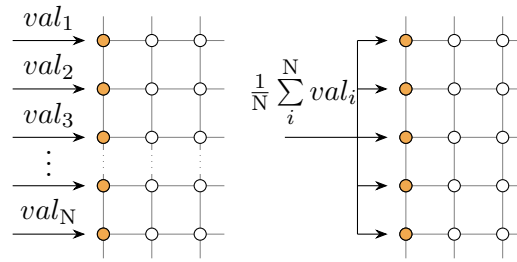


Figure 4.31: Scheme of the different ways to prescribe the loading values val . N nodes loaded (left), N nodes loaded - averaged (right) [A3].

Indication of task	Number of time steps	Computational time [s]	Number of reflections
T_1	1,000	0.00004009	2.12
T_2	2,000	0.00008018	4.24
T_3	5,000	0.00020045	10.61
T_4	10,000	0.00040090	21.21
T_5	20,000	0.00080180	42.43
T_6	30,000	0.00120270	63.64
T_7	40,000	0.00160360	84.85
T_8	50,000	0.00200450	106.06
T_9	75,000	0.00300675	159.10
T_{10}	100,000	0.00400900	212.13

Table 4.3: Table of computational times T_i .

Figures 4.32 and 4.33 [A3] show the values of the global cost C_G from Section 4.3.2 for all tasks with different times of computation T_i and different numbers of active nodes, with or without averaging, in the reverse task.

Figure 4.32 [A3] shows the results for loading TYPE I and Figure 4.33 shows the results for loading TYPE II. Different numbers of loaded nodes and different lengths of computational times show how the quality of the reconstruction changes. Two different types of loading, by nodal velocity and by nodal force, compare two approaches how to solve the problem with standard methods in commercial FE software.

For loading TYPE I, Figure 4.32 [A3], it can be seen that the averaging of information leads to a loss of accuracy of the reconstruction. There is also an influence of the number of active nodes on the quality of the reconstruction. From the physical point of view, when the prescribed signal is applied as the nodal velocity, the boundary is moved in a rigid way and this boundary reflects the propagating waves as rigid boundary, which has opposite an effect on the reflection of stresses than the stress-free boundary conditions, see e.g. the book of Achenbach on wave propagation in solids, [90]. Therefore, the TYPE II leads to more stable results of the reconstruction, see Figure 4.33 [A3]. With larger number of active nodes for the application of boundary conditions, this effect is even amplified. The time referred to T_3 is sufficient for the reconstruction. Based on this numerical study, the TYPE II is preferred in the TR process and as an advantage, there is no need to modify the finite element code and only a preceding time integration of the reversed data is needed as part of the flowchart.

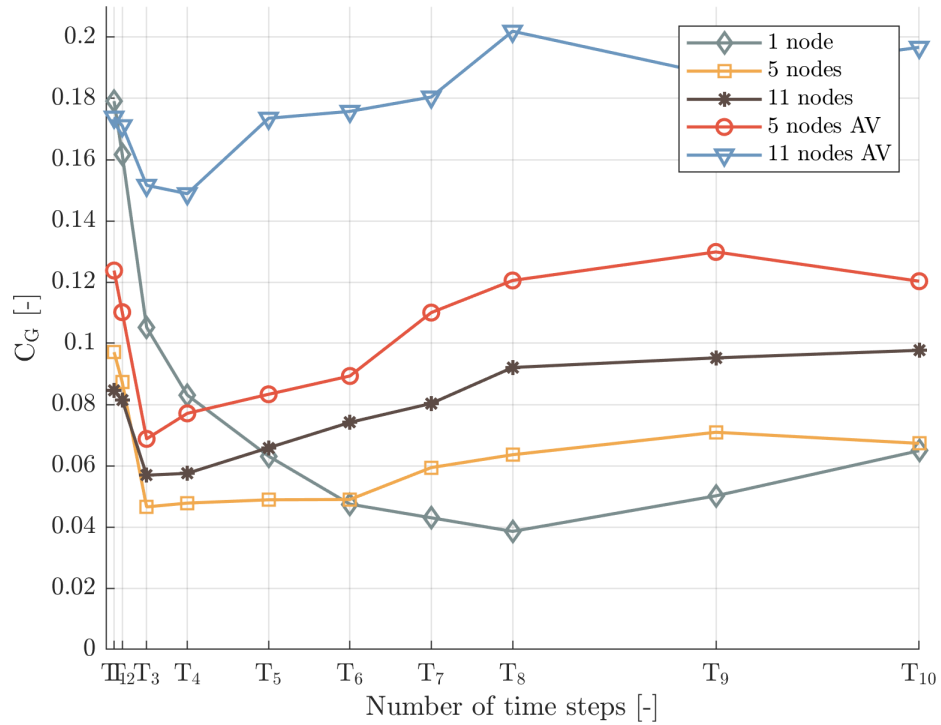


Figure 4.32: Global cost C_G , TYPE I - loading by nodal velocities [A3].

For local consideration at the localized point \mathcal{A} , the time histories of the normalized velocity after TR computation of the both types of loading are

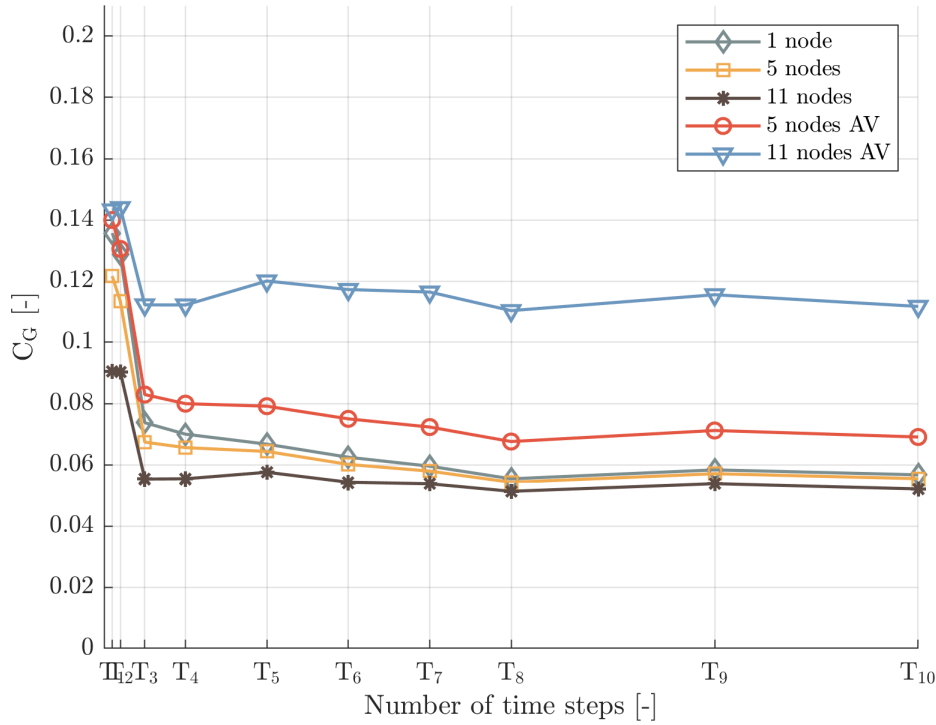


Figure 4.33: Global cost C_G , TYPE II - loading by nodal forces [A3].

shown in Figure 4.34 [A3] (loading by nodal velocity) and Figure 4.35 [A3] (loading by nodal force). The computations were performed for time T_{10} and for all numbers of active nodes, as mentioned in the previous text. Each reconstructed signal is normalized so that the maximum value is equal to 1, again assuming a linear system that can be scaled arbitrarily. Then the signals are reversed in time, although this is not necessary due to the symmetry of the loading signal. This normalization of the signals allows at least some qualitative comparison of the reconstruction.

For the loading TYPE I, one can see a different arrival time of the maximum peak, depending on the number of active nodes in the reverse task and averaging of the reversed quantities. On the contrary, the results for the loading TYPE II show a stable character and deviation of the signal is relatively small. This means that the loading TYPE II is preferred for a correct reconstruction of the original signal.

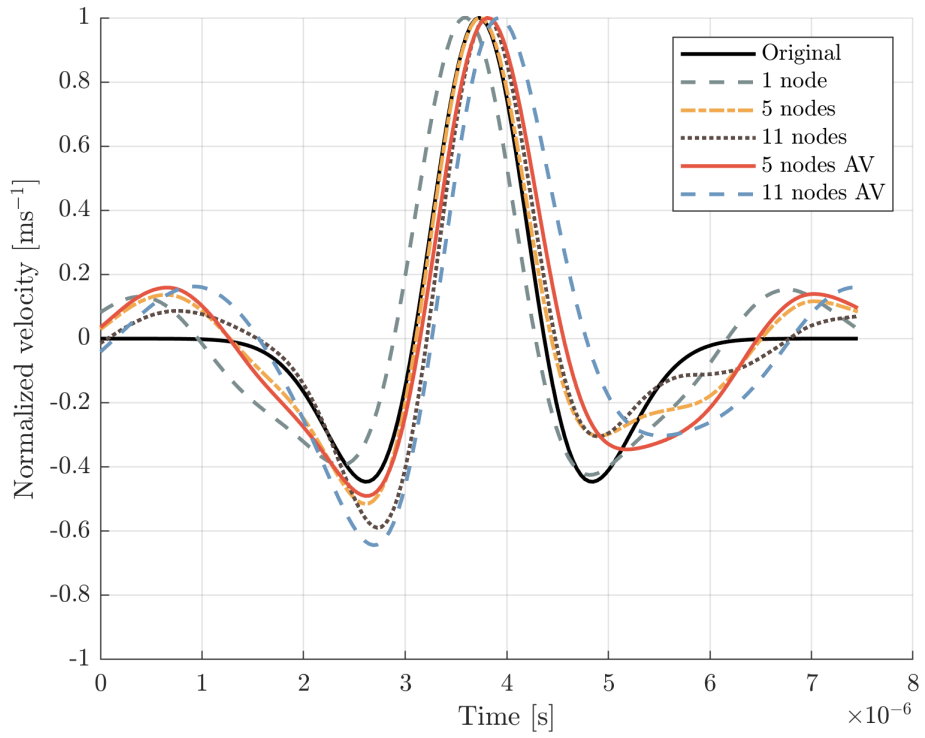


Figure 4.34: Reconstructed pulse for time T_{10} , loading of TYPE I - nodal velocities [A3].

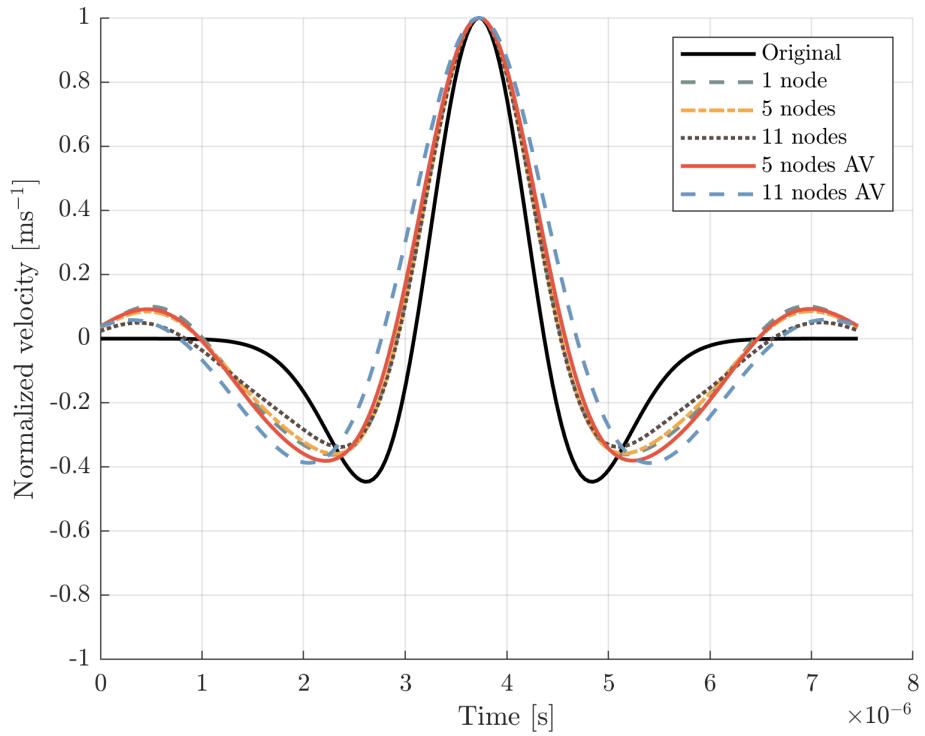


Figure 4.35: Reconstructed pulse for time T_{10} , loading of TYPE II - nodal forces [A3].

4.3.7 Numerical sensitivity study of the proposed methodology

Five additional studies of numerical sensitivity are performed using the presented algorithm (Alg. 2). The effects studied on the reconstruction of the original pulse are the time step size, the mesh size, the number of transmitters, the domain shape (domain with a hole), and the environmental disturbance (background noise). In each study, one parameter is changed in the reverse task and compared with the reference one. Again, the same FE model is used, as shown in Figure 2.2 [A3] and Ricker pulse for loading. Eventual changes are commented on in the description of each sensitivity study. The computational time for all studies was $T_4 \sim 10,000 \Delta t$. The quality of the reconstruction is evaluated here only visually, since not enough numerical experiments are performed to use the costs to show a reasonable trend. The following results are more illustrative and show some practical aspects of computational TR.

Sensitivity study 1 - time step size

In Sensitivity study 1, the time step size is changed in the reverse problem - three different Courant numbers (time step sizes) are used. One task is a reference task with the same time step size as in the frontal task, and then one is smaller and the other one is larger than in the reference task. See Table 4.4 for the details.

Courant number	Time step size [s]
0.5	$2.673 \cdot 10^{-8}$
(reference) 0.75	$4.009 \cdot 10^{-8}$
0.99	$5.282 \cdot 10^{-8}$

Table 4.4: Sensitivity study 1 - input values [A3].

It can be seen that changing the size of the time steps has a small impact on the quality of the reconstruction, see Figure 4.36 [A3]. Only a small time and phase shift is apparent, resulting from the temporal-spatial dispersive behavior of the finite element method as a function of the time step size, [76].

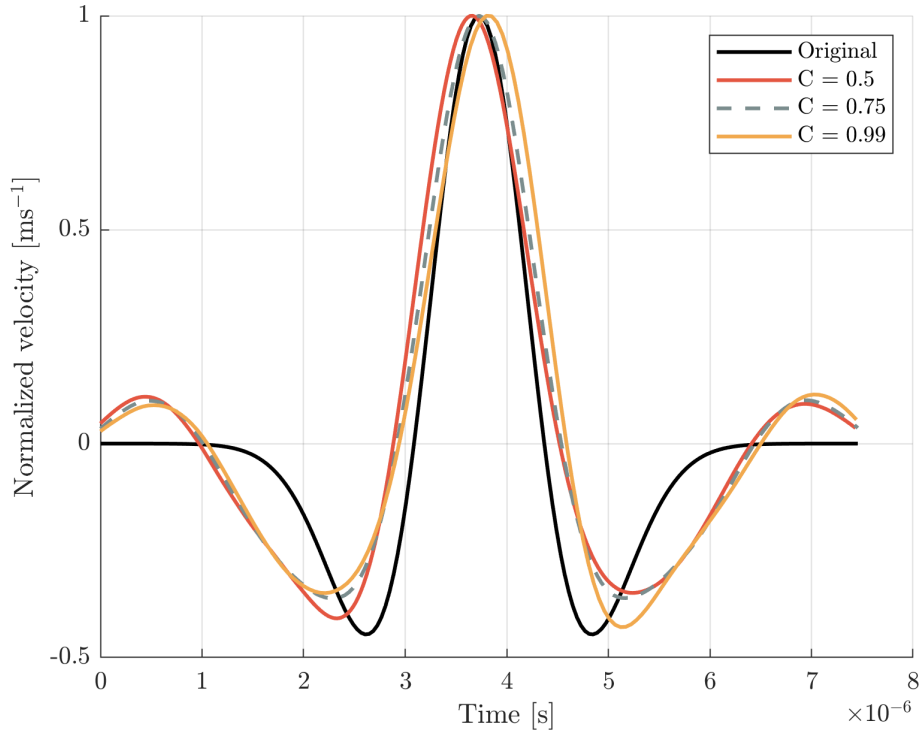


Figure 4.36: Sensitivity study 1 - Reconstruction [A3].

Sensitivity study 2 - mesh density

In Sensitivity study 2, the FE mesh density is changed in the reverse problem. Three different meshes are used in the reverse problem, the Courant number $Co \doteq 0.75$ in all cases, so the time step size had to be changed. Again, one reverse task is reference with the same mesh as in the frontal task, then one mesh is coarser and the other one is finer. See Table 4.5 for the details.

Element size [mm]	Mesh density	Time step size [s]
0.3125 mm	$320 \times 320 = 102,400$	$3.132 \cdot 10^{-8}$
(reference) 0.4 mm	$250 \times 250 = 62,500$	$4.009 \cdot 10^{-8}$
0.5 mm	$200 \times 200 = 40,000$	$5.011 \cdot 10^{-8}$

Table 4.5: Sensitivity study 2 - input values.

Very significant impact on the result has the change of FE mesh density, see Figure 4.37 [A3]. Here the time and phase shift is more apparent than in Sensitivity study 1, though the reconstructed peak is still easily recognizable from the surrounding signal. This can be explained by the fact that the FE model has a dispersive behavior - the numerical wave speed depends on the mesh density, see [88], and by change of mesh density this effect is more dominant than the effect of changing the time step size.

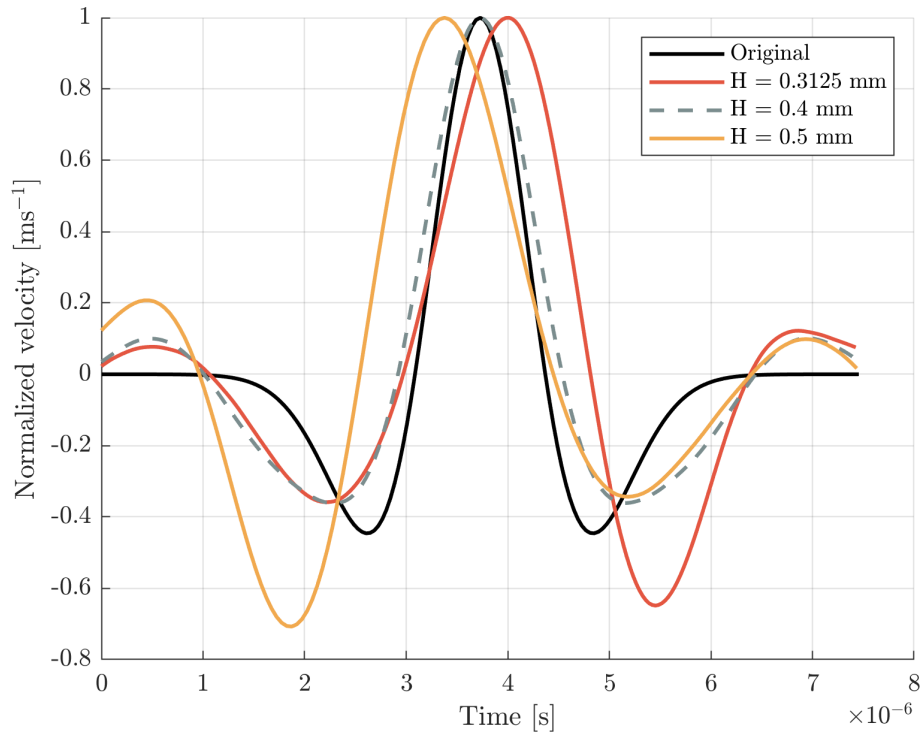


Figure 4.37: Sensitivity study 2 - Reconstruction [A3].

Sensitivity study 3 - number of transmitters

In Sensitivity study 3, the quality of the reconstruction is studied depending on the number of positions used to record the output signals in the frontal problem. The reverse problem is then loaded at these positions. The positions are denoted as $\mathcal{B}_1 - \mathcal{B}_3$, and the coordinates are shown in Figure 4.38 [A3]. The positions were chosen randomly. In these three tasks, one (\mathcal{B}_1), two ($\mathcal{B}_1, \mathcal{B}_2$), and three ($\mathcal{B}_1, \mathcal{B}_2, \mathcal{B}_3$) positions of transmitters are used stepwise.

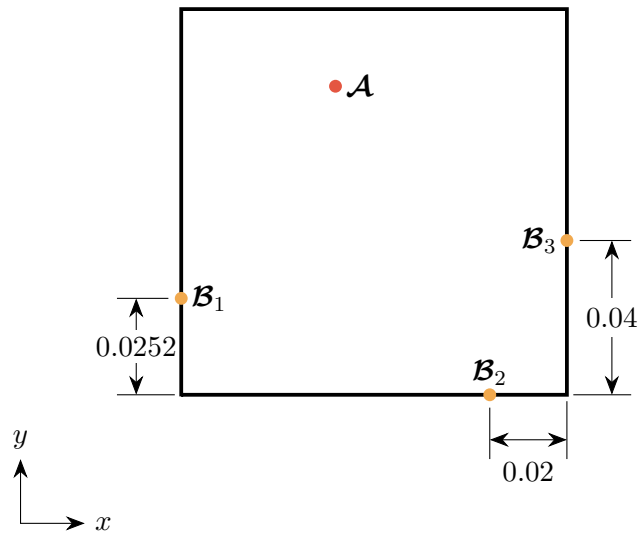


Figure 4.38: Sensitivity study 3 - positions of recording points [A3].

Based on Figure 4.39 [A3], the number of points \mathcal{B}_i does not cause any time shift. Using more points (transmitters) for loading slightly improves the quality of the reconstruction.

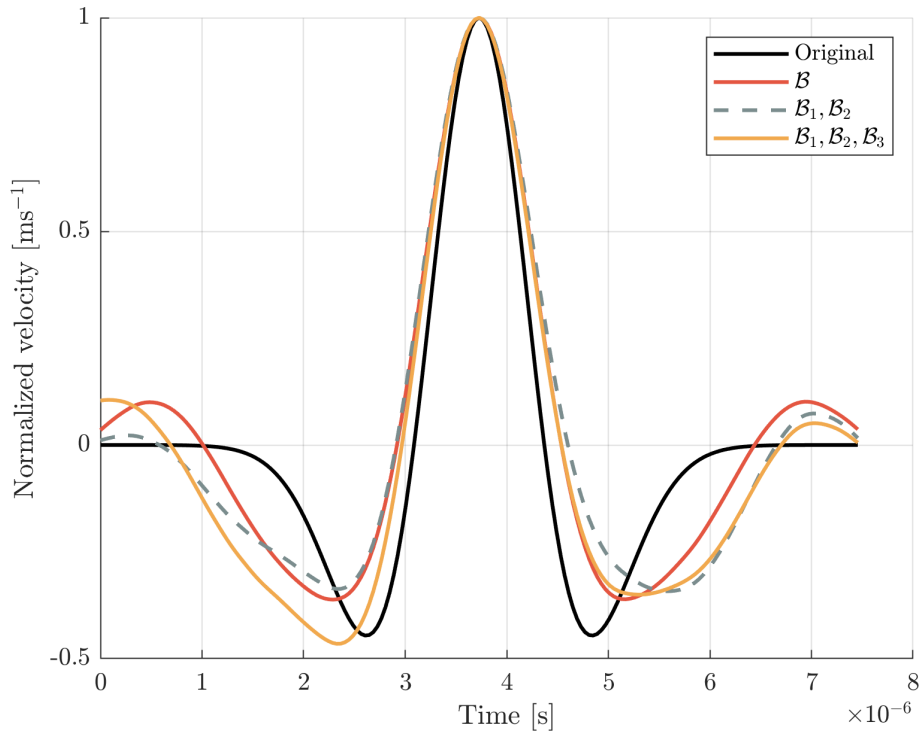


Figure 4.39: Sensitivity study 3 - Reconstruction [A3].

Sensitivity study 4 - domain with hole

The Sensitivity study 4 represents a problem in which the analysed domain contains an unknown obstacle. The dimensions are shown in Figure 4.40 [A3]. Two frontal tasks were performed, where in one of them the domain contains a rectangular hole. Then two reverse tasks were performed, both on the domain without the hole, simulating that the obstacle is not known.

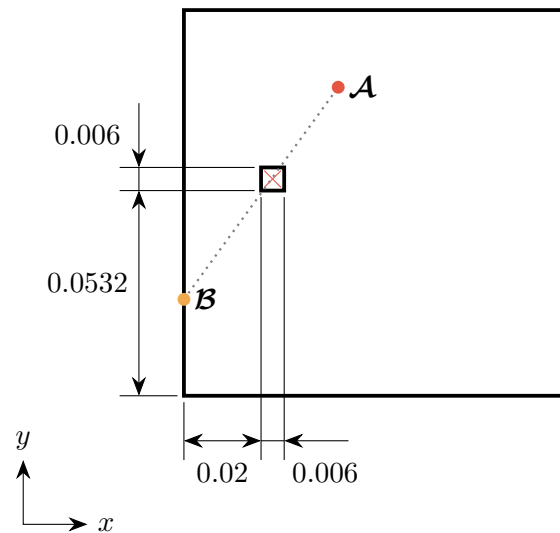
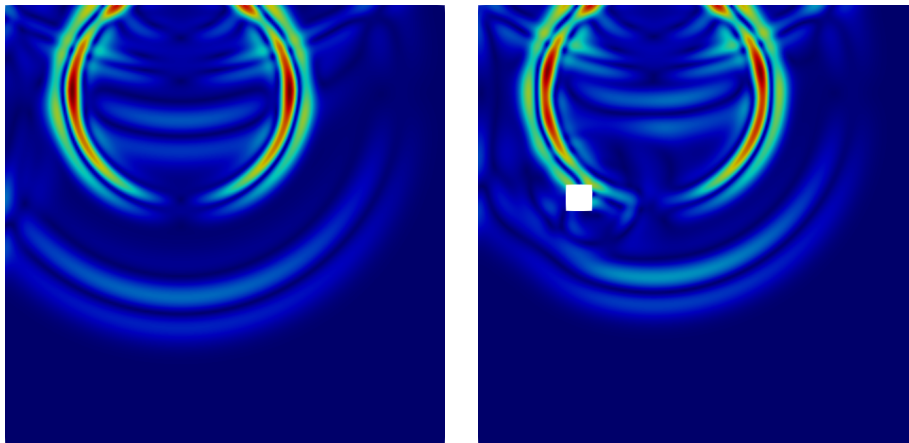


Figure 4.40: Sensitivity study 4 - scheme [A3].



(a) : A domain without a hole.

(b) : A domain with a rectangular hole.

Figure 4.41: A snapshot of velocity wave field from the frontal problem for time $300 \Delta t$, comparison of a domain without/with a hole [A3].

For the successful reconstruction, the wave reflections and time of computation play the key role, as the principal of the TR method states. The present obstacle, in this case a small rectangular hole, behaves like a scatterer and brings further reflections into the domain. This study shows the robustness

of the TR method and the approach used, as there is only a small difference between the reconstructed signals from the pure domain and the domain with a hole, see Figure 4.42 [A3].

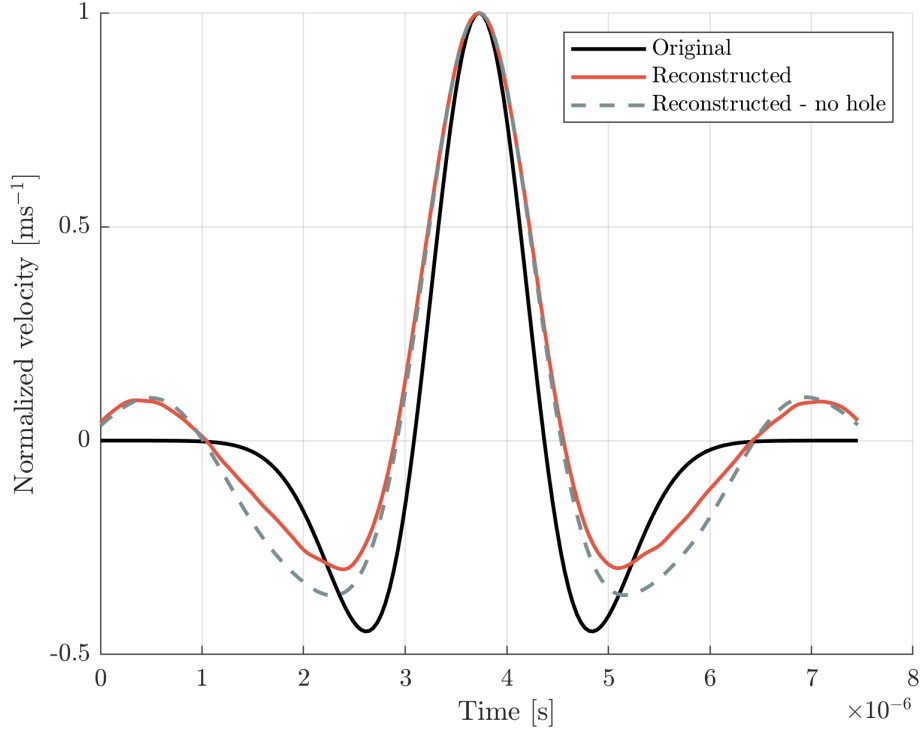
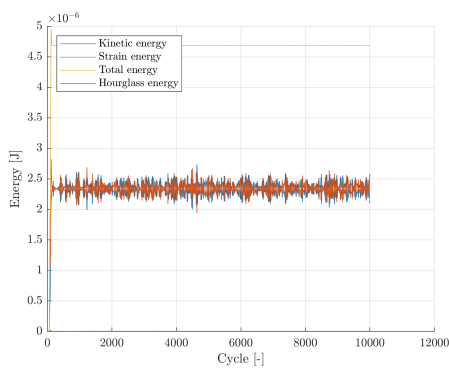


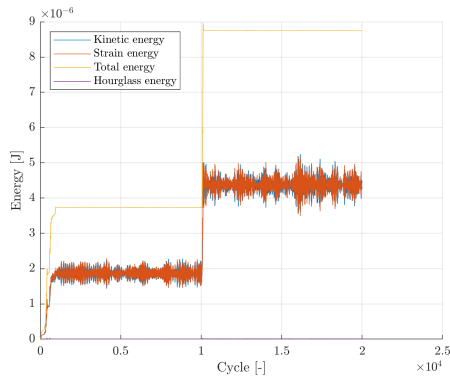
Figure 4.42: Sensitivity study 4 - Reconstruction [A3].

Sensitivity study 5 - background noise

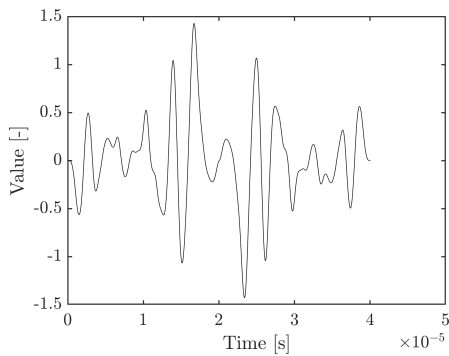
In Sensitivity study 5, the influence of a preceding disturbance of the system is examined. This is represented by a pseudo random signal, see Figure 4.43c [A3], which generates a complex wavefield before the Ricker pulse is transmitted. The disturbance signal is a filtered white noise that covers the frequency range of the Ricker pulse and has a zero mean value. This study is designed to test the superposition principle and the robustness of TR method to environmental disturbances. The computational time is doubled here ($20,000 \Delta t$). At time $t = 0 \Delta t$ the pseudo-random signal is prescribed as a load at arbitrarily chosen location \mathcal{D} , marked in magenta in Figure 4.43d. When the classical loading by the Ricker pulse begins at $t = 10,000 \Delta t$, a noise-like wavefield is already present in the system, see Figure 4.43d. Then only the second half of the output signal is considered as relevant and sent back as a load in the reverse problem. Compare the energy conservation in Figures 4.43a and 4.43b for tasks without and with disturbance to see the impact on the total energy. Note that if the task ran until $20,000 \Delta t$, we would also see a reconstruction of the disturbance.



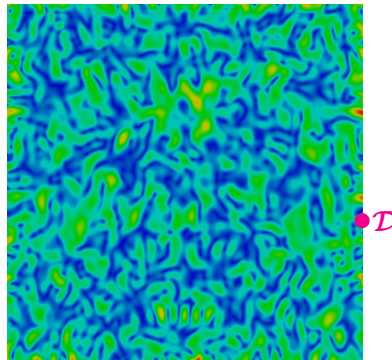
(a) : Energy conservation of frontal task without noise.



(b) : Energy conservation of frontal task with noise applied.



(c) : Pseudo random signal prescribed as a noise.



(d) : Velocity magnitude distribution at time $10,000\Delta t$ - fully developed "noise".

Figure 4.43: Sensitivity study 5 - creation of noise [A3].

Result shows, see Figure 4.44 [A3], that background noise does not have a large impact on the quality of the reconstruction, which is a well known fact in experimental TR.

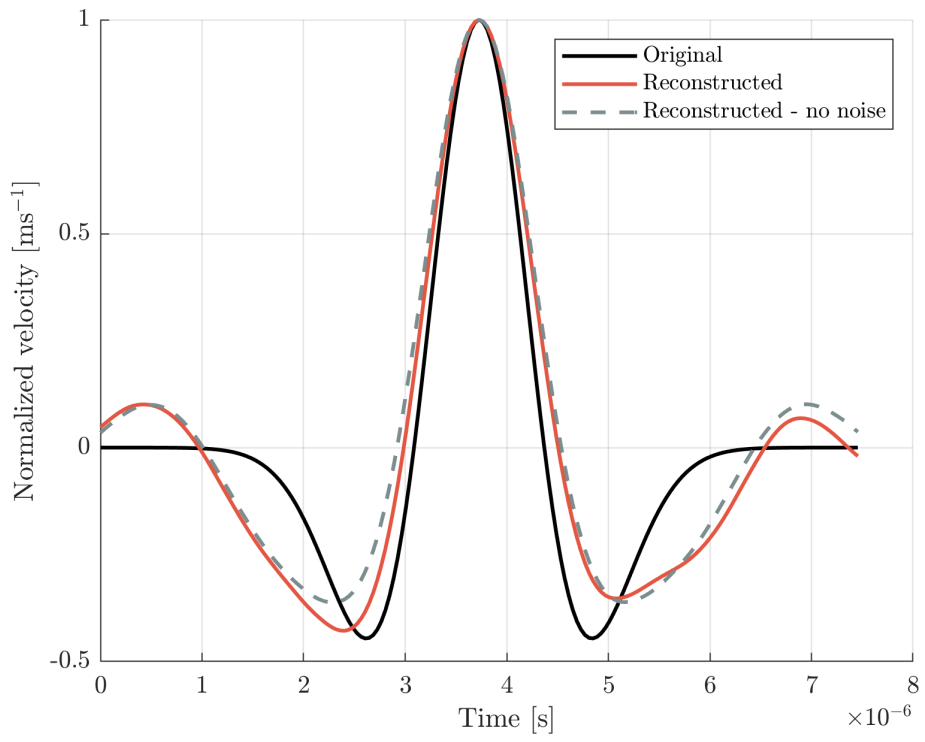


Figure 4.44: Sensitivity study 5 - Reconstruction [A3].

4.4 TR with experimental data

This section presents the not yet published results of using real experimental data to reconstruct the original source in the time domain using the proposed methodology. The paper is in preparation.

In this section, the experimental data from the paper [A1] were used for reconstruction of the original source, see Section 4.2.1. In the mentioned paper, we worked only with three measured signals at points A, B, and C, but in fact 195 signals were recorded. These responding signals were used for the reconstruction of the original loading signal. In accordance with the proposed procedure, see Algorithm 2, the recorded signals of normal velocity were time-reversed and integrated and used as a pressure load in the reverse task.

4.4.1 Problem definition

A thin aluminum plate was loaded by a piezoelectric transducer at the center of the bottom edge. The dimensions of the plate were $399 \times 50 \times 1.35$ mm and the material properties were $E = 72$ GPa, $\nu = 0.333$, $\rho = 2770$ kg·m⁻³. The FE mesh consisted of $1596 \times 200 = 319200$ 4-noded quadrilateral elements, the length of the element edge was 0.25 mm, Δt was $4.5 \cdot 10^{-8}$ s. The response in terms of normal velocity was recorded at the top edge in 195 points with a spatial step of 1 mm, symmetrically distributed with respect to the central point, which was exactly opposite to the transducer. See the scheme in Figure 4.45.

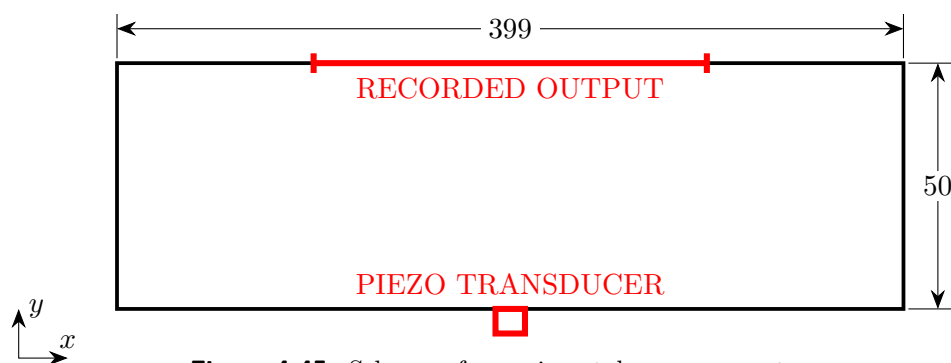


Figure 4.45: Scheme of experimental measurement.

The loading corresponded to a smooth pulse of duration t_0 with amplitude σ_0 changing according to a cosine train 333 kHz with 0.25 cosine window, sampled at 20 MHz. The shape of the loading is given in Figure 4.46. The response was recorded one after another in all 195 points with the vibrometer. For a more detailed description of the experimental setup, see Section ???. See the x-t plot of the recorded normal velocity for the first 1000 time steps in Figure 4.47.

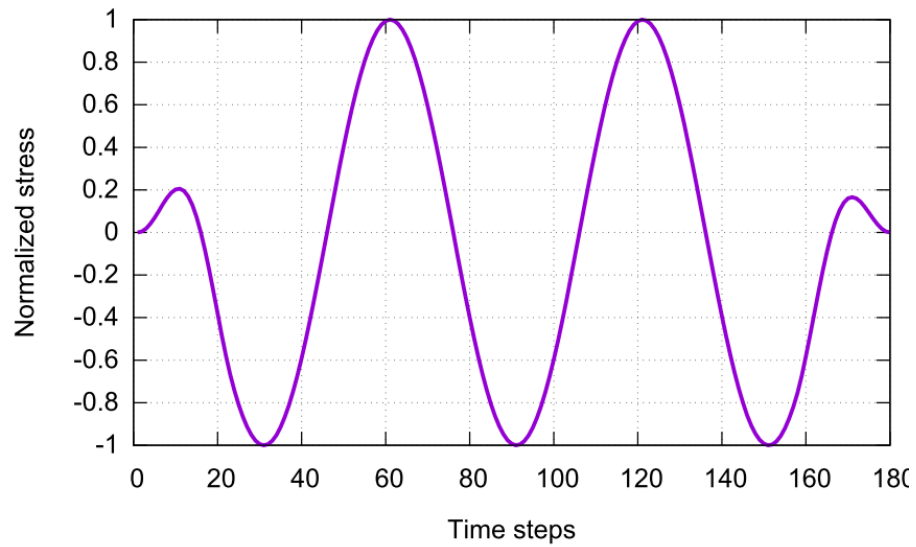


Figure 4.46: Loading signal.

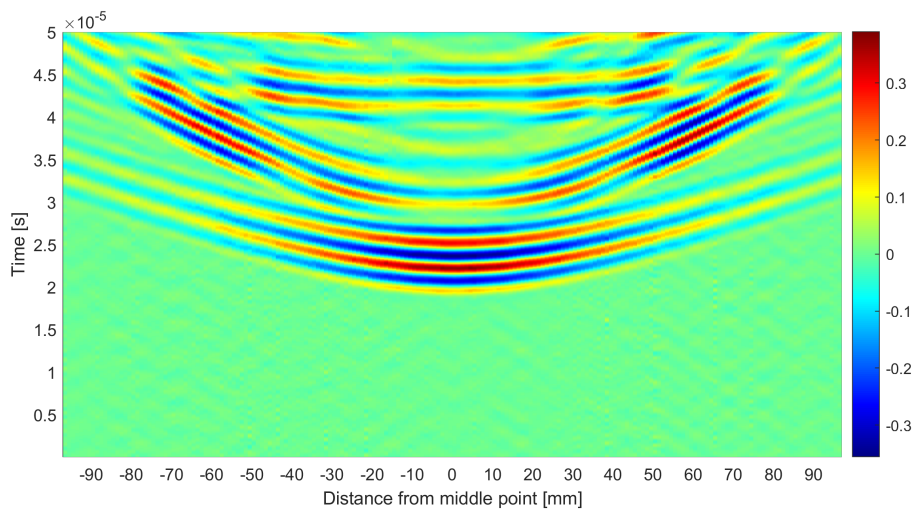


Figure 4.47: X-t plot of measured normal velocities.

4.4.2 Results of TR with experimental data

Unlike purely numerical experiments, such as in Section 4.3, where the time history of the velocity in the loaded area is known and the reconstruction can be directly compared and assessed using, e.g., the proposed cost functions, in a real experiment the velocity excited by the transducer cannot be recorded, so the reference signal does not exist. Therefore, the real velocity pulse recorded at the center of the transducer was used as the reference signal for comparison with the reconstruction, see Figure 4.13. Because of the uncertainties with exact start of the loading and with the exact shape of the loading signal, it was not straightforward how to assess the quality of the reconstruction, and the result is assessed only visually.

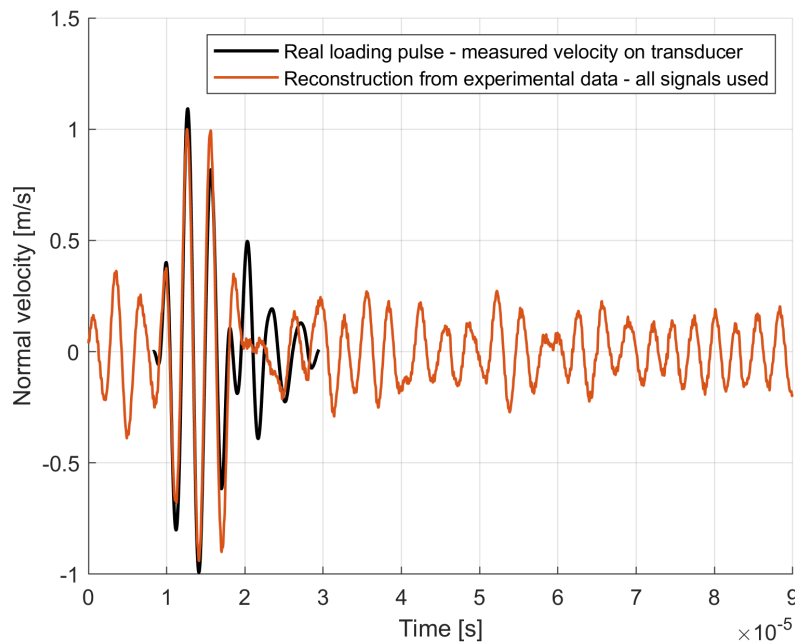


Figure 4.48: Result of TR.

4.4.3 Study of sensitivity to position of reverse load

In this study only few recorded signals were used for load in reverse task - 5 tasks each with different group of signals from 3 neighboring nodes. See the positions of loaded nodes in Figure 4.50.

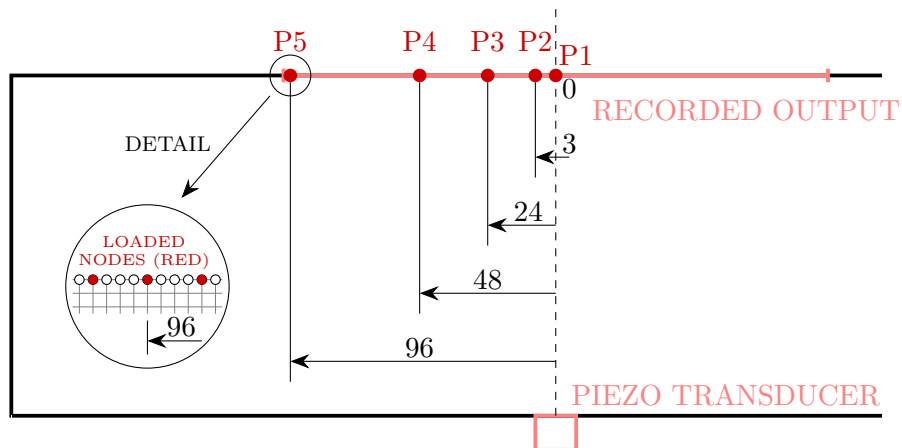


Figure 4.49: Scheme shows positions (P1,...,P5) of loaded group of nodes and their distance from the axis of symmetry.

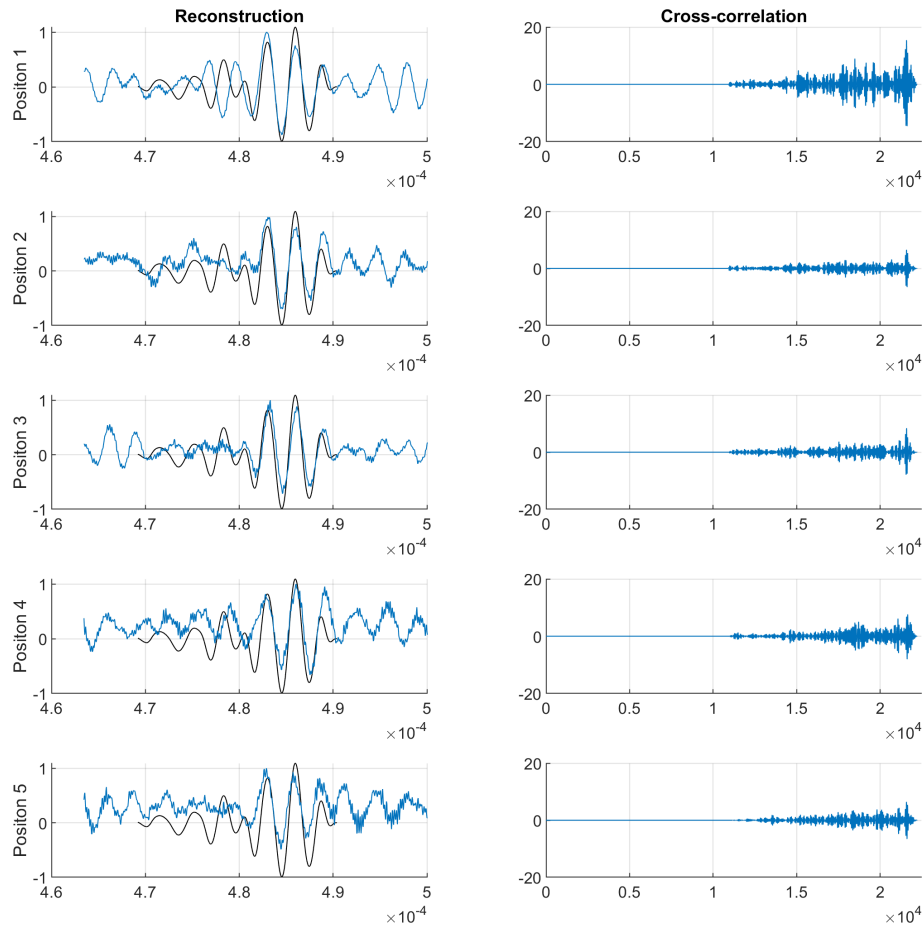


Figure 4.50: Result of sensitivity study to position of reverse load. Reconstruction of the loading signal is in the left column in blue, black line is the real loading pulse. In the right column is the cross-correlation of the reconstructed and the original signal.

4.4.4 Discussion of TR with experimental data

The reconstructed signal in Figure 4.48 was "positioned" to match the reference signal by shifting it in both the x and y directions. The criterion for the y-shift was purely visual and the criterion for the x-shift (time) was the value of the cross-correlation of both signals. The magnitude of the reconstructed signal was also arbitrarily updated. The positioning of the reconstructed signal is possible due to the linearity of the problem. The same post-processing of the reconstruction will be necessary in any kind of real employment of TR for the lack of knowledge of the source signal.

The results prove that the proposed methodology works well and provides a correct reconstruction of the source in the time domain. Although there are differences between reconstruction done from different positions, Figure 4.50, the original source is recognizable in all cases. Intuitively, the best result is obtained for the shortest transmitter-receiver distance, when the most reflections are captured.

4.5 Other numerical examples

Independently of the already presented and subsequent studies, the digital twin principle or application of TR method were also tested and presented at conferences [A11, A12, A13, A14].

4.5.1 Influence of temperature

Presented at conferences [A15], and [A16].

Problem definition

In this task, we model a situation when temperature changes by several degrees of Celsius in between the frontal and the reverse problems. Even though the change in shape can be neglected, the change in elastic parameters plays an important role, see e.g. [91], and this small temperature variation has to be taken into account in real applications of TR, because the local wave speed changes. We simulate the change of temperature by modifying Young's modulus E to make our study dependent only on one parameter. According to [92], the temperature dependence of Young's modulus is described by the formula (4.13) for a temperature range of 20 - 600 °C, where the subscript of E means the value of temperature. The change of E reflects in the change of the velocity of the longitudinal wave c_L . Table 4.6 shows the values of c_L and E for particular tasks.

$$E_T = \left[1 + \frac{T}{2000 \ln\left(\frac{T}{1100}\right)} \right] E_{20} \quad (4.13)$$

Number of task	Decrease of c_L in %	c_L [ms ⁻¹]	E [Pa]
Reverse task 0	0.00	5 291.265	$2.0000 \cdot 10^{11}$
Reverse task 1	0.01	5 290.735	$1.9996 \cdot 10^{11}$
Reverse task 2	0.05	5 288.619	$1.9980 \cdot 10^{11}$
Reverse task 3	0.10	5 285.973	$1.9960 \cdot 10^{11}$
Reverse task 4	0.20	5 280.682	$1.9920 \cdot 10^{11}$
Reverse task 5	0.50	5 264.808	$1.9801 \cdot 10^{11}$

Table 4.6: Change of longitudinal wave speed c_L and Young's modulus E in case study.

We consider a two-dimensional domain under a plane stress condition with stress-free boundary conditions. The dimensions of the domain of

interest are depicted in Figure 4.51. The element size was 0.4 mm, giving $250 \times 250 = 62\,500$ elements. Material properties were $E = 2 \cdot 10^{11}$ Pa for the reference task, $\rho = 7\,850 \text{ kg} \cdot \text{m}^{-3}$, and $\nu = 0.3$. Time of computation was $2 \cdot 10^{-3}$ s, and the time step size was $3.7 \cdot 10^{-8}$ s ($Co \doteq 0.69$). In the frontal task, the position \mathcal{A} shows the location of the loading signal and the position \mathcal{B} shows the location of recording of the response. In the reverse task, these points are swapped. For loading, the same Ricker pulse was used as in Figure 4.23 given by equation 4.12.

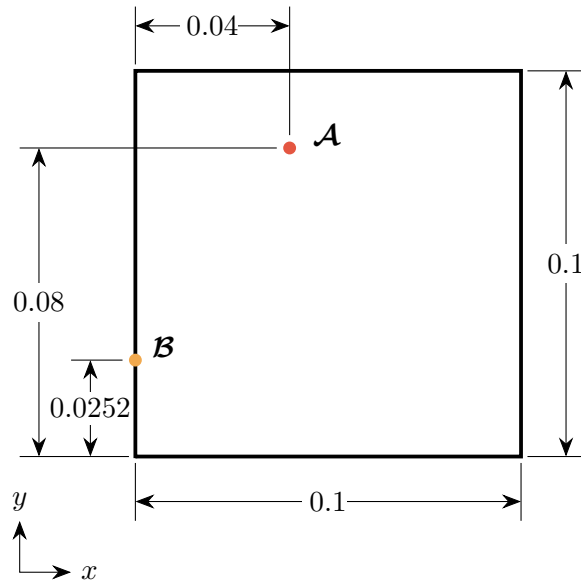


Figure 4.51: Scheme for analysis of influence of temperature.

Results and discussion

The change in temperature, and thus the change in wave speed, is reflected in the reconstructed pulse - it is shifted in time and overall deformed. See the reconstructed pulses for the considered values of the decrease in the wave speed, Figure 4.52. In principle, the same result is obtained for wave speed increased by the same amount, Figure 4.53. In this case, the resulting pulse is shifted and deformed in the opposite way, due to the linearity of the problem.

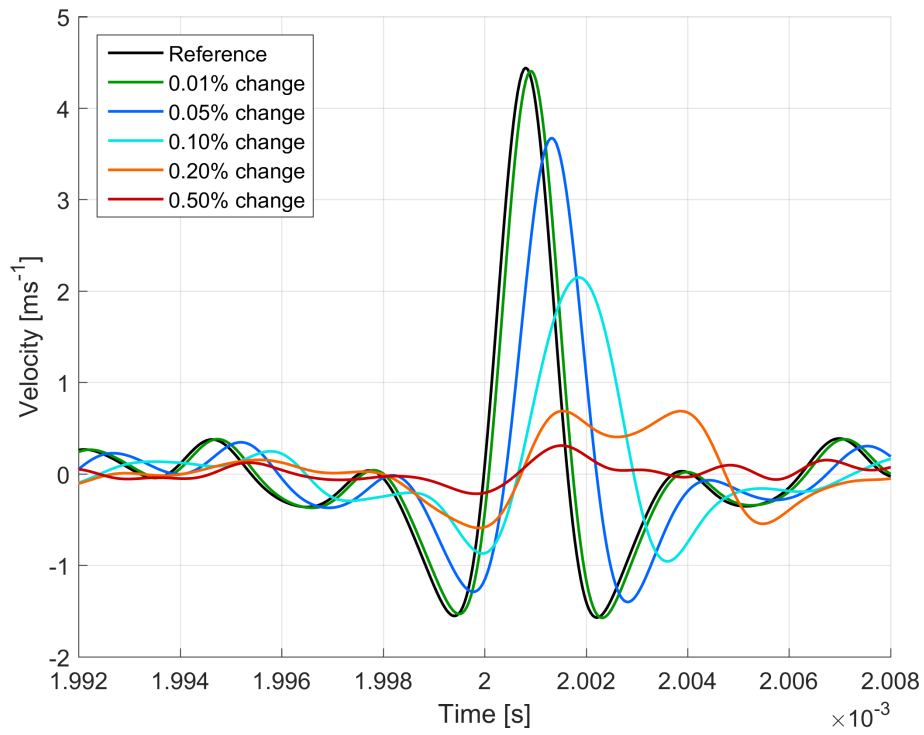


Figure 4.52: Reconstructed pulse - decreased wave speed c_L (increased temperature).

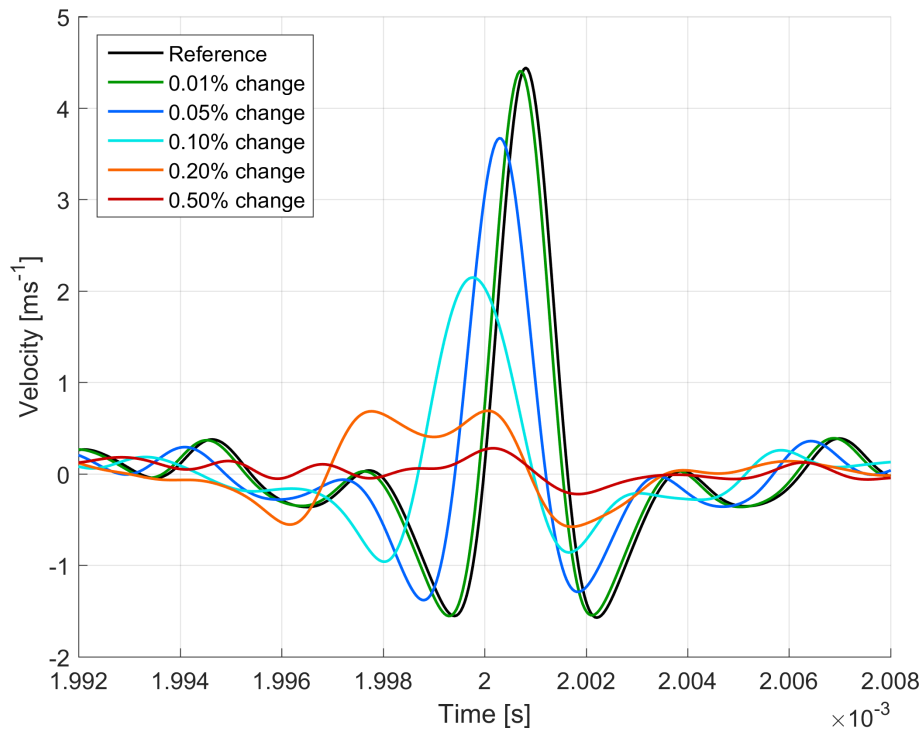


Figure 4.53: Reconstructed pulse - increased wave speed c_L (decreased temperature).

4.5.2 Cross-correlation

Presented at conference [A12].

Problem definition

In this simulation, a thin 3D aluminum strip, see scheme in Figure 4.54, was loaded by a pseudo-random signal of normal velocity, Figure 4.55a, at the point marked with a red cross in the scheme. The FE model consists of 192,000 8-noded hexagonal elements. The material parameters were $E = 69 \cdot 10^9$ Pa, $\nu = 0.334$, and $\rho = 2700 \text{ kgm}^{-3}$. The time of computation was $T = 0.001$ s, with $\Delta t = 3 \cdot 10^{-8}$ s. There were 37 nodes loaded with the same signal representing a round transducer, see Figure 4.55b. In the frontal task, normal velocity was recorded at two points (always in one node) marked with a blue and a green cross. In two reverse tasks, one-by-one the reversed signals were used here as loading and the normal velocity was recorded again in nodes at the highlighted grid, see Figure 4.55c.

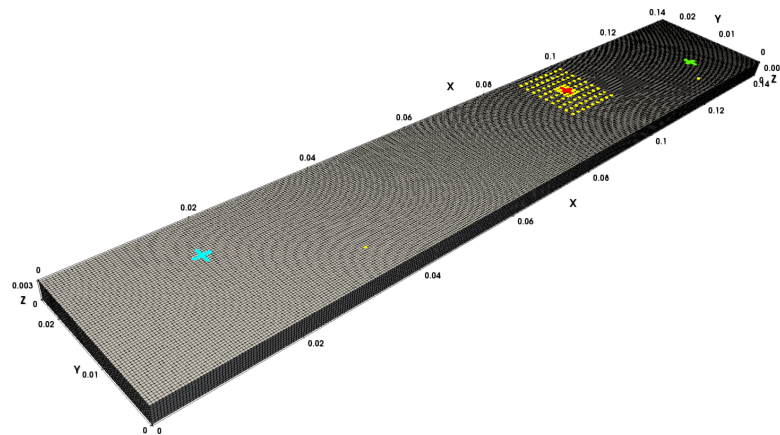


Figure 4.54: Scheme of the numerical experiment - localization of source using cross-correlation.

Results and discussion

The signals from both reverse tasks were correlated, clearly marking the position of the original source, see results in Figure 4.56. The red signals come from nodes originally loaded in the frontal task. It is clear that this method is very sensitive - only loaded nodes show some visible correlation and for directly adjacent nodes, no correlation is apparent.

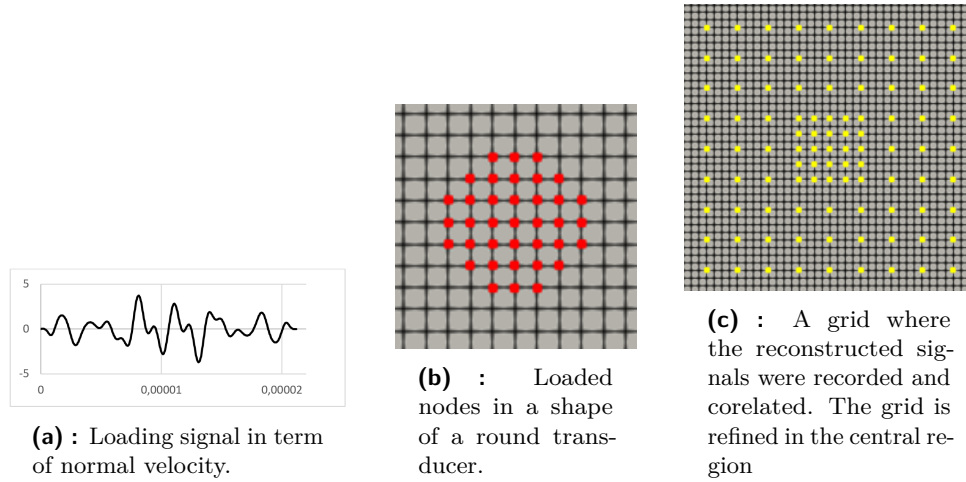


Figure 4.55: Settings of the numerical experiment: loading signal, loaded nodes, and nodes where the output was recorded.

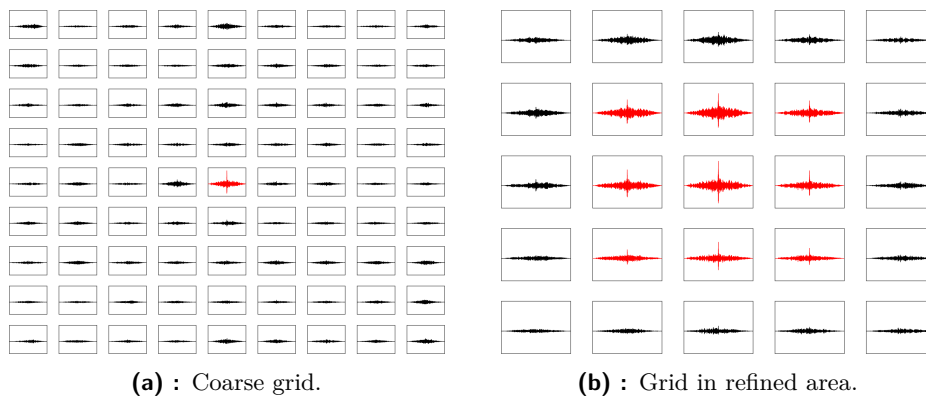


Figure 4.56: Result of correlated signals on coarse and refined grid. The red signals come from nodes originally loaded in the frontal task.

4.5.3 Crack detection

Presented at conferences [A17], [A18], and [A19].

Problem definition

Here, the localization of a forming and a propagating crack was analyzed here. The crack was modeled by disconnected nodes. See the scheme of the problem in Figure 4.57. First, a static analysis of prestressed parts was performed, one part without a crack for the problem of a forming crack, and one part with an existing crack for the problem of a propagating crack. The displacement field was then used as the initial condition for the dynamic simulation of the cracking part. The disconnected nodes, exposed to the same prestress, started to move away from each other behaving as a source of vibrations. The crack was modeled at the center of the left edge, the point \mathcal{A} , and the responding normal velocity was recorded at the point \mathcal{B} in 11 nodes.

The length of the element edge is 0.4 mm, thus the FE mesh consists of 62,500 bilinear four-noded elements. We assume a linear homogeneous isotropic material with Young's modulus $E = 2 \cdot 10^{11}$ Pa, Poisson's ratio $\nu = 0.3$, and mass density $\rho = 7,850 \text{ kg}\cdot\text{m}^{-3}$. Time step size Δt is $4.009 \cdot 10^{-8}$ s.

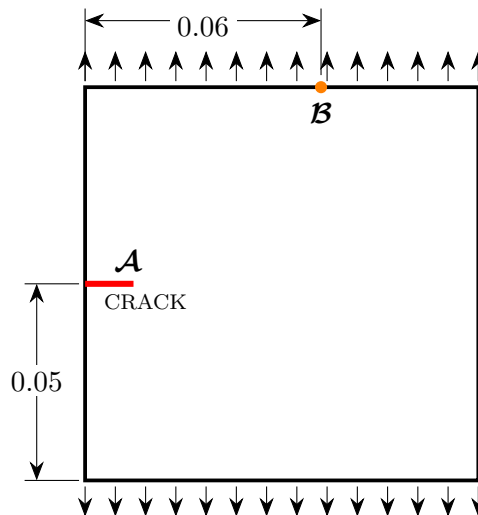


Figure 4.57: Scheme of the numerical experiment of forming and propagating crack detection.

For both problems, in reverse tasks a model without crack was analyzed simulating ignorance of the crack, and 4 tasks were performed with different lengths of computation - $1\,000 \Delta t$, $2\,000 \Delta t$, $10\,000 \Delta t$, and $50\,000 \Delta t$. Considering the longitudinal wave speed $c_L \doteq 5,291.3 \text{ m}\cdot\text{s}^{-1}$, for longest time the wave reflects approximately 100 times between opposite boundaries. Furthermore, reverse tasks of different times were subdivided into 3 sub-tasks, with 1 (denoted 1n in the figures) and 5 (5n) nodes loaded separately with time-reversed signals and 5 (5nAV) nodes loaded with an averaged signal.

Results and discussion

Knowing the time of the "rupture" made it possible to focus on the right time step, at which the field of nodal velocity was visually analyzed. See the results of localization of the forming crack, Figure 4.58, and the propagating crack, Figure 4.59.

The forming crack is noticeable since $2000 \Delta t$ for all numbers of loaded nodes. Evidently, the $1n$ and $5nAV$ cases do not provide enough information for unique refocusing and a "ghost" reconstruction appears, vanishing with the increasing length of computation.

In the problem of propagating crack, the number of loaded nodes plays a more important role than in the previous case. This effect may be compounded by the fact that a different model was used for the computation of the reverse task (model without crack). Basically, a longer computational time is needed to obtain (visually) results of the same quality as for the problem of forming crack.

In all cases, the averaged signal, $5nAV$, makes the refocusing more visible, but more blurred.

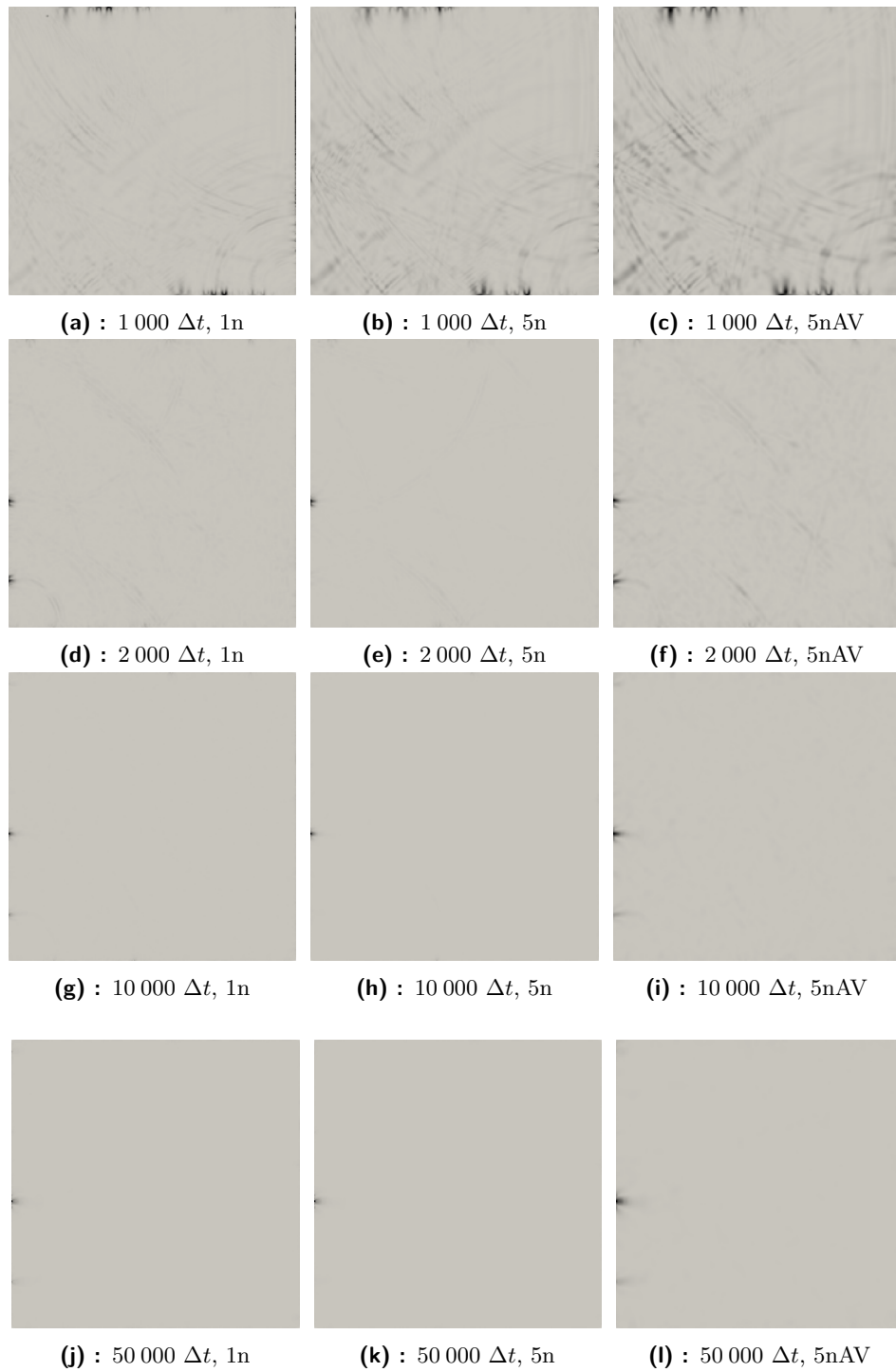


Figure 4.58: Localization of forming crack, magnitude of nodal velocity for different times of computation and number of loaded nodes.

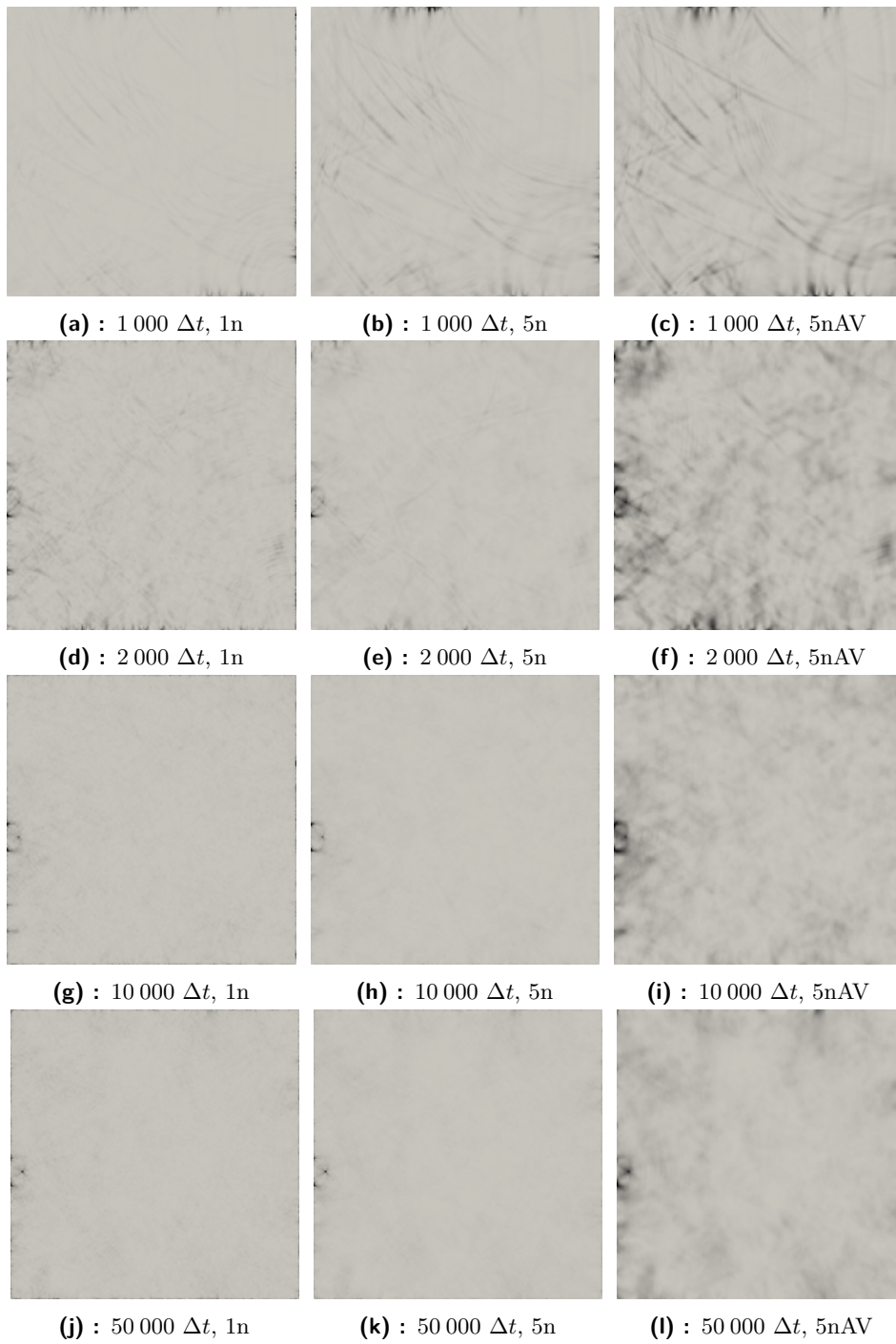


Figure 4.59: Localization of propagating crack, magnitude of nodal velocity for different times of computation and number of loaded nodes.



Chapter 5

Discussion

In this thesis, the use of the computational time reversal method for reconstruction of the original source was investigated. In order to be able to analyze such a problem and have a full control over the analysis, an **explicit solver called *TR-FEM*** was developed. *TR-FEM* combines the desired numerical procedures with non-standard time-varying boundary conditions and automates the TR process.

The numerical solution of direct wave propagation in a homogeneous body was tested and compared with the experiment and the analytical solution, which, among other things, served as a **verification of the code**. Up to a certain time, a good agreement of all methods was achieved. Similarly, the solutions with the analytical approach, the finite element method, and the finite volume method of direct wave propagation in a heterogeneous body were compared.

Afterwards, a detailed analysis of prescribing various time-varying boundary conditions was performed. First, the initial wave field was reconstructed, then a loading pulse was used. Based on this analysis was **developed a procedure** of how to prescribe loading signal to keep the correct time history of all kinematic quantities. For evaluation of quality of the original source reconstruction the proposed cost functions were used.

For verification of the developed methodology, the real experimental data were used in a numerical model for **reconstruction of the real source**. The model was loaded with recorded signals from different positions and the reconstructions were compared. The developed methodology **proved to be successful** and thus allows the original source to be reconstructed in the time domain.

Further, other numerical tests were carried on to show what are the possibilities and limitations of the method. Namely influence of change of temperature on quality of reconstruction, localization of source using cross-correlation of two recorded signals, and localization of emerging and propagating crack modeled by disconnected nodes.

This work adds another piece to the puzzle called the digital twin. The whole concept of the digital twin can only be fully effective if it provides complete information and the nature of the excitation source is as important as its localization.

As the analysis of the influence of temperature implies, the quality of the reconstruction is **highly sensitive** to the input parameters. The success of using this method depends on the precise tuning of the material properties of the tested body. In practice, it would be necessary to first calibrate the model and transfer the material properties from the real to the digital model with sufficient accuracy.

Recommendations for future research

In order to identify the type of flaw such as an emerging crack, an impact, or a loose screw connection, it is necessary to know how such a flaw behaves. In other words, what the derived source signal looks like. As part of further research, it would be useful to create a database of these signals in order to be able to evaluate the types of flaws. Needless to say, the explicit computation is highly time demanding. By definition, the time reversal method works with local sources and such sources are linked with higher frequencies. Future research could investigate applying some model order reduction procedure.



Chapter 6

Conclusions

This research was conducted to improve the quality of the reconstruction of the original source using the computational time reversal method. A procedure for correctly prescribing the loading signal was developed and verified on experimental data, and several numerical tests were performed as a benchmark. **The objectives of the dissertation were met.** It can be concluded that with a sufficient amount of information loaded (temporal and spatial) it is possible to reconstruct the original source in the time domain correctly. Therefore, the use of the computational time reversal method in practice is feasible if the parameters of the computational model are sufficiently calibrated.

Bibliography

Author's peer-reviewed journal papers

- [A1] M. Mračko, V. Adánek, A. Berezovski, J. Kober, and R. Kolman. “Experimental, Analytical, and Numerical Study of Transient Elastic Waves from a Localized Source in an Aluminium Strip”. In: *Applied Acoustics* 178 (July 2021), p. 107983.
- [A2] V. Adánek, A. Berezovski, M. Mračko, and R. Kolman. “A Two-Layer Elastic Strip under Transverse Impact Loading: Analytical Solution, Finite Element, and Finite Volume Simulations”. In: *Mathematics and Computers in Simulation* 189 (Nov. 2021), pp. 126–140.
- [A3] M. Mračko, J. Kober, R. Kolman, Z. Převorovský, A. Tkachuk, and J. Plešek. “Finite Element Method Based Computational Time Reversal in Elastodynamics: Refocusing, Reconstruction and Its Numerical Sensitivity”. In: *Mathematics and Computers in Simulation* 189 (Nov. 2021), pp. 163–190.

Author's conference journal papers

- [A4] D. Gabriel, A. Tkachuk, J. Kopačka, R. Kolman, M. Mračko, M. Bischoff, and J. Plešek. “Estimation of Stability Limit Based on Gersgorin's Theorem for Explicit Contact-Impact Analysis Signorini Problem Using B_penalty Approach”. In: *6th International conference on computational methods in structural dynamics and earthquake engineering - Proceedings* (2017).
- [A5] A. Kruisová, R. Kolman, M. Mračko, and M. Okrouhlík. “Temporal-Spatial Dispersion Analysis of Finite Element Method in Implicit Time Integration”. In: *Engineering mechanics - Book of full texts* (2019).

■ Author's conference talks

- [A6] M. Mračko, A. Tkachuk, R. Kolman, J. Plešek, and D. Gabriel. “Comparison of Local and Global Critical Time Step Size Estimators in Explicit Dynamics”. In: *Computational Mechanics*. Vol. 2016. Špičák.
- [A7] M. Mračko, R. Kolman, A. Tkachuk, J. Kopačka, D. Gabriel, and J. Plešek. “Comparison of Local and Global Critical Time Step Size Estimators in Explicit Dynamics: Multidimensional Case”. In: *ECCOMAS Young Investigators Conference*. Vol. 2017. Milano.
- [A8] M. Mračko, A. Tkachuk, R. Kolman, J. Plešek, and D. Gabriel. “Critical Time Step Estimators in Explicit Dynamics”. In: *Computational Mechanics*. Vol. 2017. Špičák.
- [A9] A. Kruisová, R. Kolman, and M. Mračko. “Full Dispersion Analysis of the Newmark Family in Finite Element Method in Elastodynamics”. In: *Computational Mechanics*. Vol. 2017. Špičák.
- [A10] A. Kruisová, R. Kolman, and M. Mračko. “Dispersion Errors for Wave Propagation in Thin Plate Due to the Finite Element Method”. In: *Computational Mechanics*. Vol. 2019.
- [A11] J. Kober, M. Mračko, and Z. Převorovský. “Verification of Digital Twin Concept for Time Reversal Analysis”. In: *NDT in Progress*. Vol. 2019. Praha.
- [A12] Z. Převorovský, M. Mračko, J. Kober, J. Krofta, and R. Kolman. “Acoustic Source Location by Time Reversal Signal Transfer from Experiment to Numerical Model (Digital Twin)”. In: *Advanced Modelling of Wave Propagation in Solids*. Vol. 2018. Praha.
- [A13] Z. Převorovský, J. Krofta, J. Kober, M. Chlada, and M. Mračko. “Time Reversal Localization of Continuous and Burst Acoustic Emission Sources under Noise”. In: *European Conference on Acoustic Emission Testing*. Vol. 2018. Senlis.
- [A14] Z. Převorovský, J. Krofta, M. Chlada, J. Kober, and M. Mračko. “Testing of Local SHM System Designed for Power Plant Pipeline”. In: *NDT in Progress*. Vol. 2021. Praha.
- [A15] M. Mračko, R. Kolman, J. Kober, Z. Převorovský, and J. Plešek. “Influence of Temperature in Computational Time Reversal Method”. In: *The 2nd International Conference on Advanced Modelling of Wave Propagation in Solids*. Vol. 2018. Praha.
- [A16] M. Mračko, R. Kolman, J. Kober, Z. Převorovský, and J. Plešek. “Computational Time Reversal Method Based on Finite Element Method: Influence of Temperature”. In: *Engineering Mechanics*. Vol. 2018. Svratka.
- [A17] M. Mračko, R. Kolman, J. Kober, Z. Převorovský, and J. Plešek. “Crack Localization Using Computational Time Reversal Method”. In: *ECCOMAS Young Investigators Conference*. Vol. 2019. Krakow.

- [A18] M. Mračko, R. Kolman, J. Kober, Z. Převorovský, and J. Plešek. “The 2nd International Conference on Advanced Modelling of Wave Propagation in Solids”. In: *NDT in Progress*. Vol. 2019. Praha.
- [A19] M. Mračko, R. Kolman, J. Kober, Z. Převorovský, and J. Plešek. “Computational Time Reversal: Localization of Cracks”. In: *Modelling*. Vol. 2019. Olomouc.

■ Author’s conference posters

- [A20] M. Mračko, J. Kopačka, A. Tkachuk, R. Kolman, J. Plešek, and D. Gabriel. “Application of Gershgorin’s Theorem for Time Step Size Estimation for Contact-Impact Problems”. In: *Seminar on Numerical Analysis*. Vol. 2017. Ostrava.

■ Other references

- [21] H. Lasi, P. Fettke, H.-G. Kemper, T. Feld, and M. Hoffmann. “Industry 4.0”. In: *Business & Information Systems Engineering* 64 (Aug. 2014), pp. 239–242.
- [22] H. Cañas, J. Mula, M. Díaz-Madroñero, and F. Campuzano-Bolarín. “Implementing Industry 4.0 Principles”. In: *Computers & Industrial Engineering* 158 (Aug. 2021), p. 107379.
- [23] D. Balageas, C.-P. Fritzen, and A. G??emes. *Structural Health Monitoring*. 2010.
- [24] A. Ghosh, D. J. Edwards, M. R. Hosseini, R. Al-Ameri, J. Abawajy, and W. D. Thwala. “Real-Time Structural Health Monitoring for Concrete Beams: A Cost-Effective ‘Industry 4.0’ Solution Using Piezo Sensors”. In: *International Journal of Building Pathology and Adaptation* 392 (May 11, 2020), pp. 283–311.
- [25] D. Goyal, S. Balamurugan, K. Senthilnathan, I. Annapoorani, and M. Israr, eds. *Cyber-Physical Systems and Industry 4.0: Practical Applications and Security Management*. First edition. Pam Bay, FL: Apple Academic Press, Inc, 2022. 1 p.
- [26] L. F. C. S. Durão, S. Haag, R. Anderl, K. Schützer, and E. Zancul. “Digital Twin Requirements in the Context of Industry 4.0”. In: *Product Lifecycle Management to Support Industry 4.0*. Ed. by P. Chiabert, A. Bouras, F. Noël, and J. Ríos. Vol. 540. IFIP Advances in Information and Communication Technology. Cham: Springer International Publishing, 2018, pp. 204–214.

- [27] F. Pires, A. Cachada, J. Barbosa, A. P. Moreira, and P. Leitaó. “Digital Twin in Industry 4.0: Technologies, Applications and Challenges”. In: *2019 IEEE 17th International Conference on Industrial Informatics (INDIN)*. 2019 IEEE 17th International Conference on Industrial Informatics (INDIN). Helsinki, Finland: IEEE, July 2019, pp. 721–726.
- [28] Y.-C. Choi, J.-H. Park, and K.-S. Choi. “An Impact Source Localization Technique for a Nuclear Power Plant by Using Sensors of Different Types”. In: *ISA Transactions* 501 (Jan. 2011), pp. 111–118.
- [29] H. Yu, L. Lu, and P. Qiao. “Localization and Size Quantification of Surface Crack of Concrete Based on Rayleigh Wave Attenuation Model”. In: *Construction and Building Materials* 280 (Apr. 2021), p. 122437.
- [30] K. Hensberry, N. Kovvali, K. C. Liu, A. Chattopadhyay, and A. Papandreou-Suppappola. “Guided Wave Based Fatigue Crack Detection and Localization in Aluminum Aerospace Structures”. In: *Volume 1: Development and Characterization of Multifunctional Materials; Modeling, Simulation and Control of Adaptive Systems; Structural Health Monitoring*. ASME 2012 Conference on Smart Materials, Adaptive Structures and Intelligent Systems. Stone Mountain, Georgia, USA: American Society of Mechanical Engineers, Sept. 19, 2012, pp. 907–916.
- [31] J. A. Scales and A. Gersztenkorn. “Robust Methods in Inverse Theory”. In: *Inverse Problems* 44 (Oct. 1, 1988), pp. 1071–1091.
- [32] R. S. MacKay and J. D. Meiss, eds. *Hamiltonian Dynamical Systems: A Reprint Selection*. Boca Raton: CRC Press, 2020.
- [33] A. Parvulescu and C. Clay. “Reproducibility of Signal Transmissions in the Ocean”. In: *Radio and Electronic Engineer* 294 (1965), p. 223.
- [34] M. Fink. “Time Reversal of Ultrasonic Fields. I. Basic Principles”. In: *IEEE Transactions on Ultrasonics, Ferroelectrics and Frequency Control* 395 (Sept. 1992), pp. 555–566.
- [35] G. Zhang, J. M. Hovem, H. Dong, and L. Liu. “Coherent Underwater Communication Using Passive Time Reversal over Multipath Channels”. In: *Applied Acoustics* 727 (June 2011), pp. 412–419.
- [36] C. He, Q. Zhang, and J. Huang. “Passive Time Reversal Communication with Cyclic Shift Keying over Underwater Acoustic Channels”. In: *Applied Acoustics* 96 (Sept. 2015), pp. 132–138.
- [37] S. Dos Santos and Z. Prevorovsky. “Imaging of Human Tooth Using Ultrasound Based Chirp-Coded Nonlinear Time Reversal Acoustics”. In: *Ultrasonics* 516 (Aug. 2011), pp. 667–674.
- [38] M. Fink, G. Montaldo, and M. Tanter. “Time-Reversal Acoustics in Biomedical Engineering”. In: *Annual Review of Biomedical Engineering* 51 (Aug. 2003), pp. 465–497.

- [39] M. Fink. “Time Reversal and Phase Conjugation with Acoustic Waves: Industrial and Medical Applications”. In: *Conference on Lasers and Electro-Optics* 3 (2005), pp. 2334–2335.
- [40] C. S. Larmat, R. A. Guyer, and P. A. Johnson. “Time-Reversal Methods in Geophysics”. In: *Physics Today* 638 (Aug. 2010), pp. 31–35.
- [41] W. Sachse, K. Yamaguchi, J. Roget, and A. (Association). *Acoustic Emission: Current Practice and Future Directions*. ASTM STP 1077. ASTM, 1991.
- [42] W. Mu, J. Sun, G. Liu, and S. Wang. “High-Resolution Crack Localization Approach Based on Diffraction Wave”. In: *Sensors (Basel, Switzerland)* 198 (2019).
- [43] G. Ribay, S. Catheline, D. Clorennec, R. Kiri Ing, N. Quieffin, and M. Fink. “Acoustic Impact Localization in Plates: Properties and Stability to Temperature Variation”. In: *IEEE Transactions on Ultrasonics, Ferroelectrics, and Frequency Control* 542 (Feb. 2007), pp. 378–385.
- [44] D. Givoli and E. Turkel. “Time Reversal with Partial Information for Wave Refocusing and Scatterer Identification”. In: *Computer Methods in Applied Mechanics and Engineering* 213–216 (Mar. 2012), pp. 223–242.
- [45] I. Levi, E. Turkel, and D. Givoli. “Time Reversal for Elastic Wave Refocusing and Scatterer Location Recovery”. In: *Journal of Computational Acoustics* 2301 (Mar. 2015), p. 1450013.
- [46] E. Amitt, D. Givoli, and E. Turkel. “Combined Arrival-Time Imaging and Time Reversal for Scatterer Identification”. In: *Computer Methods in Applied Mechanics and Engineering* 313 (Jan. 2017), pp. 279–302.
- [47] C. G. Panagiotopoulos, Y. Petromichelakis, and C. Tsogka. “Time Reversal and Imaging for Structures”. In: *Lecture Notes in Civil Engineering* 2 (2017), pp. 159–182.
- [48] K. Kimoto, K. Nakahata, and T. Saitoh. “An Elastodynamic Computational Time-Reversal Method for Shape Reconstruction of Traction-Free Scatterers”. In: *Wave Motion* 72 (July 2017), pp. 23–40.
- [49] Y. Kwak, S. M. Park, J. Lee, and J. Park. “Rattle Noise Source Localization through the Time Reversal of Dispersive Vibration Signals on a Road Vehicle”. In: *Wave Motion. An International Journal Reporting Research on Wave Phenomena* 93 (2020), p. 102452.
- [50] C. Lopatin, D. Rabinovich, D. Givoli, and E. Turkel. “Computational Time Reversal for NDT Applications Using Experimental Data”. In: *Journal of Nondestructive Evaluation* 363 (Sept. 2017), p. 48.
- [51] H. W. Park, S. B. Kim, and H. Sohn. “Understanding a Time Reversal Process in Lamb Wave Propagation”. In: *Wave Motion* 467 (Nov. 2009), pp. 451–467.

- [52] H. Ammari, E. Bretin, J. Garnier, and A. Wahab. “Time-Reversal Algorithms in Viscoelastic Media”. In: *European Journal of Applied Mathematics* 244 (Aug. 2013), pp. 565–600.
- [53] B. E. Anderson, J. Douma, T. Ulrich, and R. Snieder. “Improving Spatio-Temporal Focusing and Source Reconstruction through Deconvolution”. In: *Wave Motion* 52 (Jan. 2015), pp. 151–159.
- [54] G. Tyras. *Radiation and Propagation of Electromagnetic Waves*. Electrical Science. New York: Academic Press, 1969. 368 pp.
- [55] M. J. Lighthill and G. B. Whitham. “On Kinematic Waves II. A Theory of Traffic Flow on Long Crowded Roads”. In: *Proceedings of the Royal Society of London. Series A. Mathematical and Physical Sciences* 2291178 (May 10, 1955), pp. 317–345.
- [56] G. B. Whitham. *Linear and Nonlinear Waves: Whitham/Linear*. Hoboken, NJ, USA: John Wiley & Sons, Inc., June 16, 1999.
- [57] G. C. Cohen. *Higher-Order Numerical Methods for Transient Wave Equations*. Scientific Computation. Berlin, Heidelberg: Springer Berlin Heidelberg, 2002.
- [58] C. J. Ammon, A. A. Velasco, T. Lay, and T. C. Wallace. *Foundations of Modern Global Seismology*. Second edition. London ; San Diego, CA: Academic Press is an imprint of Elsevier, 2021. 586 pp.
- [59] M. Mitra and S. Gopalakrishnan. “Guided Wave Based Structural Health Monitoring: A Review”. In: *Smart Materials and Structures* 255 (May 1, 2016), p. 053001.
- [60] M. Abbas and M. Shafiee. “Structural Health Monitoring (SHM) and Determination of Surface Defects in Large Metallic Structures Using Ultrasonic Guided Waves”. In: *Sensors* 1811 (Nov. 15, 2018), p. 3958.
- [61] M. Fink. “Time-Reversal Mirrors”. In: *Journal of Physics D: Applied Physics* 26 (1993), pp. 1333–1350.
- [62] D. Givoli. “Time Reversal as a Computational Tool in Acoustics and Elastodynamics”. In: *Journal of Computational Acoustics* 2203 (Sept. 2014), p. 1430001.
- [63] A. Love. *A Treatise on the Mathematical Theory of Elasticity*. University Press, 1934.
- [64] T. J. R. Hughes. *The Finite Element Method: Linear Static and Dynamic Finite Element Analysis*. Dover Publication, 2000.
- [65] T. Belytschko, W. Liu, B. Moran, and K. Elkhodary. *Nonlinear Finite Elements for Continua and Structures*. No Longer Used. Wiley, 2013.
- [66] K.-J. Bathe. *Finite Element Procedures*. Prentice Hall, 1996. PMID: 2558565.
- [67] O. C. Zienkiewicz, R. L. Taylor, and J. Z. Zhu. *The Finite Element Method: Its Basis and Fundamentals*. Butterworth-Heinemann, 2005.

- [68] A. Stroud and D. Secrest. *Gaussian Quadrature Formulas: By A.H. Stroud and Don Secrest*. Prentice-Hall Series in Automatic Computation. Prentice-Hall, 1966.
- [69] T. Belytschko, J. S.-J. Ong, Wing Kam Liu, and J. M. Kennedy. “Hourglass Control in Linear and Nonlinear Problems”. In: *Computer Methods in Applied Mechanics and Engineering* 433 (May 1, 1984), pp. 251–276.
- [70] T. Belytschko and W. E. Bachrach. “Efficient Implementation of Quadrilaterals with High Coarse-Mesh Accuracy”. In: *Computer Methods in Applied Mechanics and Engineering* 543 (Mar. 1986), pp. 279–301.
- [71] D. KOSLOFF et G. A. FRAZIER. “Treatment of hourglass patterns in low order finite element codes”. In : *International Journal for Numerical and Analytical Methods in Geomechanics* 21 (1978), p. 57-72.
- [72] E. Hinton, T. Rock, and O. C. Zienkiewicz. “A Note on Mass Lumping and Related Processes in the Finite Element Method”. In: *Earthquake Engineering & Structural Dynamics* 43 (Jan. 1976), pp. 245–249.
- [73] C. Felippa and K. Park. “The Construction of Free-Free Flexibility Matrices for Multilevel Structural Analysis”. In: *Computer Methods in Applied Mechanics and Engineering* 191 (2002), pp. 2111–2140.
- [74] C. Farhat and F.-X. Roux. “A Method of Finite Element Tearing and Interconnecting and Its Parallel Solution Algorithm”. In: *International Journal for Numerical Methods in Engineering* 326 (1991), pp. 1205–1227.
- [75] G. Arfken. *Mathematical Methods for Physicists*. Boston: Elsevier, 2005.
- [76] R. Kolman, J. Plešek, J. Červ, M. Okrouhlík, and P. Pařík. “Temporal-Spatial Dispersion and Stability Analysis of Finite Element Method in Explicit Elastodynamics”. In: *International Journal for Numerical Methods in Engineering* 1062 (2016), pp. 113–128.
- [77] R. V. Mises und H. Pollaczek-Geiringer. “Praktische Verfahren der Gleichungsauflösung .” In: *ZAMM - Zeitschrift für Angewandte Mathematik und Mechanik* 92 (1929), S. 152–164.
- [78] G. Strang. *Linear Algebra and Its Applications*. Cengage Learning, 2005, p. 544.
- [79] S. A. Gershgorin. “Über Die Abgrenzung Der Eigenwerte Einer Matrix”. In: *Izvestiya Akademii Nauk SSR* 7 (1931), pp. 749–754.
- [80] R. F. Kulak. “Critical Time Step Estimation for Three-Dimensional Explicit Impact Analysis”. In: *Structures Under Shock and Impact*. 1989.

- [81] T. J. Hughes, K. S. Pister, and R. L. Taylor. “Implicit-Explicit Finite Elements in Nonlinear Transient Analysis”. In: *Computer Methods in Applied Mechanics and Engineering* 17–18 (Jan. 1979), pp. 159–182.
- [82] R. Courant, K. Friedrichs, and H. Lewy. “Über Die Partiellen Differenzgleichungen Der Mathematischen Physik”. In: *Mathematische Annalen* 100 (1928), pp. 32–74.
- [83] J. O. Hallquist. *LS-Dyna Theory Manual*. Livermore Software Technology Corporation, 2006.
- [84] B. Zuanetti, T. Wang, and V. Prakash. “A Novel Approach for Plate Impact Experiments to Determine the Dynamic Behavior of Materials Under Extreme Conditions”. In: *Journal of Dynamic Behavior of Materials* 31 (Mar. 2017), pp. 64–75.
- [85] D. Grady. “Shock-Wave Compression of Brittle Solids”. In: *Mechanics of Materials* 293-4 (Aug. 1998), pp. 181–203.
- [86] J. A. Cottrell, T. J. R. Hughes, and Y. Bazilevs. *Isogeometric Analysis: Toward Integration of CAD and FEA*. Chichester, West Sussex, U.K. ; Hoboken, NJ: Wiley, 2009. 335 pp.
- [87] R. Gonzalez. *Digital Image Processing*. Upper Saddle River, N.J: Prentice Hall, 2008.
- [88] R. Kolman, J. Plešek, M. Okrouhlík, and D. Gabriel. “Grid Dispersion Analysis of Plane Square Biquadratic Serendipity Finite Elements in Transient Elastodynamics”. In: *International Journal for Numerical Methods in Engineering* 961 (2013), pp. 1–28.
- [89] Y. Wang. “Frequencies of the Ricker Wavelet”. In: *GEOPHYSICS* 802 (2015), A31–A32.
- [90] J. D. Achenbach. *Wave Propagation in Elastic Solids*, by J. D. Achenbach. North-Holland Pub. Co.; American Elsevier Pub. Co Amsterdam, New York, 1973, xiv, 425 p.
- [91] Z. Prevorsevsky and J. Kober. “Some Factors Affecting Time Reversal Signal Reconstruction”. In: *Physics Procedia* 70 (2015), pp. 604–608.
- [92] A. Ancas and D. Gorbănescu. “Theoretical Models in the Study of Temperature Effect on Steel Mechanical Properties”. In: *Bulletin of the Polytechnic Institute of Jassy LII (LVI)* (Jan. 2006), pp. 49–54.